Risk Assessment Analysis and Urban Heat Mitigation for the city of Prato

Dissertation

submitted to the

Faculty of Architecture, Civil Engineering and Environmental Sciences

Technische Universität Braunschweig

and the

Department of Civil and Environmental Engineering

University of Florence

in candidacy for the degree of a

Doktor der Naturwissenschaften (Dr. rer. nat.) /

Dottore di Ricerca Civil and Environmental Engineering

by

Tommaso Giordano

from Florence, Italy

2026

I. Acknowledgements

I would like to thank all the people close to me during this long-lasting PhD journey. First, I want to acknowledge my supervisors: Dr. Beniamino Gioli, who has been tutoring me for a long-time, mentoring me and introducing me to research as life-inspiring job; Prof. Fabio Castelli, who accepted me as PhD student and helped me out with precious hints during this journey; Prof. Stephan Weber, who warmly welcomed me in Braunschweig as part of his research team and made me feel home during my exchange period.

I want to thank also to my CNR colleagues: Lorenzo, who has been guiding me with practical tips to go ahead and never give-up; Simone and Alice, my room-colleagues sharing ideas and daily issues to be methodically solved; Alessandro, who has always new fresh ideas to work on.; and all the others: Federico, Giovanni, Marianna and Carolina.

Finally, a special thank goes also to my girlfriend, Elena, who had to bear me during these last 3 years - including my abroad period in Braunschweig - and to Jakob, the cool guy who accepted me as flat-mate during my period in Braunschweig.

II. Abstract

The impacts of heat stress and air pollution are both related to severe health risks for citizens. Complexity and heterogeneity of urban systems can lead to some residents being more exposed than others, possibly exacerbating social inequalities. Whilst the impacts of heath stress and air pollution on population health are known, their relationship with socioeconomic vulnerability has been less investigated. In this work, an integrated risk assessment framework for a mid-size city (Prato, Italy) was developed by combining information on concurrent hazards (summer heat stress and winter air pollution), socioeconomic vulnerabilities indices (Income deciles and Deprivation Index), and demographic exposure (elderly population fraction). Multiple data sources were merged through a novel approach incorporating observed measurements of air temperature and air pollution (PM10 and PM2.5 concentrations) at fine time and spatial resolution through a dense IoT sensor network. Results indicated that i) socioeconomic vulnerability was significantly and positively correlated with summer heat intensity (R > 0.8); ii) lowest and highest income classes experienced lower PM concentrations compared to middle-income classes; iii) the fraction of elderly people associated with low socioeconomic vulnerability was little impacted by heat intensity but mostly exposed to winter air pollution depending on their proximity to highly travelled roadways and industrial activities.

Although the extensive coverage of the low-cost sensor network, some zones of the city remained unmonitored. To overcome these observational gaps and achieve full spatial coverage, a statistical modelling approach was employed to map air temperature across the urban domain. Specifically, air temperature during a warm summer day was modelled by integrating IoT observations with three remote-sensing predictors: Land Surface Temperature (LST), Sky View Factor (SVF), and Vegetation Fraction Cover (VFC). A multiple linear regression framework yielded moderate accuracy (R2 = 0.30, RMSE = 0.51 °C), and the mapped temperature showed strong spatial agreement with the Urban Heatwave Thermal Index employed in the risk assessment analysis (I-Moran = 0.43).

Addressing the combined effects of multiple hazards within a robust risk assessment framework and explore approaches to spatialize hazards distribution is essential to identify risk. However, this must be complemented by effective mitigation strategies. In this regard, irrigation of urban parks emerges as a promising heat-mitigation measure, enhancing evaporative cooling and lowering near-surface air temperatures. In the final part of this thesis, the potential cooling effect of irrigating urban parks was assessed using the ENVI-met microclimate model. Four irrigation scenarios were simulated for eight selected parks classified according to tree-cover density and compared against a baseline non-irrigated condition. During the warmest hours of the day (12:00–16:00), the average AirT decreased from low (CL1) to high (CL4) tree density classes by approximately 1.5 °C and 0.5 °C in cooler and warmer microclimatic classes. Similarly, increasing irrigation intensity from the baseline to the most intensive irrigation scenario further reduced temperatures by about 1.5 °C in both microclimatic classes. The combined effect of higher tree density and irrigation led to a clear shift toward cooler thermal classes, with mean temperatures moving from >35.0 °C to <34.0 °C.

III. List of Figures

Figure 13. Satellite images and corresponding three-dimensional representations developed with the ENVI-met model for the irrigated (A) and rainfed (B) urban green areas used for modelling validation and tuning.

Figure 14. Satellite images extracted from Google Earth and corresponding three-dimensional representations developed with the ENVI-met model for the eight urban green areas, grouped into Near-River (NR, top) and Inner-City (IC, bottom) microclimate classes across increasing tree-density classes (01–04).

Figure 15. Income deciles (a) and Deprivation Index (b) averaged at census tract level for the whole municipality of Prato.

Figure 16. Average UHTI (a) and Fraction of Elderly People (b) at census tract level.

Figure 17. Winter (01/12/2022-28/02/2023) average PM10 (a) and PM2.5 (b) concentrations at each monitoring site.

Figure 18. Average summer-season (01/06/2022-31/08/2022) air temperature (°C) computed at each monitoring site.

Figure 19. Relation between hazards (UHTI, AirT, PM concentrations) and vulnerability (DI, I) variables averaged for income deciles grouped in classes of similar size. Red lines and curves were estimated through simple and second-degree polynomial regression models. Error bars represent standard error.

Figure 20. Scatterplots of the principal components data (PC1 and PC2). Red arrows represent the loadings vectors (see Table 4) of each variable. For figure readability red arrows were multiplied by a constant factor (k=5).

Figure 21. Gap-filling RMSE for each ID station site.

Figure 22. Average AirT between 12:00 and 16:00 observed the 16th July 2024.

Figure 23. Scatterplots of SVF (a), VFC (b) and LST (c) versus AirT.

Figure 24. Scatterplot between observed and multiple linear regression modelled air temperature values.

Figure 25. Spatial distribution of modelled air temperature across Prato.

Figure 26. Bivariate Moran’s plot of UHTI and modelled AirT.

Figure 27. Bivariate LISA map of modelled AirT and UHTI.

Figure 28. Validation of the ENVI-met model for irrigated and rainfed sites against observations (grey filled dots). Simulated values obtained with default soil properties are shown as a black dotted line; error bars represent the corresponding standard deviation. Simulated SWC dynamics are also reported for default (black dotted line) and calibrated/tuned (red line) soil properties against observations (grey filled dots).

Figure 29. Average diurnal differences in AirT (a), RH (b), and SWC (c) between the baseline and the four irrigation scenarios (AS1–AS4), simulated across four tree-density classes (CL1–CL4) for the urban park domains located in the inner-city (IC) and near-river (NR) classes. Shaded areas indicate confidence intervals arising from the spatial aggregation of the simulated domain and reflect sub-grid spatial variability.

Figure 30. Heatmaps of average air temperature (°C) and corresponding temperature classes (0.5 °C bins) simulated for near-river (NR, left) and inner-city (IC, right) urban park microclimate classes under baseline (BS) and four irrigation scenarios (AS1–AS4), across four tree-density classes (CL1–CL4). Values represent mean conditions during the time-window (12:00–16:00), averaged across the eight urban park domains. Cooler colors indicate lower air temperatures. Row and column averages summarize the combined effects of tree-density and irrigation intensity on thermal conditions.

Figure 31. Incremental contribution of tree-density to air-temperature mitigation in near-river (NR) and inner-city (IC) microclimatic class. Upper panel (a) shows the incremental air-temperature reduction (ΔAirT, °C) associated with increasing tree-density classes (CL2–CL4) for NR (blue bars) and IC (orange bars); error bars indicate variability across aggregated domains. Lower panels illustrate the relative contribution (%) of each tree-density class to the total cooling effect within NR (b) and IC (c) microclimate classes.

Figure 32. Incremental contribution of irrigation intensity to air-temperature mitigation in near-river (NR) and inner-city (IC) microclimatic classes. Upper panel (a) shows the incremental air-temperature reduction (ΔAirT, °C) associated with increasing irrigation intensity (AS1–AS4) for NR (blue bars) and IC (orange bars); error bars indicate variability across aggregated domains. Lower panels illustrate the relative contribution (%) of each irrigation scenario to the total cooling effect within NR (b) and IC (c) microclimate classes

Figure 33. Joint economic–thermal response of irrigation strategies aggregated at climate classes. The figure shows the relationship between total daily irrigation costs (€, red line, left y-axis), air temperature reduction (ΔAirT, °C; blue line, right y-axis), and normalized cooling efficiency (°C $€^{-1}$,

scaled 0–1; grey bars) for combined inner-city and near-river microclimate classes scenarios (IC–NR), with values averaged across tree-density classes

IV. List of Tables

V. List of Acronyms

AirT	Air temperature
ARPA	Agenzia Regionale per la Protezione Ambientale
AUHI	Atmospheric Urban Heat Island
CFD	Computational Fluid Dynamics
DI	Deprivation Index
EEA	European Environmental Agency
FEP	Fraction of Elderly People
G	Ground Heat Flux
H	Sensible Heat Flux
I	Income Decile
IPCC	International Panel on Climate Change
KMO	Kaiser–Meyer–Olkin
LC	Low-Cost
LE	Latent Heat Flux
LISA	Local Indicator of Spatial Association
LST	Land Surface Temperature
MAE	Mean Absolute Error
NDVI	Normalized Difference Vegetation Index
OLS	Ordinary Least Squares
PAESC	Piano d'Azione per l'Energia Sostenibile e il Clima
PCA	Principal Components Analysis
PM	Particulate Matter
R	Pearson Correlation Coefficient
RH	Relative Humidity

RMSE	Root Mean Squared Error
RMSE-CV	Root Mean Squared Error – Cross Validated
R2	Determination Coefficient
SE	Standard Error
SIR	Servizio Idrologico Regionale
SVF	Sky View Factor
SUHI	Surface Urban Heat Island
TAW	Total Available Water
TDR	Time Domain Reflectometry
TIRS	Thermal Infra-Red Sensor
UHTI	Urban Heatwave Thermal Index
UHI	Urban Heat Island
VFC	Vegetation Fraction Cover
WHO	World Health Organization
WRF	Weather Research and Forecasting
λ	Eigenvalues
θ	Soil Water Content

Table of Contents

1. Introduction

1.1 Background

Urban areas are particularly exposed to adverse environmental conditions due to the interaction between biophysical properties and anthropogenic activities, resulting in elevated air temperatures and poor air quality. Heat stress, which is generally higher during summer heatwaves, causes health threats such as hyperthermia, heat strokes and other cardiovascular and respiratory diseases (WHO, 2004). Because of climate change, heatwaves and heat stress are increasing both in intensity and duration (Perkins, 2015; Copernicus, 2023), especially in Europe (Fig. 1). During the 2012–2021-decade, European countries experienced heatwaves with magnitude 50% higher than during the 2002-2011 decade (Alizadeh et al., 2022).

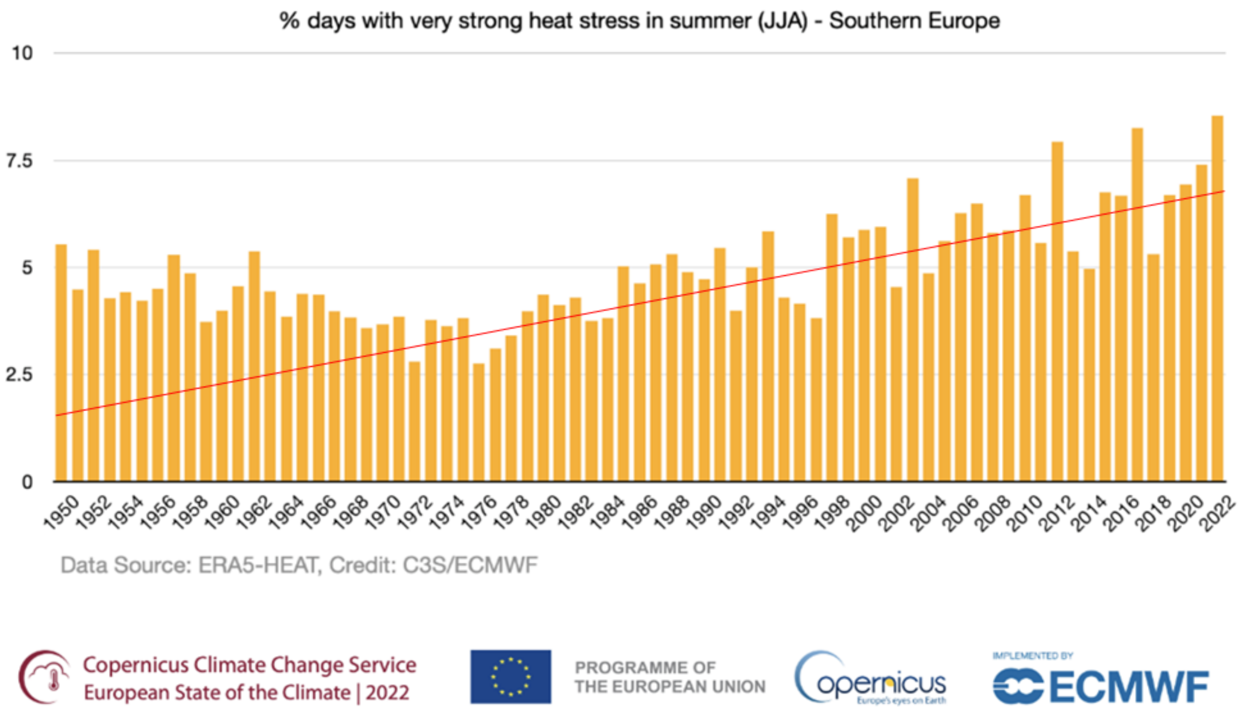

Figure 1. Percentage of days during summer with 'very strong heat stress' (UTCI between 38 and 46°C) in southern Europe, from 1950 to 2022 (Copernicus, 2023)

On the other hand, poor air quality also impacts public health, generating inflammation, oxidative stress and immunosuppression that directly impact our body's organs, thus facilitating strokes, heart and pulmonary diseases and cancer (WHO, 2024). Despite average air pollution is improving in Europe (Sicard et al., 2023; EEA, 2023a) and European citizens are being less exposed (Fig. 2), its spatial distribution is heterogeneous and health impacts still represent a significant burden for residents of many urban areas (EEA, 2023b). With respect to WHO guidelines (WHO, 2021), in 2023 62.0% of European urban residents were exposed to PM10 concentrations above 15 µg m^{-3} (annual air quality guideline level), 94.4% to PM2.5 concentrations above 5 µg m^{-3} (annual air quality guideline level) 84.1% to NO2 concentrations above 10 µg m^{-3} (annual air quality guideline level)and 95.3% to O3 concentrations above 100 µg m^{-3} (short-term air quality guideline level) (EEA, 2025).

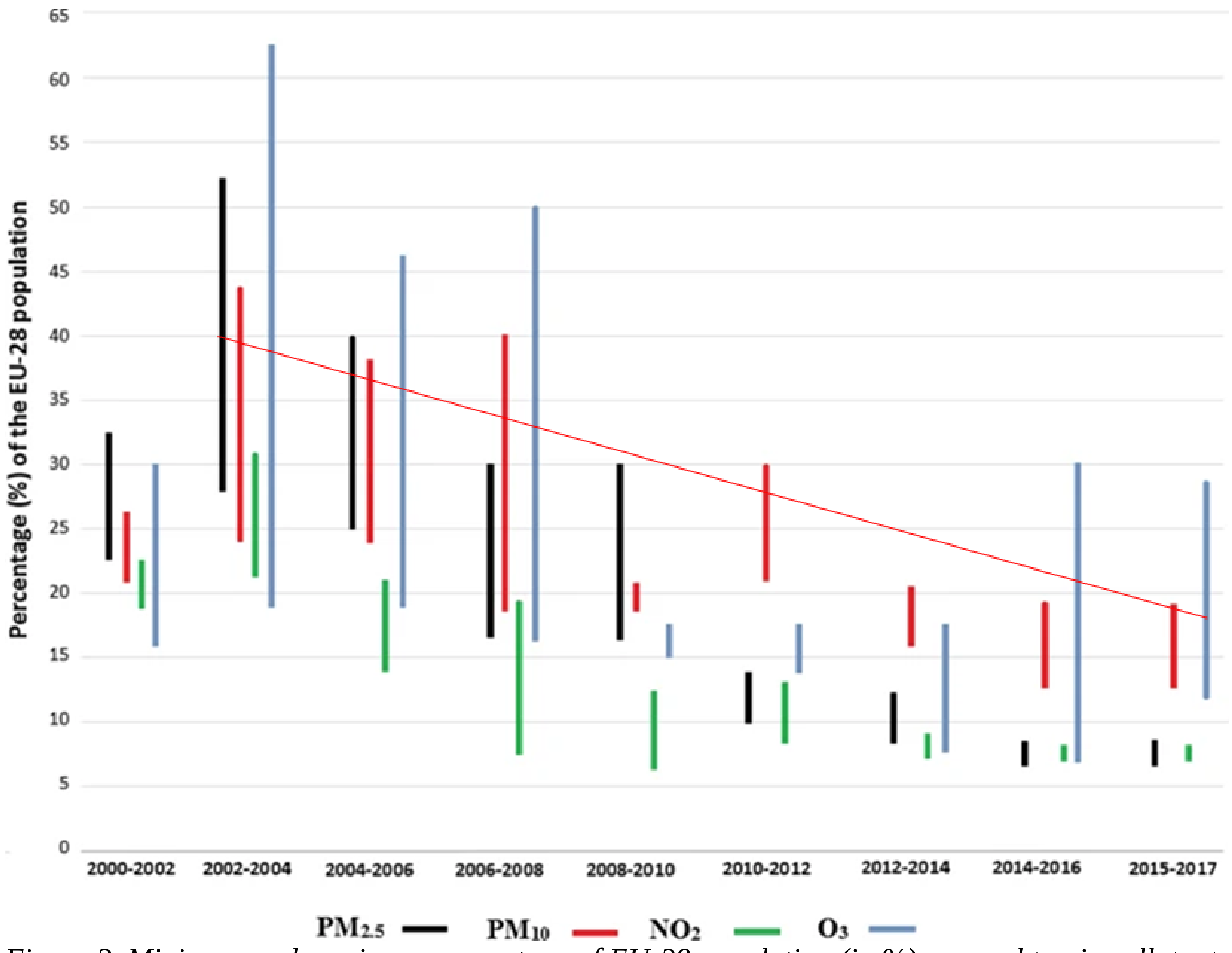

Figure 2. Minimum and maximum percentage of EU-28 population (in %) exposed to air pollutants concentrations (particulate matter PM2.5 and PM10, nitrogen dioxides NO2 and tropospheric ozone O3) exceeding the European Union limit or target values between 2000 and 2017 (Adapted from Sicard et al., 2021)

Among European countries, Italy generally experiences extreme summer weather conditions characterized by drought and heatwaves (Spano D. 2021; Rousi et al., 2022). Moreover, persistent wintertime air pollution issues especially in the northern area of the Po Valley (Fig. A1) usually lead to adverse public health consequences (Gualtieri et al., 2022; Stafoggia et al., 2017).

Cities are complex and heterogeneous systems, characterized by different biophysical features such as trees and green spaces, urban canyons dimensions, anthropogenic materials, and anthropogenic activities such as road traffic volumes and commercial endeavors. All of these features influence and interact with the atmosphere generating local microclimates, thus determining the so-called Urban Heat Island (UHI) and air pollution patterns (Barlow, 2014; Huang et al., 2022; Li et al., 2020). Both UHI and air pollution are strongly linked to each other. On the one hand, the use of air conditioning during hot periods intensifies the UHI effect, which in turn accelerates the formation of tropospheric ozone and Volatile Organic Compounds (Ulpiani, 2021). Similarly, urban aerosol pollution can contribute to UHI enhancement by altering radiative forcing (Cao et al., 2016). On the other hand, this link can show an opposite pattern, since UHI can strengthen turbulent dispersion, thus favoring pollutant dispersion (Fallmann et al., 2016). Adverse hot spots in terms of urban heat and poor air quality can be associated with a limited number and size of green spaces and infrastructures, which result in a decreased cooling effect, irradiance attenuation (e.g., shading) and pollutant absorption (Coombes and Viles, 2021).

When the distribution of green spaces and pollutant emission sources is intersected with granular socioeconomical variables, social injustice patterns may arise. Areas with high population density, low-income residents and vulnerable populations (such as underserved communities, people with health complications, elderly) have been found not to have access to green spaces, limiting their ability to mitigate outdoor heat stress (Wolch et al., 2014, Rocha et al., 2024). On the other hand, urbanized areas close to pollutant emission sources – such as highly travelled roadways, industries, and dense commercial areas – can be more exposed to adverse air quality despite the presence of green infrastructures (Jennings et al., 2021). Also, local wind regimes can transfer pollutants to urban areas not directly adjacent to upwind emission sources (Kanabkaew et al., 2019). In this work, vulnerability was accounted as component of risk assessment according to IPCC, (2022), in which it was defined as a relation between sensitivity (degree to which a system is affected by natural and anthropogenic disasters) and adaptive capacity (ability of a population to cope with disasters). Whilst climate and air pollution impact on population health were widely reported in literature (D'Amato et al., 2015; De Marco et al., 2019; Sicard et al., 2021; Dambha-Miller et al., 2022), socioeconomic vulnerability as a further key risk factor and environmental justice driver has been less investigated. Ellena et al. (2023) performed a heat stress risk assessment for the city of Turin (Italy) integrating socioeconomic, health and environmental conditions of the elderly population and found that heat risk is higher in areas with social and economic disadvantages. Venter et al. (2023) assessed the spatial exposure inequality to heat and air pollution in Oslo (Norway), finding that poorer residents were more exposed. Badaloni et al. (2023) assessed the relationship between socioeconomic deprivation and environmental vulnerabilities in Rome (Italy), indicating instead that areas with the highest pollution and temperature values did not correspond to high socioeconomic deprivation.

Assessment of the intraurban combined distribution of heat and adverse air quality remain limited in most European cities, due to the lack of adequate monitoring tools capable of resolving the inter-relations between environmental and socioeconomic aspects. Numerical models are frequently used to reproduce physical processes occurring at different spatial scales in urban areas, requiring high computational capacity and accurate knowledge of boundary conditions and other input parameters (Trane et al., 2024). Remote sensing is commonly used to derive Land Surface Temperature (LST), typically used as a proxy for air temperature to map the UHI distribution and assess heat stress. However, remote sensing LST is actually a measure of surface temperature, which well defines the Surface Urban Heat Island (SUHI) but not the Atmospheric Urban Heat Island (AUHI), measured through air temperature and more directly linked to heat stress. The difference between SUHI and AUHI particularly stands during daytime, when remote sensing is unable to capture the dependence of air temperature on the three-dimensional elements of the urban canopy (Hu et al., 2013), despite its capacity to investigate large areas with fine spatial resolution. Therefore, SUHI may not accurately proxy heat stress, which depends on several factors such as relative humidity, local wind regimes and radiation, not even captured by AUHI. As a result, to obtain biometeorological information effectively related to heat stress, it is preferable to adopt approaches that integrate LST with building height, sky view factor and other morphological variables (Fiorillo et al., 2023). Ground-based monitoring of air temperature and air pollution is therefore necessary. It can be performed by deploying dense sensor networks that seamlessly integrate and improve the information provided by the sparse official air quality and meteorological stations (Kumar et al., 2015; Brilli et al., 2021; M. A. Zaidan et al., 2022).

The employment of a robust risk assessment framework is essential to highlight patterns of vulnerable population exposed to environmental hazards. However, this represents only an initial step within a broader risk management framework, which includes the evaluation of mitigation strategies aimed at reducing population health risks. A wide range of approaches has been explored to tackle urban heat, including nature-based solutions and green infrastructures (e.g., urban parks and forests), cooling materials (e.g., reflective pavements and cool roofs), and blue infrastructures (e.g., rivers, lakes, and wetlands) (Aleksandrowic et al., 2017). Among these, urban green spaces provide temperature cooling through evapotranspiration from vegetation and soil and by reducing the absorption of solar radiation through shading (Hami et al., 2019; Saher et al., 2019). However, the cooling effectiveness of urban green spaces depends on several factors such as their size, shape, and the surrounding and internal built-up areas (Cheung et al., 2022). Irrigation also plays a potential key role, since it provides a stronger evapotranspiration cooling effect. The additional soil moisture from irrigation increases latent heat flux and decreases sensible heat flux from a turfed surface, thus leading to cooler surface and near-surface temperature (Lunel et al., 2024; Jiang et al., 2014; Kueppers et Snyder, 2012; Cook et al., 2011; Spronken-Smith et al 2000). Nevertheless, the effectiveness of this process is strongly influenced by water availability, irrigation scheduling and background climatic conditions. When water availability and irrigation scheduling are not a limiting factor, background air temperature, vapor pressure deficit, wind speed, and solar radiation are the main factors influencing evapotranspiration (Allen et al., 2000). High air temperature and strong solar radiation increase the available energy for evaporation, whilst elevated vapor pressure deficit and wind speed facilitate the diffusion of water vapor away from the surface (Burt et al., 2005). Consequently, the cooling potential of irrigation tends to be greater in hot arid climates, where atmospheric evaporative demand is high, than in temperate, humid, or continental regions (Cheung et al., 2022).

The analysis of irrigation effects on local climate originates from agricultural studies, which in recent years have become increasingly thorough and comprehensive, covering different regions of the world and a wide range of spatial scales (de Vries, 1959; Fowler et al., 1974; Bonfils et Lobell, 2007; Yoshida et al., 2012; Nocco et al., 2019; Yang et al., 2020). Following this line of research, interest toward urban contexts increased, with early investigations examining the microclimatic conditions of irrigated urban parks (Spronken-Smith & Oke, 1998; Potchter et al., 2006). More recently, studies have employed numerical and empirical models as well as direct measurements. Using the SURFEX model for Adelaide, Australia, Broadbent et al. (2018) found that diurnal summer air temperatures decreased by up to 2.3 °C. Gao et al. (2020), applying the WRF model in Sydney, reported reductions of 1.5 °C in maximum daily temperature. In Paris, Daniel et al. (2018) applied a Town Energy Balance model and demonstrated that vegetation watering significantly lowered air temperatures in densely vegetated residential areas (up -3.8°C). On a broader scale, Cheung et al. (2021) developed a linear regression model where the difference in mean near-surface air temperature between irrigated and non-irrigated conditions, derived from a meta-analysis of 19 case studies, was used as the dependent variable, while background climatic variables, including mean near-surface air temperature, rainfall, specific humidity, wind speed, and net radiation, were initially considered as independent predictors. They applied the model to 100 cities worldwide, showing average cooling of −1.09 °C (up to −1.65 °C in arid climates), although a minority of cities experienced slight warming (+0.76 °C). Wang et al. (2019) showed the cooling effect efficiency triggered by irrigation of urban vegetation across US contiguous urbanized areas through WRF simulations, reporting an average near-surface air temperature reduction of 1 °C for every 7.27 mm of daily irrigation applied. At field scale, empirical evidence reinforces these findings, with Cheung et al. (2024) detecting cooling of up to −0.9 °C between irrigated and non-irrigated turfgrass in Melbourne, and Lam et al. (2020) observing temperature decreases of up to −4 °C during heatwaves in the city's botanical gardens.

Despite existing evidence, assessing the potential cooling effects of irrigation in urban green areas remains challenging due to the high costs of experimental campaigns, the limited number of suitable (i.e., accession and security) experimental sites, and challenges associated with continuous data acquisition (i.e., energy supply availability). To overcome these limitations appropriate tools capable of disentangling the complex physical interactions between soil, vegetation, and the atmosphere and isolating the irrigation effect are required. Numerical models provide such a means by solving the governing equations of physical processes, offering spatially explicit outputs across the computational domain, and enabling comparative analyses under different scenarios (Trane et al., 2024). Among various numerical models, ENVI-met is a widely used three-dimensional microclimate model mainly applied to study the thermal comfort benefits of cooling strategies, including irrigation and water-based mitigation techniques (Tsoka et al. 2018; Scharfstädt et al., 2024; Gobatti et al., 2024).

1.2 Objectives

Within this context, the integration of multiple data sources at fine spatiotemporal resolution has emerged as a key requirement for the study of urban environmental hazards; however, such integration is often constrained by the limited availability of large-scale monitoring infrastructures at the city scale. These data are indeed crucial for identifying hotspots of hazards across a city, characterizing population and urban vegetation patterns, and for the local initialization and validation of modelling frameworks. For this reason, this thesis aims to fill this gap by combining high spatial- and temporal-resolution ground-based measurements, detailed urban information layers, and high-resolution numerical modelling using the city of Prato (Italy) as a case study because of the availability of extensive high-resolution data and a well-established local framework of monitoring, research, and planning activities addressing urban sustainability and climate change mitigation. Specifically, how can a risk assessment framework be developed to study the population exposure to urban summer heat and low winter air quality conditions? How accurate can the hazard modelling be relying on measurements from a dense network of low-cost sensors? How do high-resolution ground-based microclimatic observations improve the assessment and simulation of irrigation-induced thermal mitigation in urban parks with differing tree-cover densities and urban contexts?

1.3 Thesis structure

Following this objectives scheme, the thesis proceeds as follows: chapter 2 shows the materials and methods employed to i) develop a risk assessment framework, ii) assess the modelling of summer heat city-wide and iii) simulate irrigation driven cooling effect. Chapter 3 illustrates the results corresponding to each point. Chapter 4 shows the discussion of the obtained results, while Chapter 5 shows the conclusions of the thesis (Fig. 3).

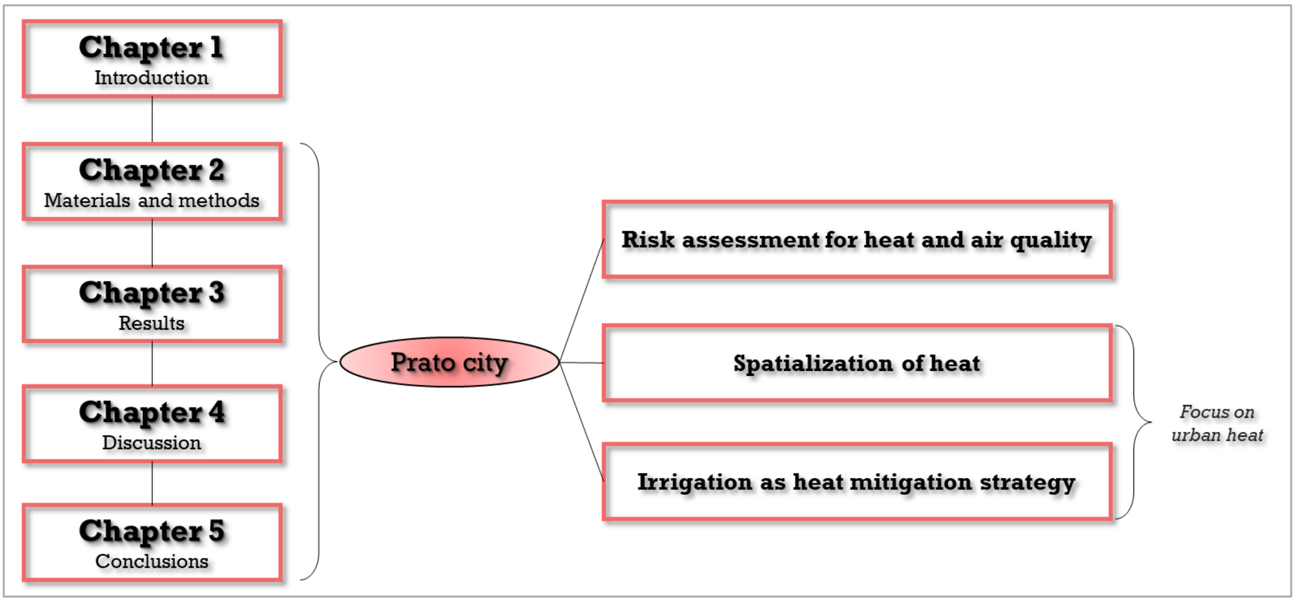

Figure 3. Thesis structure

2. Materials and methods

2.1 Study Area

The municipality of Prato (Italy, 43°52′48″ N, 11°05′54″ E, Fig. 4) covers about 97 km^2, with a population of almost 200,000 inhabitants (ISTAT, 2022). Prato has a mesothermal temperate climate, classified as Csa in the Köppen and Geiger climate classification (Kottek et al., 2006), characterized by dry and hot summers and cool damp winters. Extreme weather-related hazards often take place during summer (heatwaves) and fall-winter (air pollution critical episodes due to capping inversion in the near surface vertical thermal profile). The city is historically known to be a European hub for textile, with its land-use showing a pattern of industrial districts mixed with residential neighborhoods. The municipality of Prato was selected by the European Commission among the 100 European cities that will contribute to the mission "100 smart and climate-neutral cities by 2030". Also, the city has been participating to innovation paths to approach climate neutrality by 2030 through the involvement in several scientific projects such as "Prato Urban Jungle" (https://www.pratourbanjungle.it/it) and "Prato Forest city" (https://www.pratoforestcity.it/). Prato also hosts an industrial aqueduct managed by G.I.D.A. spa (Gestione Impianti di Depurazione Acque) alongside the civil one. Currently, the wastewater treatment facility recovers approximately 10 million cubic meters of water annually, of which only 3.5 million cubic meters are reused. The remaining water presents an opportunity to implement innovative, circular strategies for sustainable and efficient management of greening in urban areas to increase city resilience.

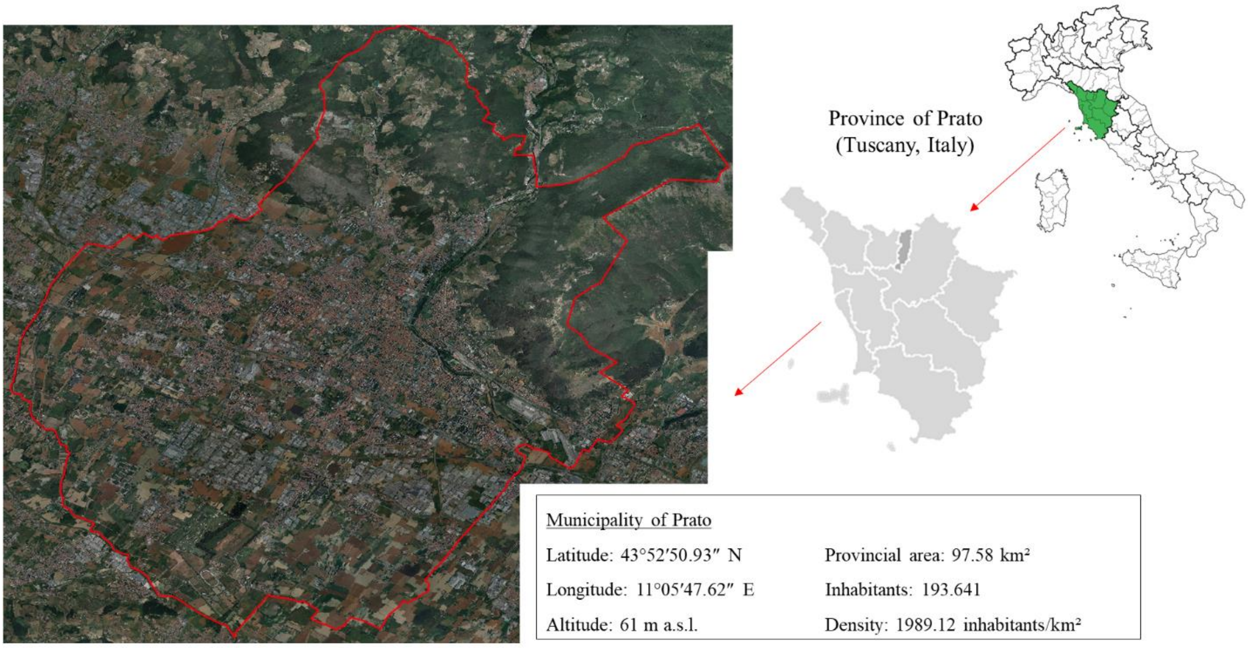

Figure 4. Geographical location of the study area

2.2 Assessment of risk components

2.2.1 Risk assessment framework

Risk assessment has been approached through different perspectives across disciplines, ranging from probabilistic methods in disaster risk reduction to exposure–response models in public health. In environmental sciences, risk has often been quantified through indices that combine hazard intensity with vulnerability indicators, while in urban studies it is increasingly linked to spatial analyses of exposure to climatic extremes. These diverse approaches share the goal of identifying populations, assets, or systems at risk, but they differ in the way they conceptualize and integrate the contributing factors (O'Lenick et al., 2019). The Intergovernmental Panel on Climate Change (IPCC) has provided a widely adopted framework that conceptualizes risk estimation as the interaction between hazards, exposure, and vulnerability (IPCC, 2022). Hazard refers to the potentially damaging physical event or stressor, such as extreme heat or high concentrations of air pollutants, that can cause harm. Exposure describes the presence of people, assets, or systems in places that could be adversely affected by the hazard. Vulnerability represents the propensity or predisposition of a population to be negatively affected, determined by factors such as age, health status, and socioeconomic conditions. Following these definitions, the risk assessment framework adopted for this work followed the scheme reported in the following table (Table 1).

Risk assessment component	Category	Variable	Acronym	Spatial representation	Data source
Hazard	Summer heat	Urban Heatwave Thermal Index	UHTI	10-m grid	CNR-IBE
	Summer heat	Air temperature	AirT	Point	CNR-IBE
	Winter air pollution	Particulate matter concentrations	PM_{10} and $PM_{2.5}$	Point	CNR-IBE
Exposure	Demographic	Fraction of Elderly People	FEP	Census tract	Municipality of Prato

Risk assessment component	Category	Variable	Acronym	Spatial representation	Data source
Vulnerability	Socioeconomic	Deprivation Index	DI	Census tract	Municipality of Prato
		Income	I	Census tract	Municipality of Prato

Table 1. Risk assessment framework, including three components (hazard, exposure and vulnerability), five categories, seven variables (UHTI, air temperature, PM2.5, PM10, fraction of elderly people, deprivation index and income.

These risk assessment components were disaggregated in categories and variables, which will be better described in the next paragraphs. Hazards include two categories: summer heat, represented by air temperature and UHTI, and winter air pollution, represented by $PM_{2.5}$ and PM_{10} concentrations. Following Ellena et al. (2023), exposure includes the demographic category, represented by the fraction of elderly people living in the area. This exposure variable was chosen since elderly people are considered as one of the demographic categories mostly impacted by these hazards (Meade et al., 2020; Simoni et al., 2015). Finally, vulnerability includes the socioeconomic condition, represented by the income deciles and the deprivation index.

2.2.2 Ground-based measurements

Ground-based measurements of air pollution (PM2.5 and PM10 concentrations) and air temperature were collected within the whole city through a network of low-cost (LC) air quality stations named AirQino, installed at ∼3.5 m height (Fig. A2). Initially consisting of 30 stations, this LC network eventually consisted of 20 stations (see later in § 2.6, Fig. 6 and Table A4). Each LC station was equipped with sensors collecting PM2.5 and PM10 concentrations (Novasense SDS011) and air temperature (AM2315) at high temporal frequency (2–3 min.). Accuracy of these sensors is 10 % (PM2.5 and PM10) and 5 % (air temperature), while resolution is 1.00 μg m−3 (PM2.5 and PM10) and 0.30 °C (air temperature). Further details can be found in Table A1. Reliability of these sensors was tested over different environments and climate conditions, such as in Italy (Cavaliere et al., 2018; Brilli et al., 2021), the Arctic region (Carotenuto et al., 2020), and the Sub-Saharan Africa (Gualtieri et al., 2024).

Air pollution and air temperature data were extracted for the period 01/06/2022–28/02/2023, which includes both the winter and summer seasons. Elevated PM concentrations typically occurring in wintertime were included, as well as extreme summertime temperatures, which covered summer 2022 characterized by prolonged heatwaves (Copernicus, 2023). Air quality and air temperature data were quality-controlled with specific despiking and outliers' detection procedures (Brilli et al., 2021), and then aggregated and averaged at both hourly and daily time-step. Additional data from regional agencies monitoring stations were collected to assess the reliability of air quality and air temperature measurements collected from sensor network. These included daily data of $PM_{2.5}$ and PM_{10} concentrations from two official stations of the European Environmental Agency (EEA) managed by the Tuscany Regional Environmental Protection Agency (ARPAT), i.e., ID 21 and 22, and air temperature data (15-min resolution) from an official meteorological station of the Regional Hydrological Service of Tuscany (SIR), i.e., ID 23 (Fig. 6 and Table A4). Daily time series of PM concentrations and air temperature collected by all AirQino stations as compared to ARPA and SIR reference stations are plotted in Figure A3. Auxiliary wind speed and direction data from the SIR meteorological station (ID 23) have been retrieved to picture the wind regime of the study area and thus support results discussion.

2.2.3 Urban Heatwave Thermal Index

The spatial pattern of heat intensity was assessed through the Urban Heatwave Thermal Index (UHTI), developed for the City of Prato within the "Piano d'Azione per l'Energia Sostenibile e il Clima" project (PAESC, accessed on 13th February 2023). Developed by Nardino et al. (2022), the UHTI is a normalized index designed to quantify intra-urban air temperature variability during heatwave conditions, enabling the identification of thermal hot-spots across the urban fabric. The construction of this index depends on the combination of three variables: i) Vegetation Fraction Cover (VFC); ii) Land Surface Temperature (LST); iii) Sky View Factor (SVF). VFC, a widely used indicator to monitor vegetation status, was computed from 2015-2021 summer months (June, July, August) NDVIs obtained from Sentinel 2A images (10m resolution) with cloud cover lower than 10%. The NDVI is a dimensionless index describing the difference between the visible (RED) and near infrared (NIR) reflectance of vegetation cover and has been widely used to study the effects of vegetation on the urban microclimate (Guha et al., 2018; Guerri et al. 2021). In this study, the average summer NDVI was computed and the corresponding VFC was obtained using the following formula:

$$VFC = \frac{NDVI - NDVI_s}{NDVI_v - NDVI_s}$$

Where $NDVI_s$ represents the NDVI value of bare soil (0.1) and $NDVI_v$ the NDVI value of fully vegetated areas (0.9). LST was retrieved from Landsat 8 scenes acquired between June and August 2015–2021 at ~10:00 UTC, each with <10% cloud cover. The LST retrieval process employed the Single-Channel method with NDVI-based emissivity correction (Sobrino et al., 2004), previously applied in similar contexts (Guha et al., 2018; Guerri et al., 2021; Nardino et al., 2022) and providing outputs at 30 m spatial resolution. The resulting LST scenes were aggregated and averaged. The Sky View Factor (SVF) is a dimensionless indicator, ranging from 0 to 1 and quantifying the degree of exposure of a surface to the sky dome—that is, the fraction of the sky hemisphere visible from a given point at ground level (Oke, 1981). For this study, SVF was computed from a Digital Surface Model obtained with LIDAR data with spatial resolution at 1m from the 2007-2017 period.

Air temperature was modeled separately as a function of each predictor variable using linear regression, yielding the following relationships:

$$AirT_{VFC} = -2.49VFC + 25.79 \qquad R2 = 0.89^* \qquad (1)$$

$$AirT_{LST} = 0.599LST + 10.52 \qquad R2 = 0.43^* \qquad (2)$$

$$AirT_{SVF} = 2.33SVF + 35.09 \qquad R2 = 0.86^* \qquad (3)$$

where (2) was taken from Nardino et al. (2022), (3) was estimated using LST data from Landsat-8 and air temperature from the meteorological station of the Regional Hydrological Service of Tuscany (SIR, ID 23), and (4) through ENVI-met simulations performed over 3 study areas (Fig. 5).

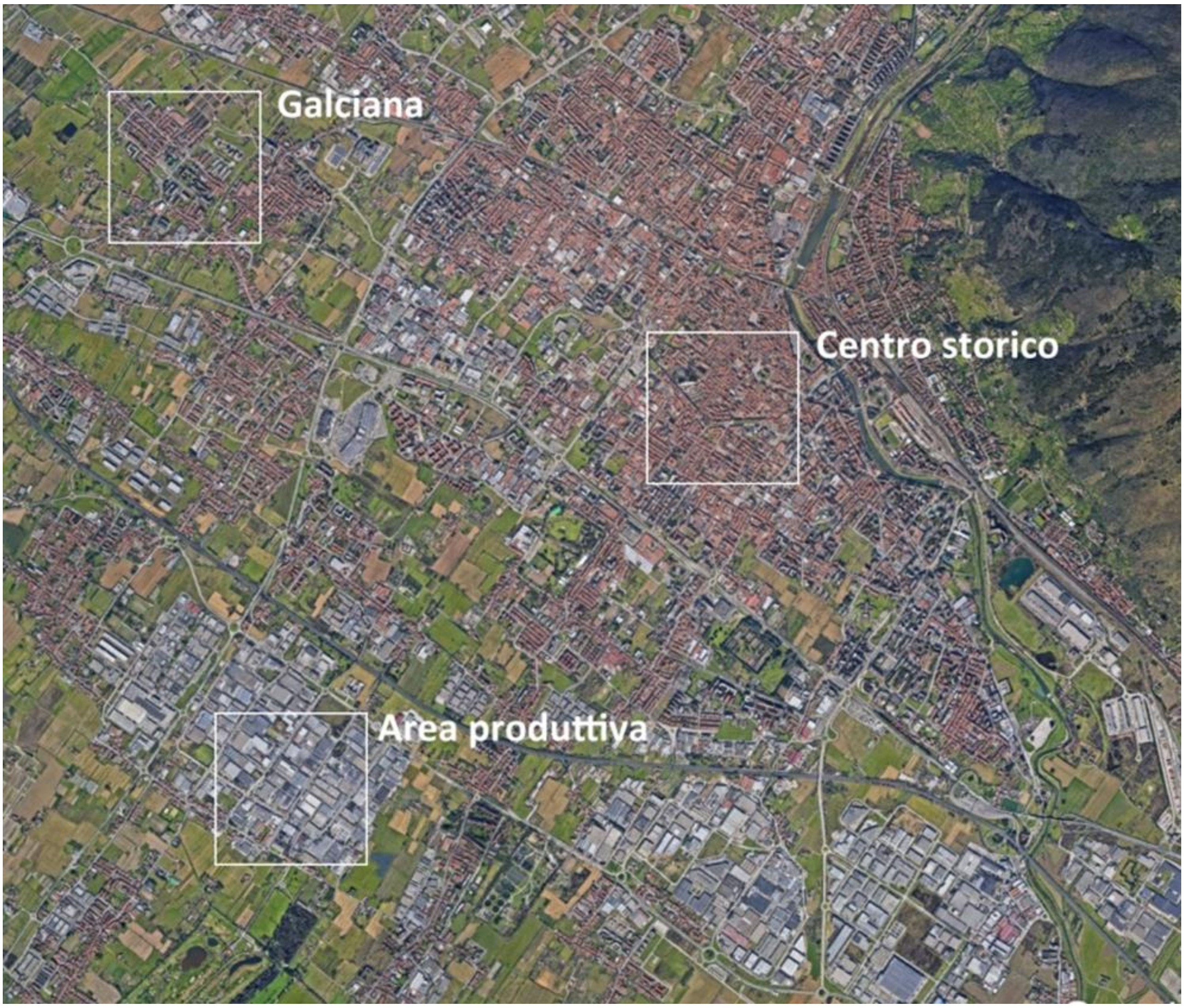

Figure 5. ENVI-met simulations areas used to estimate AirT

To create the final UHTI, (2), (3) and (4) were applied to the corresponding remote sensing inputs, and the resulting estimated $\hat{AirT}_{VFC}$ $\hat{AirT}_{LST}$ and $\hat{AirT}_{SVF}$ for the whole city domain were summed and then normalized between 0 and 1 (eq. 4).

$$UHTI_i = \frac{\left(\hat{AirT}_{VFC,i} + \hat{AirT}_{LST,i} + \hat{AirT}_{SVF,i}\right) - (\hat{AirT}_{VFC} + \hat{AirT}_{LST} + \hat{AirT}_{SVF})_{min}}{(\hat{AirT}_{VFC} + \hat{AirT}_{LST} + \hat{AirT}_{SVF})_{max} - (\hat{AirT}_{VFC} + \hat{AirT}_{LST} + \hat{AirT}_{SVF})_{min}} \quad (4)$$

2.2.4 Socioeconomic data

Socioeconomic data of Prato municipality were obtained from the municipality of Prato at census tract level (i.e., permanent statistical subdivisions of a municipality) by means of three variables: i) Income deciles; ii) Deprivation Index; iii) fraction of elderly residents. Income deciles (I) are the result of a normalization of citizens' absolute income to a scale ranging from 1 (poorest class) to 10 (richest class). These classes were then obtained by disaggregating the municipal districts based on income classes (€), hence representing a synthetic measure of the overall wealth distribution in the study area (Table A2). The Deprivation Index (DI), measuring the socioeconomic discomfort of residents, was built following the methodology proposed by Caranci et al. (2010) and considering four socioeconomic and demographic variables: low education, unemployment, non-home ownership, and population density (Table A3). The higher the values of DI, the greater the probability of social deprivation and low social well-being conditions. Finally, the fraction of elderly people (FEP) was accounted considering all residents older than 65.

2.2.5 Risk components analysis

The risk assessment analysis was based on variables having different spatial representation. Specifically, air pollution and air temperature were in-situ (point) measurements, UHTI was computed at 10-m spatial resolution, and I, DI and FEP were obtained at census tracts level that has a variable geometrical shape and size. Given the heterogeneous spatial representation of these variables, the risk assessment framework was carried out homogenizing the analysis at census tracts and adopting buffer areas for station data. The UHTI for each census tract was firstly averaged at the same spatial resolution of I, DI and FEP. Then, the values of UHTI, I, DI and FEP for each census tracts were accounted for the whole municipality. The station network measurements were considered representative of the underlying area contained within a circular buffer area centered on each station and having a specific radius. Such radius is related to the concentration footprint of each sensor, that reflects the influence of the (mostly upwind) surface on the measured concentration. The size of the footprint depends on the height of the measurement, wind velocity, surface roughness, heterogeneous underlying surfaces, and atmospheric stability (Vesala et al. 2006). In this study a fixed radius value of 500 m was selected, as an optimal distance containing the average concentration footprint peak distances for the encountered atmospheric conditions, while also representing a scale at which residents living near the sensor are likely to be exposed to the environmental hazards' intensity recorded by it—even if they reside outside the strict footprint area.

Census tracts with less than 50% of their area falling into the circular buffers were excluded, resulting in a total of 609 census tracts selected for the analysis. For each circular buffer the average value of DI, I, FEP and UHTI were computed, whilst in-situ measurements of PM concentrations and air temperature were averaged for winter (01/12/2022-28/02/2023) and summer (01/06/2022-31/08/2022) time periods, respectively. Air quality stations with less than 60% valid data were excluded from the analysis, finally resulting in a total of 23 available sites for the analysis (Fig. 6).

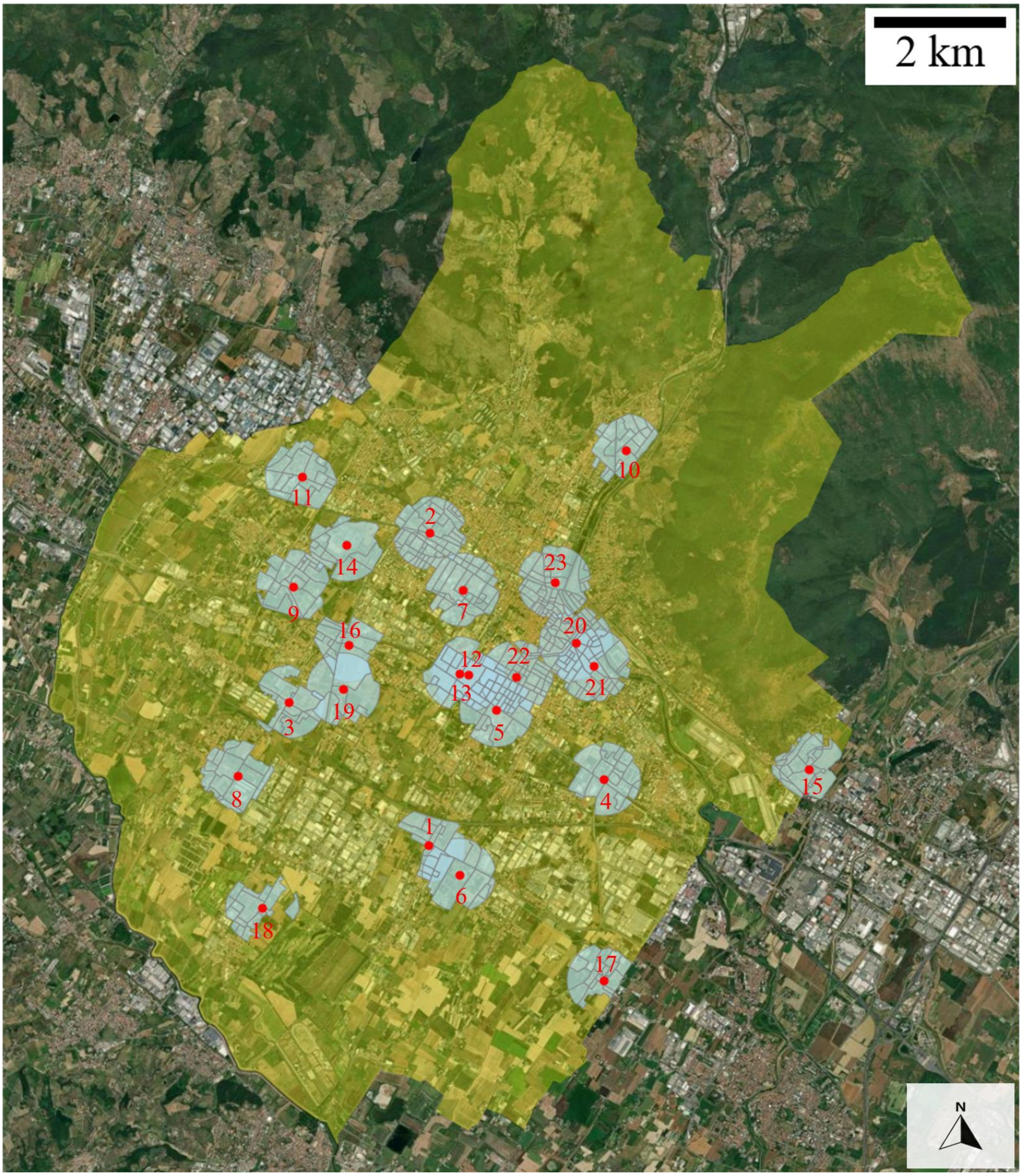

Figure 6. Municipality of Prato (yellow area), including location of air quality stations (red dots), and the census tracts included for the analysis (light-blue areas). Station IDs are reported in Table A3.

The relationships among risk components were investigated through a statistical analysis. PM_{10}, $PM_{2.5}$, AirT, I, DI and UHTI data were sorted in ascending order of income deciles (I), grouped in six classes of similar size, and averaged. Simple linear regressions of vulnerabilities on hazards were performed, and Person's correlation coefficients ($R_{hazard,\ vulnerability}$) and the corresponding 95% confidence intervals were computed (Bonett and Wright, 2000).

A Principal Component Analysis (PCA) was then implemented, using the data aggregated at census tract level and including the FEP. The PCA analysis consisted of three steps. At first the correlation matrix (Table A6) and eigenvalues (λ) were computed, and the Kaiser–Meyer–Olkin (KMO) and Bartlett sphericity tests were run to assess the dataset suitability for PCA (Kaiser, 1974; Tobias and Carlson, 1969). Then the PCA was applied to the dataset after normalization, and the first two principal components (PCs) and their eigenvalues were computed and selected according to the Keiser rule (λ>1; Kaiser, 1960). A bootstrap PCA was performed 1000 times to compute the 5th and 95th percentiles of the eigenvalues representing the lower ($Lpct_\lambda$) and upper ($Upct_\lambda$) bound of the confidence interval to validate the Keiser rule choice (Yu et al., 1998). The third step involved the analysis of the corresponding selected loadings ($l_{\lambda,hazard}$, $l_{\lambda,exposure}$, $l_{\lambda,vulnerability}$) to determine and interpret their contribution to the new components.

2.3 Spatialization of summer air temperature

2.3.1 Framework

The risk assessment framework presented in the previous chapter highlighted the spatial distribution of air temperature, revealing strong and significant microscale variability. Although the dense low-cost monitoring network covered many areas of the city, some zones still remained without observations. To overcome this limitation and achieve complete spatial coverage, air temperature should be mapped using modelling approaches capable of producing fine-scale resolution estimates. The inherent complexity of urban environments, however, makes the estimation of air temperature as an indicator of heat stress particularly challenging. Factors such as land cover, building morphology, vegetation distribution, solar exposure, and local wind regimes create variability in thermal patterns at very fine spatial scales (1–100 m), which can only be adequately captured through measurements with both high spatial and temporal resolution (Oke and Maxwell, 1975). Low-cost sensor networks offer a promising way to overcome this limitation, especially when deployed at high density across large urban areas (Venter et al., 2020).

Integrating remote sensing data with ground-based measurements further enhances the potential for mapping air temperature at fine spatial resolution. Notably, the UHTI (Urban Heat Temperature Index) developed in the previous chapter was based on Landsat-8, Sentinel-2, and LiDAR data products, achieving a 10-m resolution. However, the UHTI, like many other approaches to air temperature modelling over large spatial domains (Janatian, 2016; Venter et al., 2020; Gkirmpas et al., 2025), relied on sparse ground-based measurements, which may bias estimates of thermal patterns during heatwaves. Within this framework, the present chapter focuses on modelling air temperature during an exceptionally warm summer day in the city of Prato, relying on the same inputs' variables used for the construction of the UHTI. First, the relationships of LST, SVF, and VFC with air temperature are examined in order to assess their predictive performance. Then, air temperature is spatially modelled for the entire urban domain.

2.3.2 Remote Sensing Inputs

Landsat 8, Sentinel-2, and LiDAR data were used as inputs to spatialize air temperature at fine spatial resolution. Landsat 8 TIRS imagery from the U.S. Geological Survey (https://earthexplorer.usgs.gov, accessed on 25th February 2024) was employed to retrieve LST from a clear-sky Landsat 8 image acquired on 16 July 2024 (Fig. 7a) around midday (local time) at 30 m resolution, following the USG single-channel emissivity-corrected method. Sentinel-2 Level-2A imagery acquired on 16 July 2024 at 10 m resolution was used to derive vegetation fraction cover (VFC) from NDVI, which was calculated from the red and near-infrared bands and rescaled using the minimum and maximum NDVI values observed in the study area (Fig. 7b). The sky view factor (SVF) adopted here was the same used in the construction of the UHTI (Fig. 7c). All of these inputs were resampled at 10m resolution and harmonized to the 10m spatial grid of Sentinel 2.

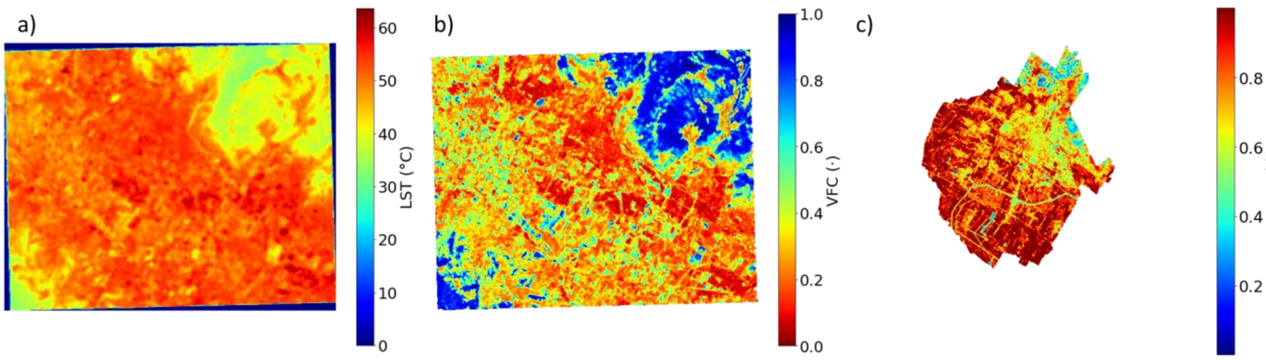

Figure 7. LST (a), SVF (b) and VFC (c) acquired on 16 July 2024 used to model air temperature.

2.3.3 Ground-based measurements

The measurements used for this analysis were focused on a warm summer day from 2024, specifically 16/07/2024. Since this day showed many missing-value data sites, a gap-filling procedure relying on the whole available time series of the low-cost sensors network was adopted to maximize the number of air temperature data. Following Decorte et al. (2024), a K-Nearest Neighbor Estimation imputation method was adopted to gap-fill missing values. Specifically, the imputation method assumes that sensors in the proximity of other sensors provide similar measurements, thus sensors neighboring can impute missing values for the same time point. Assuming that the relationship between two nearby sensors is linear, $X_{m,t}$ missing value can be estimated as function of $X_{m,t}$ through a simple linear regression:

$$\hat{X}_{n,t}^{m}=a+bX_{m,t}$$

Where a and b are estimated from non-missing values ($X_{m,t}$, $X_{n,t}$) pairs. Performing linear regressions for k neighbors, the resulting $X_{n,t}^{m}$ estimates are then combined with a weighted average to obtain the final value:

$$\hat{X}_{n,t}=\sum_{m=1}^{k} w_{nm}\,\hat{X}_{n,t}^{m}$$

With the weight $0<w_{nm}<1$ as function of the distance between m and n such that $\sum_{m=1}^{k} w_{nm}=1$.

As data were gap-filled (Table B1), the models' outputs were validated computing RMSE and R2, while the average air temperature between 12:00 and 16:00 was computed for each sensor.

2.3.4 Urban Heat Modelling

Urban heat was modelled through simple and linear regression models using the same predictors used to construct the UHTI. Specifically, the effects of VFC, LST, and SVF on near-surface air temperature were evaluated by associating the pixel values corresponding to the locations of the low-cost sensor sites with the respective air temperature observations. The models' performances were evaluated, and the coefficients of the multiple linear regression were applied to the city-wide raster predictors to spatialize air temperature. The predicted city-wide temperature was compared to the UHTI using a set of statistical parameters to identify spatial correlations. The Pearson correlation coefficient (R) was employed to quantify the overall linear relationship between the two variables across the study domain, providing a measure of their global correspondence. The Global Bivariate Moran's index (I-Moran) and the bivariate Local Indicator of Spatial Association (LISA) were employed to evaluate the spatial dependency and local clustering patterns between the predicted air temperature and the UHTI, allowing the identification of areas where high (or low) values of one variable spatially coincide with high (or low) values of the other (Moran, 1950; Anselin, 1995). The spatial relationships were determined exclusively by topological adjacency, employing a spatial weights matrix defined through regular-grid contiguity (queen contiguity).

2.4 Irrigation of urban parks as potential cooling strategy for urban summer heat

2.4.1 ENVI-met overview

When addressing how to effectively mitigate the urban heat patterns analyzed and mapped in the previous chapters, ENVI-met represents a suitable modelling tool. ENVI-met has been widely used to assess the cooling effectiveness of various mitigation strategies, including green facades and green roofs, cooling paving materials and irrigation (Tsoka et al., 2018). ENVI-met is a holistic three-dimensional non-hydrostatic model for the simulation of surface-plant-air interactions mainly employed to simulate urban environments. It has been conceptualized for microscale assessments, with simulations usually having a horizontal resolution from 1 to 10 m and a time frame usually below 24 hours because of a high computational cost and a time step of 1 to 5 seconds. Such a resolution allows the reproduction of small-scale interactions between individual buildings, surfaces and plants.

The architecture of the ENVI-met consists of several models interacting with each other within three main computational domains: a 1D boundary domain and a 3D atmospheric and soil domain and discretized using an orthogonal Arakawa C-grid. The 1D boundary domain serves to initialize ENVI-met and to define the boundary conditions of the 3D atmospheric domain – including wind speed and direction and AirT and RH 24-hours diurnal cycle – and vertically extends from the ground surface to approximately 2500 m above ground level (H). The 3D computational domain above the surface is where the investigated study areas are reproduced. It is discretized into an orthogonal grid of $I \times J \times K$ rectangular cells having dimensions $\Delta x \times \Delta y \times \Delta z$ specified with the simulation settings. Within this framework, all elements of the urban environment, including buildings, vegetation, and terrain, are digitized by these cells, which can only be entirely occupied by a single feature or left empty. Consequently, any object whose boundaries are not aligned with the principal axes (x, y, z) must be approximated to the rectilinear grid structure. The horizontal grid spacing (Δx and Δy) is uniform across all grid cells, whereas the vertical resolution (Δz) is typically kept constant in the lower layers of the model and gradually telescoped with increasing height. When the vertical resolution is kept constant, all cells share the same height Δz, with the exception of the lowest layer, which can be further subdivided into five sub-cells. Each of these sub-cells corresponds to 0.2Δz, thereby providing a finer resolution near the surface and improving the model's ability to reproduce the exchange processes between the atmosphere and the surface, which significantly influence the microclimate experienced by people. When the vertical resolution is telescoped, the grid spacing (Δz) increases with height. In this way, the model domain extends vertically up to the top Z while preserving higher resolution near the surface, where the most relevant biometeorological processes occur and the majority of energy exchanges take place. The soil domain, where soil heat and water fluxes are computed, consists of an I × J × N grid, using a telescoping scheme for the vertical discretization. Fluxes and state variables are resolved only along the vertical (z) axis, which renders the soil model effectively 1D despite its 3D grid structure (Huttner, 2012).

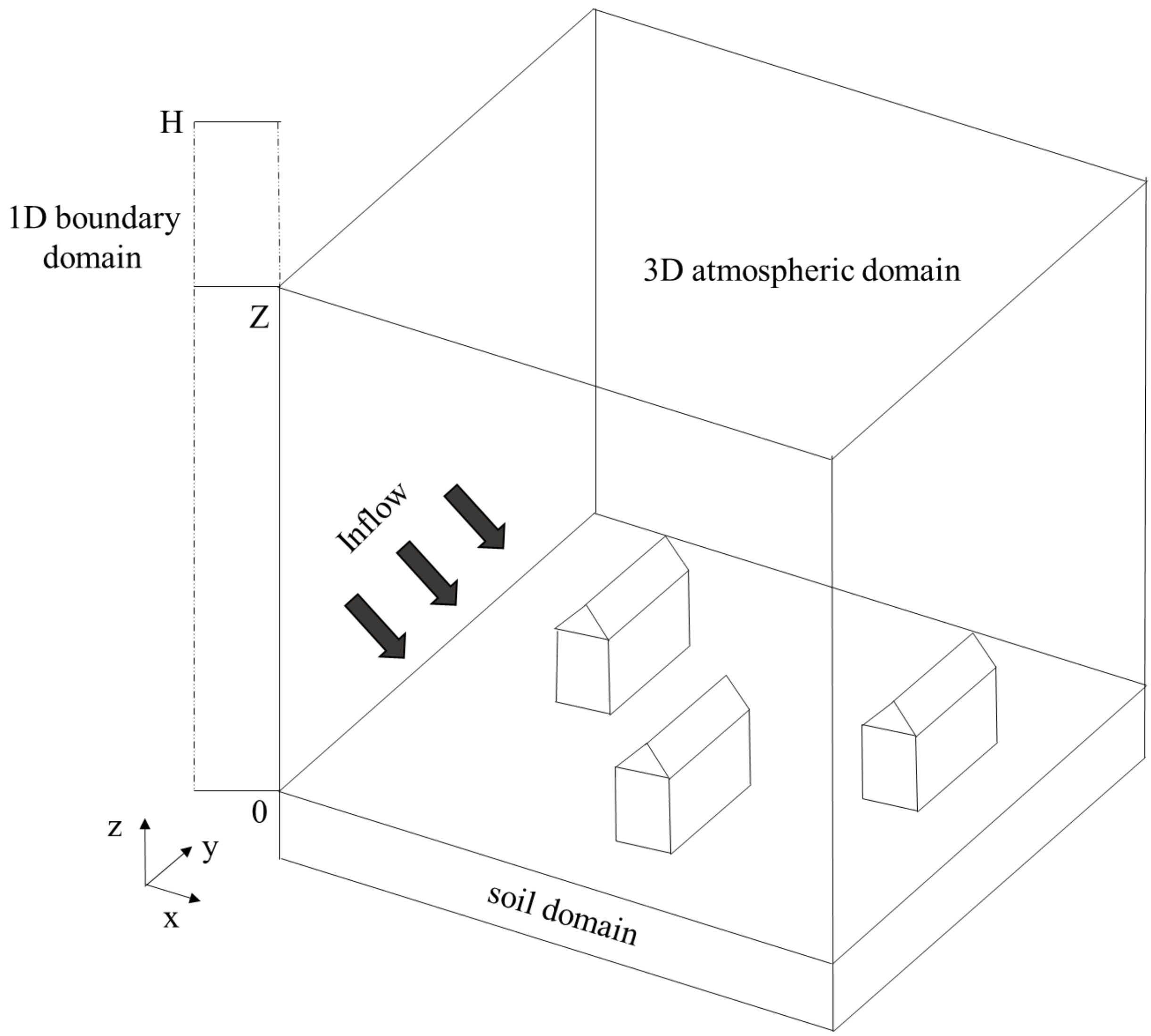

Figure 8. ENVI-met domains scheme

ENVI-met simulations calculate different prognostic variables - including wind flow, air and soil temperature, air and soil humidity, turbulence, radiative fluxes, gas and particle dispersion – through 4 main coupled models (Fig. 9): atmospheric, soil, vegetation, ground surfaces and walls (Bruse et al., 1998). The atmospheric model solves the Raynolds Averaged Navier Stockes equations and computes the mean wind flow, turbulence and exchange processes and radiative fluxes. The soil model determines the distribution of heat and the soil volumetric moisture. The vegetation module represents plant processes such as evapotranspiration, leaf temperature, and shading effects. Finally, the surface and wall modules calculate turbulent fluxes of momentum, heat, and vapor at the ground–

atmosphere and building–atmosphere interfaces. These processes are governed by coupled partial differential equations solved using finite difference methods.

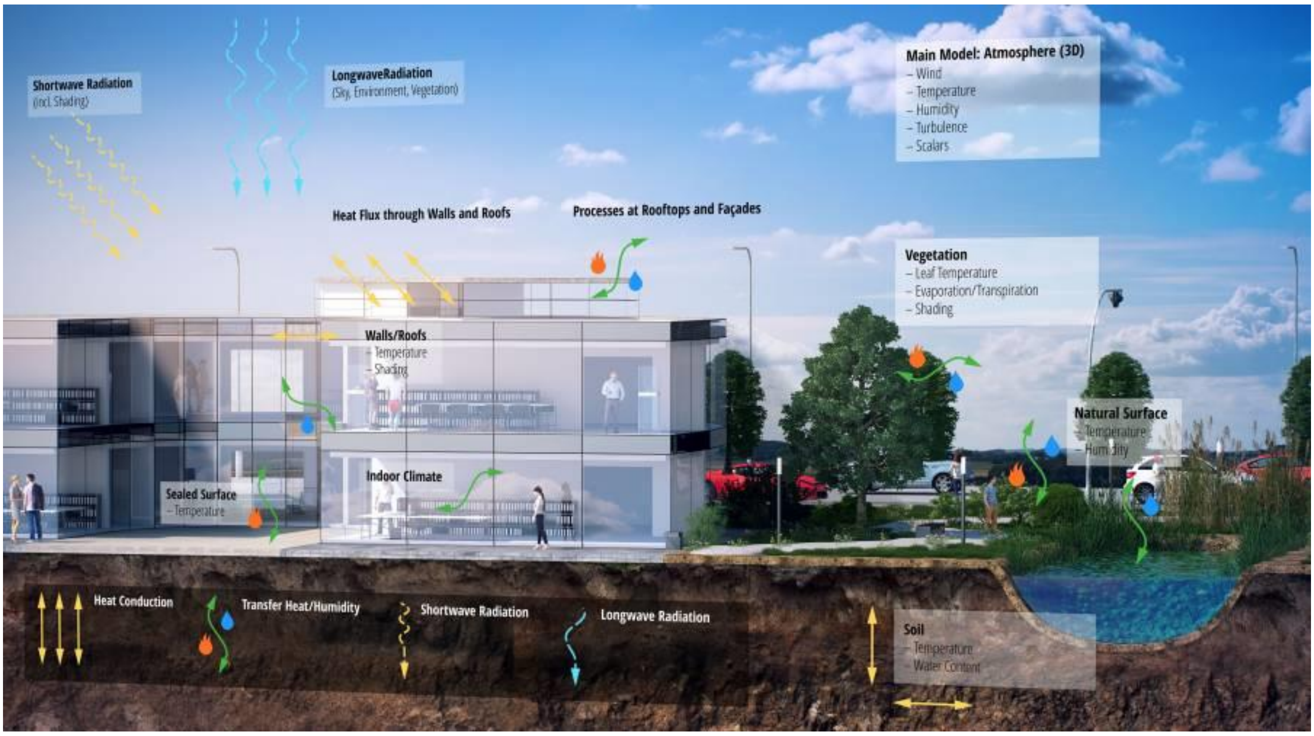

Figure 9. Schematic of the coupled models (ENVI-met: a holistic microclimate model)

Because of its complex architecture enabling the reproduction of the complex interactions occurring between atmosphere-soil-surface and vegetation, ENVI-met is able to simulate the potential cooling effectiveness coming from enhanced soil water content and water dispersion in the air. According to ENVI-met version and previous studies (Gobatti et al., 2024; Scharfstädt et al., 2024; Di Giuseppe et al., 2021), three strategies were identified to reproduce these processes: i) by increasing initial soil moisture conditions of the simulation, ii) forcing precipitation at a specific hour of the day and iii) directly placing water nozzles in the 3D reproduced study area. The increase of initial soil moisture conditions of natural soils relies on the modification of the soil water content at the beginning of the simulation (SWC_{IN}) to reproduce the wetting of the upper soil layers following a prior irrigation event. Forcing precipitation can be employed to represent a more dynamic representation of irrigation timing and duration, directly affecting soil moisture evolution, surface flux partitioning, and subsequent thermal responses. Finally, the use of water nozzles within the 3D domain simulates detailed and spatially explicit spray or mist irrigation systems, which disperse water droplets in the air that either evaporates or are subject to a sedimentation process (Di Giuseppe et al., 2021).

Relying on ENVI-met robustness, the model was first validated under contrasting water-management conditions (irrigated vs. non-irrigated) and subsequently applied to eight urban parks in Prato (Italy), representing two microclimatic classes (inner-city, IC and near-river, NR) and four tree-density classes. ENVI-met was used to simulate the thermal mitigation provided by four irrigation scenarios and to quantify their associated irrigation costs. An integrated economic analysis was then conducted by combining total irrigation costs and air-temperature reduction (ΔAirT) across paired IC–NR scenarios, with values averaged over tree-density classes. The novelty of this chapter lies in its fully integrated framework, which couples high-resolution in situ microclimatic measurements (i.e., air temperature and relative humidity), detailed urban vegetation characterization, and process-based modelling to quantify irrigation-driven cooling in urban green spaces. By explicitly linking thermal mitigation to irrigation costs across contrasting urban microclimates, this part of the thesis provides a robust and operational cost–benefit assessment of irrigation as a climate-adaptation strategy for urban parks.

2.4.2 Areas of simulations

The study sites consisted of two green areas (Fig.10 - yellow dots) selected for model validation, and eight additional urban parks (Fig.10 - red dots) to assess the cooling potential associated with different water management strategies, resulting in a total of 10 study sites. The two validation sites were characterized by different water management (i.e., irrigated vs rainfed). The irrigated site (9) was a golf club with continuous nighttime irrigation, while the rainfed site (10) was a nearby dry green area. These sites were selected for their i) close spatial proximity and similar soil and vegetation characteristics, ii) closeness to the network of local meteorological stations providing robust data for model initialization, and iii) the availability of an accessible irrigated green area with known irrigation inputs. The eight urban parks selected for the modelling assessment of cooling potential were chosen because they belong to two classes representing distinct local microclimatic conditions (i.e., warmer and cooler) and exhibit different tree-density.

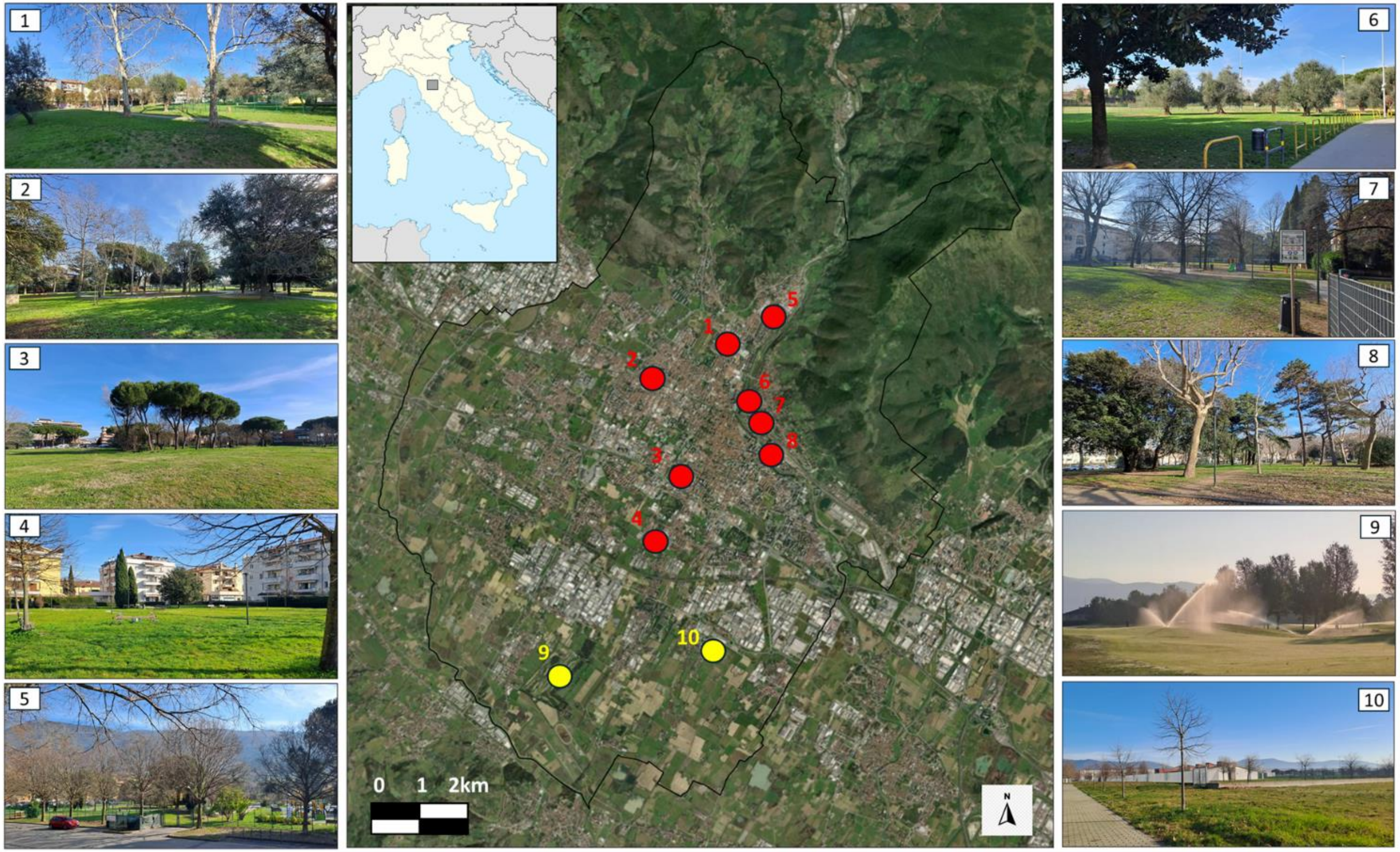

Figure 10 Location of the Municipality of Prato (Italy) and spatial distribution of the ten study sites, including pictures of selected urban parks (left and right sides). Two urban parks selected for model validation are shown as yellow dots (9, 10) in the southern part of the municipality, while eight urban parks selected for the modelling assessment of cooling potential are indicated by red dots (1-8).

2.4.3 Ground-based measurements and microclimate classification

Ground-based data consisted of measured SWC, AirT, and RH data. The SWC data was retrieved from a one-day field campaign carried out on 15 July 2025 at both validation sites using a Time Domain Reflectometry (TDR). At each site (i.e., irrigated and rainfed), 10 measurements were taken at approximately two-hour frequency (i.e., 7:00; 9:00; 12:00; 15:00; 17:00 and 19:00) at 3.5 cm depth, for a total of 140 measurements. For each site, measurements were then averaged within each time window to obtain six observed SWC values describing the daily pattern (Tab. C1), which were then used for tuning and validating the model.

AirT and RH data were collected from the AirQino sensors network. To characterize the summer microclimatic conditions in Prato, AirT and RH data were collected from all monitoring stations for the June–August period of the year preceding the experiment (2024). Since the year 2025 was selected for modelling simulations and the experimental campaign (15th of July), the 2024 dataset was used as climatic reference to capture the full summer variability. AirT was averaged over the entire 2024 summer period and classified into five temperature classes with 0.4 °C intervals to characterize different thermal zones within the Municipality during the warm season (Fig. 11). Based on this procedure, two main thermal classes were visually identified: i) a warmer inner-city area (IC, red area) and; ii) a cooler near-river area (NR, blue area) (Fig. 11, Fig. C2a). Finally, to ensure consistency with SWC data, high-frequency AirT and RH were extracted for the IC (including 17 AirQino stations) and NR (including 6 AirQino stations) microclimate classes on 15 July 2025, and then hourly averaged for each class to be used as initial conditions in the modeling simulations (Fig. C2b).

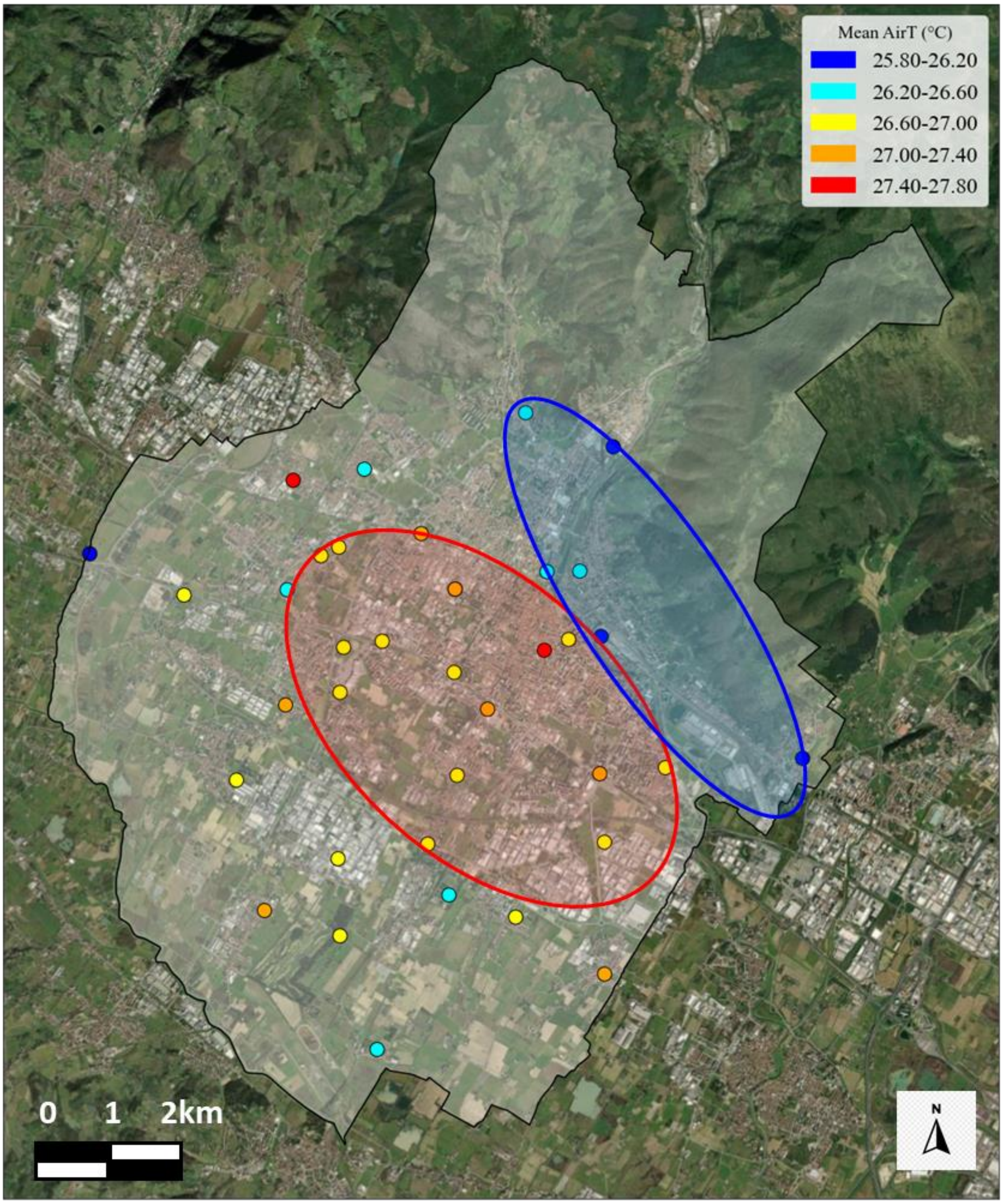

Figure 11. Mean AirT averaged over the June–August 2024 period and classified into five temperature classes with 0.4 °C intervals, used to delineate warm-season thermal zones within the Municipality. Two distinct thermal microclimate classes were identified: an inner-city class characterized by higher temperatures (red area) and a cooler class located in the north-eastern sector surrounding the city center (blue area).

2.4.3 Selection of the urban park case studies

A database containing detailed information (e.g., geographic coordinates, number of trees, area, and other structural attributes) on public green spaces equipped with recreational facilities and services within the Municipality of Prato was used to extract and characterize the existing urban parks (http://odn.comune.prato.it/dataset/giardini-attrezzati). The database reported a total of 53 urban parks, which were extracted, georeferenced, and classified according to tree-density, calculated by applying a min–max normalization to the number of trees per hectare across all 53 parks (Fig. C2). Then, all 53 parks were further grouped into four classes representing equal tree-density quartiles (25% each) (Fig. 12, Tab. C2).

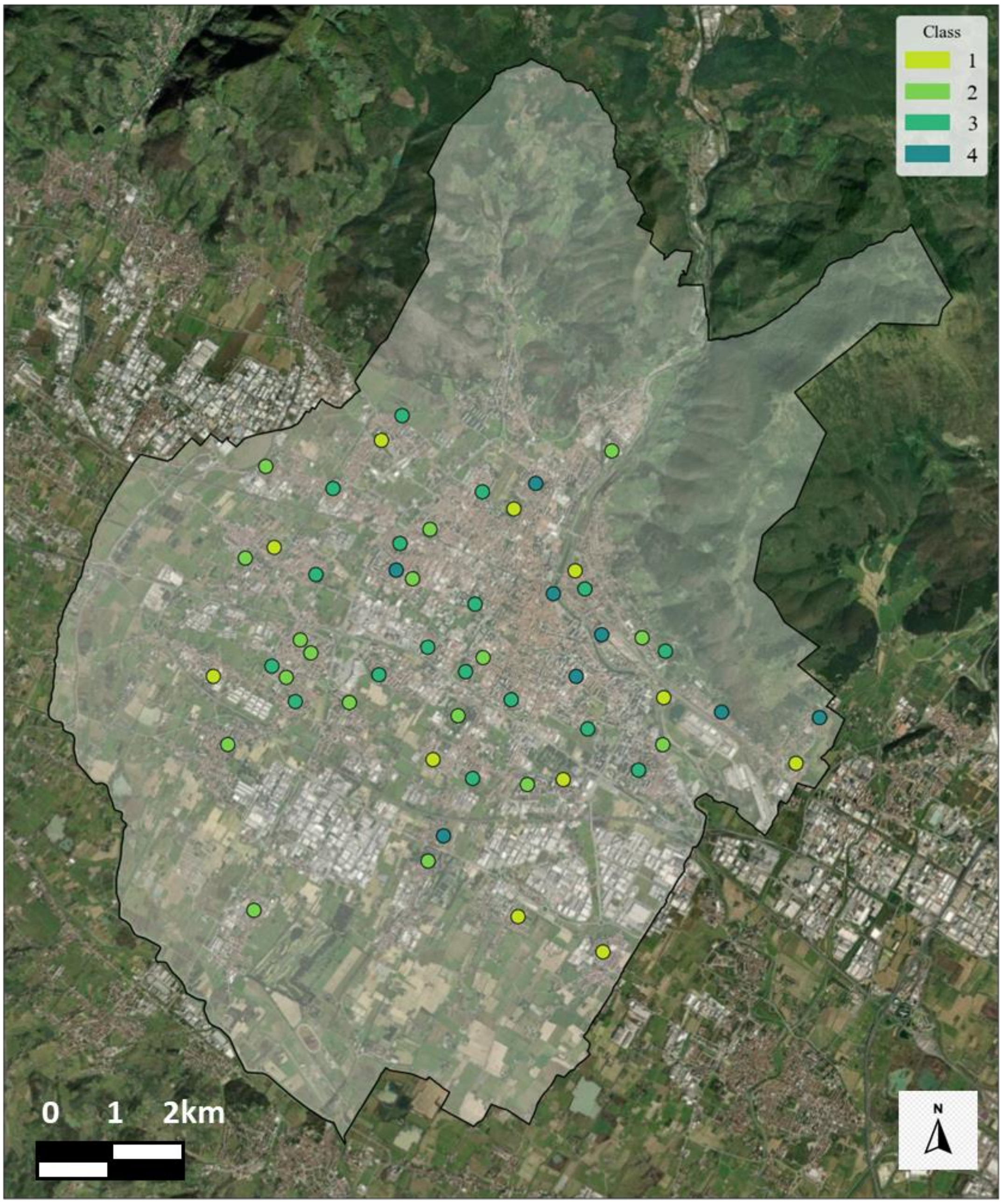

Figure 12. The 53 urban parks located in the Municipality of Prato and grouped into four classes representing equal quartiles (25% each) of tree-density calculated by applying a min–max normalization to the number of trees per hectare across all 53 parks.

For each microclimate class (IC and NR) four parks, each one representing a different tree-density class were selected, resulting in a total of eight urban parks (Tab. 2). The two parks belonging to Class 1 were used as baseline to assess the tree-density effect on thermal mitigation (see section 2.6).

Urban Park		Lat.	Lon.	Area	Microclimate classes	Normalized Tree-Density (NTCD)	Tree-Density (CL)
Name	**ID**	**(°E)**	**(°N)**	**m^2**	**ID**	**(0-100%)**	**Class**
Capponi	NR01	43.89	11.1	13480	Near-river (NR)	4.38	1
Magnolfi	NR02	43.9	11.11	6561		48.22	2
Giocagì	NR03	43.88	11.11	15485		52.35	3
Stazione	NR04	43.88	11.11	16053		88.60	4
Grignano	IC01	43.86	11.08	8817	Inner-city (IC)	10.98	1
Nenni	IC02	43.89	11.08	11868		31.87	2
Campaccio	IC03	43.87	11.09	10500		61.19	3
Puccini	IC04	43.9	11.1	9610		75.00	4

Table 2. Characteristics of the urban parks used for ENVI-met simulations, including geographic coordinates, area, distance from Bisenzio river, Tree Cover Density Class and Normalized Tree Cover Density.

2.4.4 Model validation and development of irrigation scenarios

To assess ENVI-met model reliability at reproducing daily courses of air temperature, relative humidity and soil water content under both rainfed and irrigated conditions, the model was validated in two green areas characterized by different water management (i.e., irrigated vs rainfed).

Firstly, the two sites were reproduced within the Space module of ENVI-met (Fig. 13). The irrigated site (A) was configured with horizontal grids having a resolution of 5 m, resulting in a horizontal model area of 345×345m. Concerning the vertical resolution, 25 grids were configured at 3 m resolution, with the lowest grid divided into 5 sub-grids, and with a telescoping factor of 20% applied to the grids above 30m heights. This approach was adopted to define the impact of the microclimatic variables - that mostly affect human health - at a finer resolution. By contrast, the rainfed area (B) was simulated with the same vertical resolution but a finer horizontal resolution of 2 m, yielding a horizontal areal extent of 150×192 m.

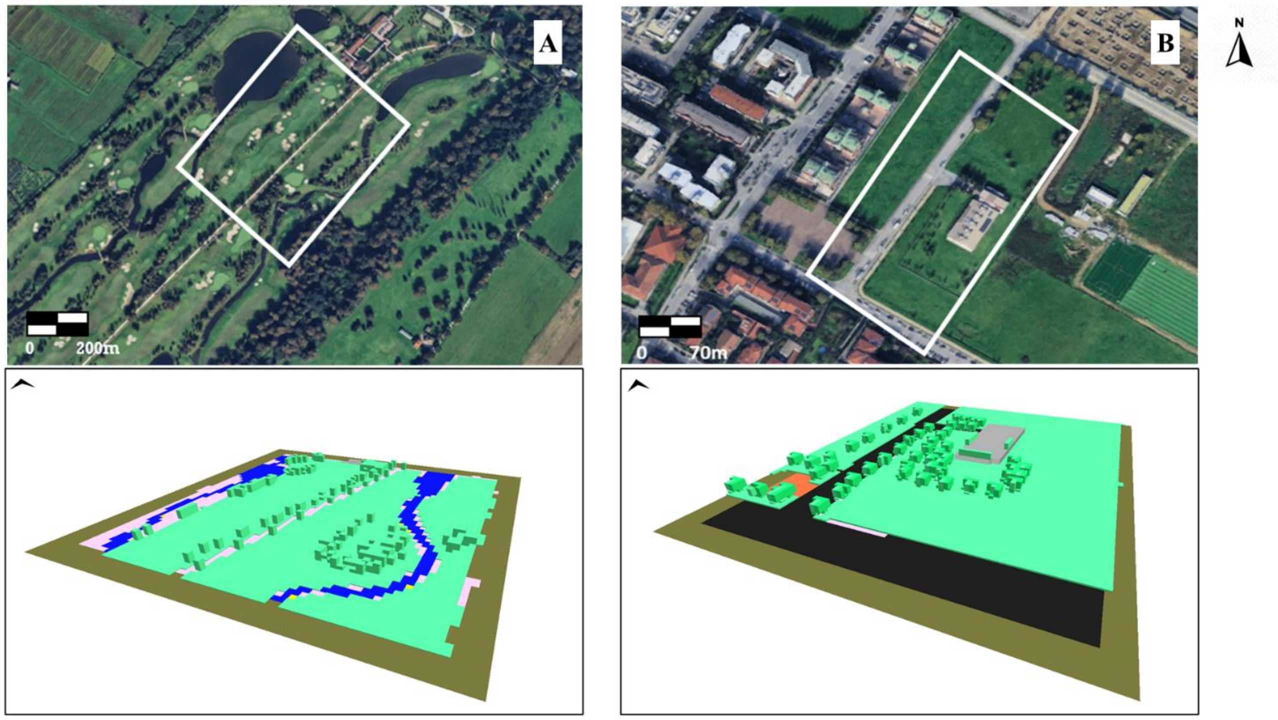

Figure 13. Satellite images and corresponding three-dimensional representations developed with the ENVI-met model for the irrigated (A) and rainfed (B) urban green areas used for modelling validation and tuning.

Model configuration included soil properties, vegetation parameters and meteorological boundary conditions. Vegetation was simplified by representing tree cover with medium-height trees and ground cover with user-defined grass of 10 cm height, while surrounding buildings were reproduced using data of standard concrete material and building heights obtained from an open access database managed by the Municipality of Prato (http://odn.comune.prato.it/dataset/edificato-prato). Boundary meteorological conditions were prescribed in the simple-forcing configuration file and consisted of hourly air temperature (AirT) and relative humidity (RH) data for both irrigated and rainfed sites. The forcing dataset was built using the average of hourly values for the 15 July 2025 extracted from IDs 18, 26, 29 and 33 for the irrigated site, and IDs 01, 06, 17 and 29 for the rainfed site (Tab. C3). Daily wind speed and direction were extrapolated by the meteorological reference station managed by the

Regional Hydrological Service of Tuscany (SIR) for the Municipality of Prato (ID=23). Soil properties were selected for both sites using clay loam texture and related model default properties.

After model setup, soil hydraulic properties were tuned to reproduce the measured soil water content (SWC) at the irrigated site. The tuning involved the adjustment of soil key parameters, including water content at saturation, field capacity, wilting point, matric potential, hydraulic conductivity, volumetric heat capacity, and the Clapp and Hornberger constant (Tab. C4). After the tuning of soil properties, the initial soil water content for the 0–20 cm soil layer was set from 0.227 (default value) to 0.270 for the irrigated site ($SWC_{IN, irr}$) and to 0.139 for the rainfed site ($SWC_{IN, not-irr}$). Model performance was evaluated with observed data at both irrigated and rainfed sites. Hourly diurnal cycles of SWC, AirT, and RH were compared between simulations and measurements, and model accuracy was assessed using the coefficient of determination (R2) and the root mean square error (RMSE).

Irrigation scenarios were built by varying the initial soil water content (SWC) to represent different irrigation levels. This approach resulted in five scenarios: one baseline non-irrigated scenario (BS) and four alternative irrigation scenarios (AS). BS was initialized with an initial soil water content ($SWC_{IN, not-irr}$) of 0.139, while the four alternative scenarios were generated by modifying the initial SWC in the 0–20 cm soil layer using evenly spaced increments between the wilting point (0.21) and field capacity (0.31) derived from the tuned soil hydraulic properties (Tab. C4). Specifically, initial SWC values were set to 0.21, 0.24, 0.27 (corresponding to the validated irrigated configuration), and 0.30, which were assigned to AS1, AS2, AS3, and AS4, respectively.

2.4.5 Model validation and development of irrigation scenarios

Thermal mitigation capacity was simulated in the eight selected urban parks based on four tree-density cover and five irrigation scenarios, resulting in a total of 40 different scenarios simulated.

The eight selected urban parks were created with a spatial resolution of a 2 m horizontal resolution and the same vertical resolution adopted for model validation (Fig. 14).

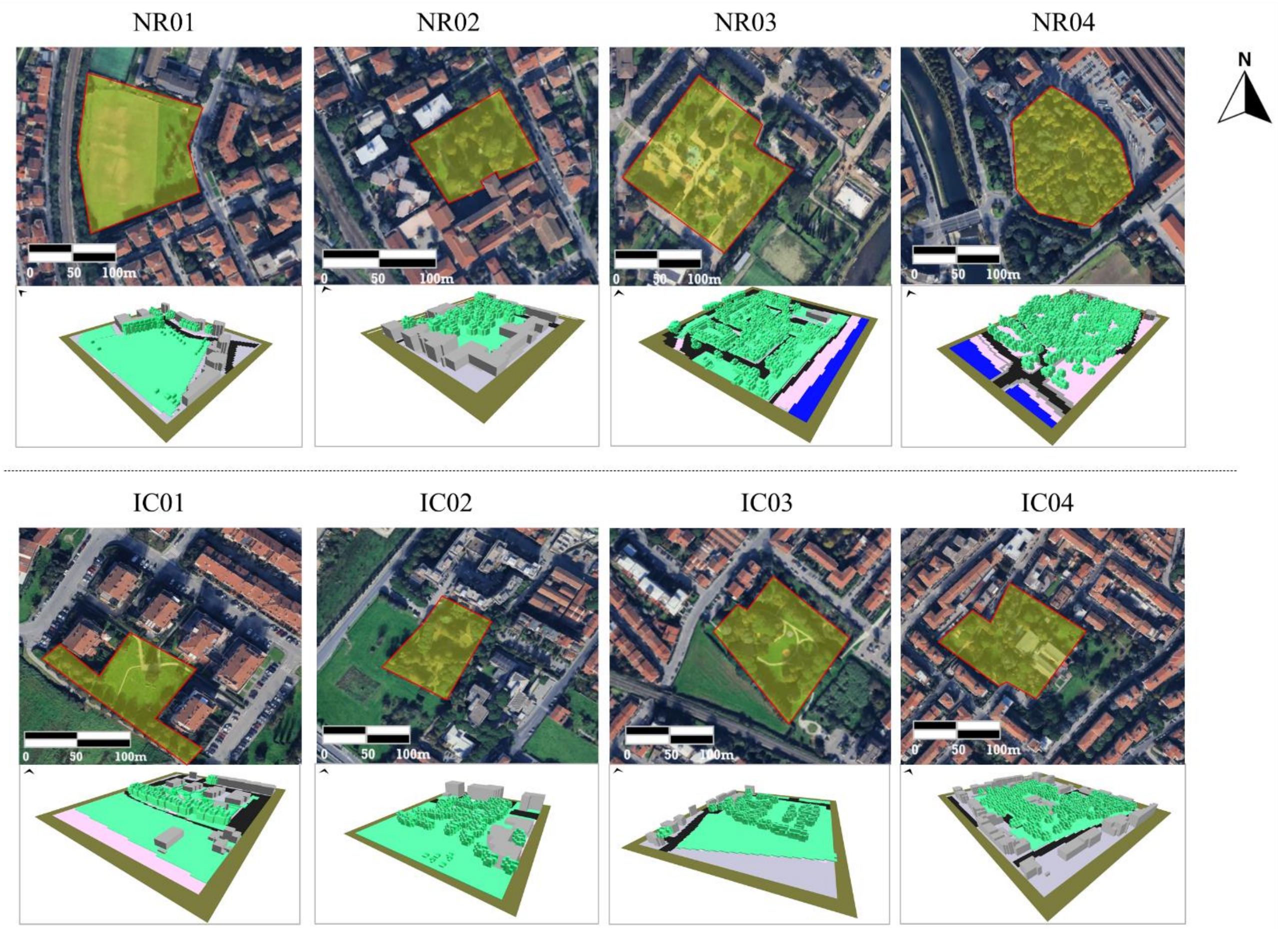

Figure 14. Satellite images extracted from Google Earth and corresponding three-dimensional representations developed with the ENVI-met model for the eight urban green areas, grouped into Near-River (NR, top) and Inner-City (IC, bottom) microclimate classes across increasing tree-density classes (01–04).

Across all sites, vegetation and soil properties were kept consistent with those defined during model validation, with the only exception for SWC, which was adjusted for each simulation according to the irrigation scenario being adopted. This approach allowed to minimize the influence of site-specific differences in soil characteristics and vegetation structure on water availability, thereby isolating the effects of irrigation on the simulated thermal patterns. Boundary meteorological conditions (i.e., hourly AirT and RH) related to 15 July 2025 were then associated with each park according to the microclimate class to which the park belonged. This strategy was implemented to reduce the influence of local atmospheric variability among sites and to ensure that differences in simulated thermal responses were primarily driven by irrigation-induced changes in soil water availability. Accordingly, four parks were initialized using boundary meteorological conditions representative of inner-city class (IC), while the remaining four parks were initialized using the near-river class (NR) (Fig. C1b). Wind speed and direction were prescribed consistently with the values adopted during model validation.

For each park, diurnal courses of microclimatic (AirT, RH at 2.7m height), soil state (SWC) variables, and surface energy balance fluxes (latent heat flux, LE; sensible heat flux, H) were computed by averaging pixel-level hourly data within the park domain (Fig. C5 and C6). The resulting diurnal courses were evaluated by comparing the baseline and irrigation scenarios, while also accounting for the combined effects of microclimatic conditions and tree-density.

To assess the thermal mitigation potential provided by irrigation and tree-density during the warmest hours of the day, AirT was averaged over the time-window 12:00–16:00 and grouped into eight classes at 0.5 °C intervals. Differences in mean AirT were then calculated by comparing the baseline non-irrigated scenario with the four alternative irrigation scenarios (AS1–AS4), and the baseline tree-density class (CL1) with the higher tree-density classes (CL2–CL4). This approach allowed evaluation of both the combined influence of irrigation and tree-density and the individual contribution of each factor to thermal mitigation.

2.4.6 Economic analysis

The potential costs for all urban park irrigation scenarios were assessed by integrating the total amount of water (m^3) used for irrigation in each park with the related cost for the whole water supply chain (i.e., distribution, wastewater collection and conveyance management, and secondary wastewater treatment). Firstly, the amount of water used for irrigation was derived for each irrigation scenario from the Total Available Water (TAW) formulation (Allen et al., 2000):

$$m^3 = (SWC_{IN,\,i} - SWC_{IN,bs})\ Z_r \cdot 10^6$$

where i= {1,2,3,4} refer to the alternative irrigation scenarios (i.e., AS); bs=baseline not irrigated; and Z_r = 0.20 m which represents the thickness of the soil layer where SWC_{IN} was changed.

Then, the cost for the whole water supply chain was taken by the water-bill simulation tool provided by Publiacqua S.p.A (https://www.publiacqua.it/). Publiacqua S.p.A. is the main water utility managing the integrated water service in the provinces of Florence, Prato, Pistoia and Arezzo, responsible for drinking water supply, sewage and wastewater treatment, serving about 1.3 million residents across 46 municipalities. The cost of the water supply chain was extracted for the day of simulation (15 July 2025) and included the cost for water supply and distribution (Aqueduct, A), wastewater collection and conveyance management (Sewer, S), and secondary wastewater treatment (SWT) each one at 1 m^3 resolution. Based on the water-bill simulation tool, the costs for A, S and SWT were set at 1.79, 0.89 and 0.79 € m^{-3}, respectively. Once the potential cost for each of the 40 scenarios was accounted (Tab. C5), an economic assessment was performed by aggregating irrigation costs across the two microclimatic classes (IC and NR). For each class, total irrigation costs were first calculated by summing the costs of the four parks representing different tree-density classes under each irrigation scenario (baseline, AS1–AS4). The aggregated costs for IC and NR were then combined pairwise to generate a set of integrated economic scenarios. This approach resulted in 25 combinations, ranging from the fully non-irrigated configuration (IC_BS + NR_BS) to the maximum irrigation configuration (IC_AS4 + NR_AS4). The economic analysis was then visualized by ranking the total costs of the 25 integrated scenarios from lowest to the highest together with their corresponding thermal mitigation capacity, expressed as air-temperature reduction (ΔAirT). In addition, the air-temperature reduction achieved per euro of irrigation cost (°C $€^{-1}$) was computed and normalized (0-1) into a cooling-efficiency index. This representation enabled a direct comparison between costs and cooling performance, thereby highlighting the cost–benefit relationship between irrigation investment and the associated thermal mitigation effect.

3. Results

3.1 Risk assessment components analysis

3.1.1. Spatial data analysis

The risk components averaged at census tract level showed heterogeneous spatial pattern within the city. The average values of I, DI, UHTI and FEP were 6.6±1.5, -0.03±2.3, 0.68±0.08 and 0.23±0.12, respectively. I and DI showed an opposite pattern, confirming that, as largely expected, wealthy areas were generally affected by lower levels of material deprivation (Fig. 15a,b). Areas with higher Income and lower Deprivation Index were mainly found in northern and southern peri-urban areas, while central areas showed complex clusters of different classes, with a variable presence of more vulnerable population.

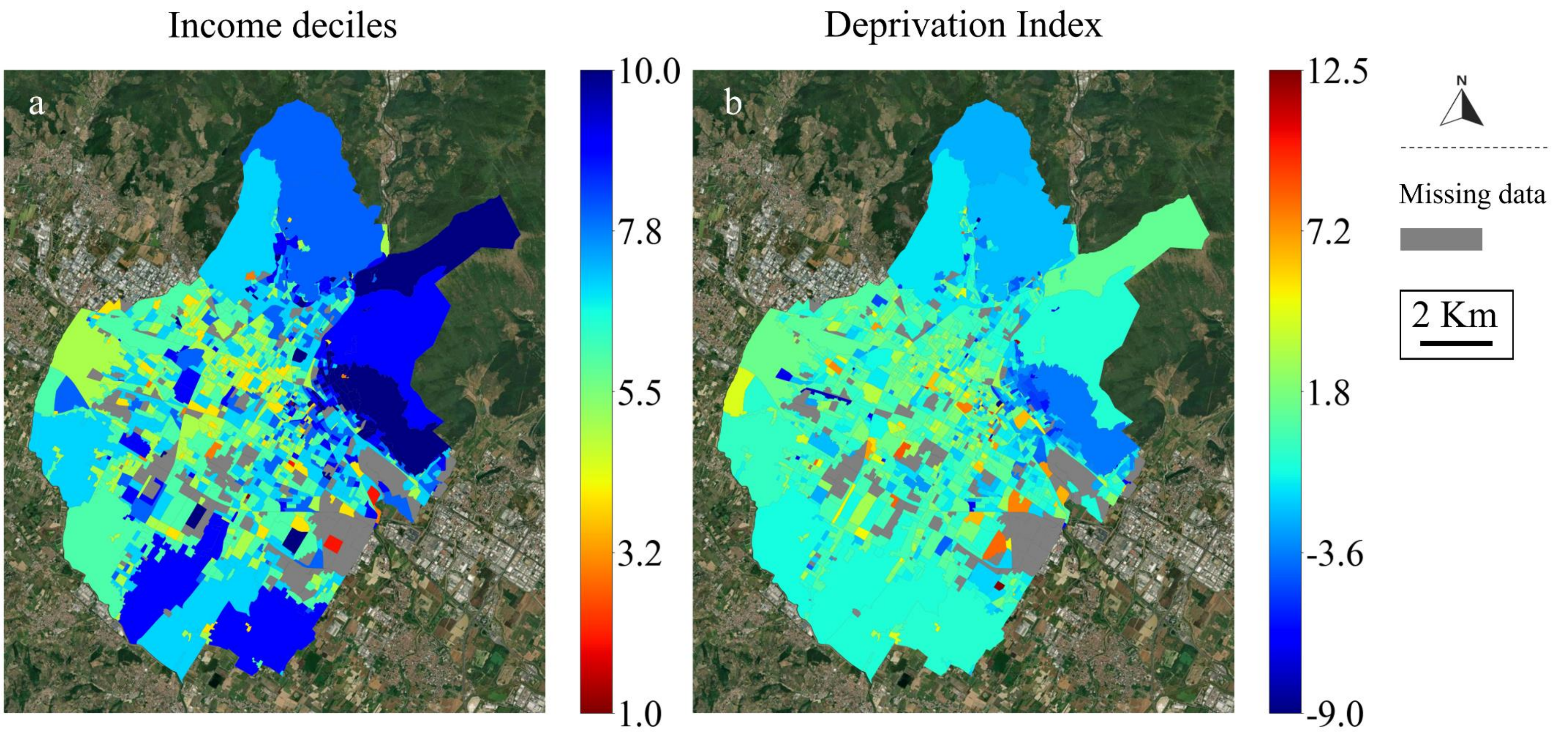

Figure 15. Income deciles (a) and Deprivation Index (b) averaged at census tract level for the whole municipality of Prato.

Higher UHTI values were observed in the downtown and in the large industrial districts south of the city (Fig. 16a), while lower values were mainly observed in the peri-urban green areas and, particularly, in the northern hilly-green area. By contrast, FEP distribution was heterogeneous (Fig. 16b), with contrasting neighborhoods conditions. The fraction of elderly people above the average was generally observed outside the city center.

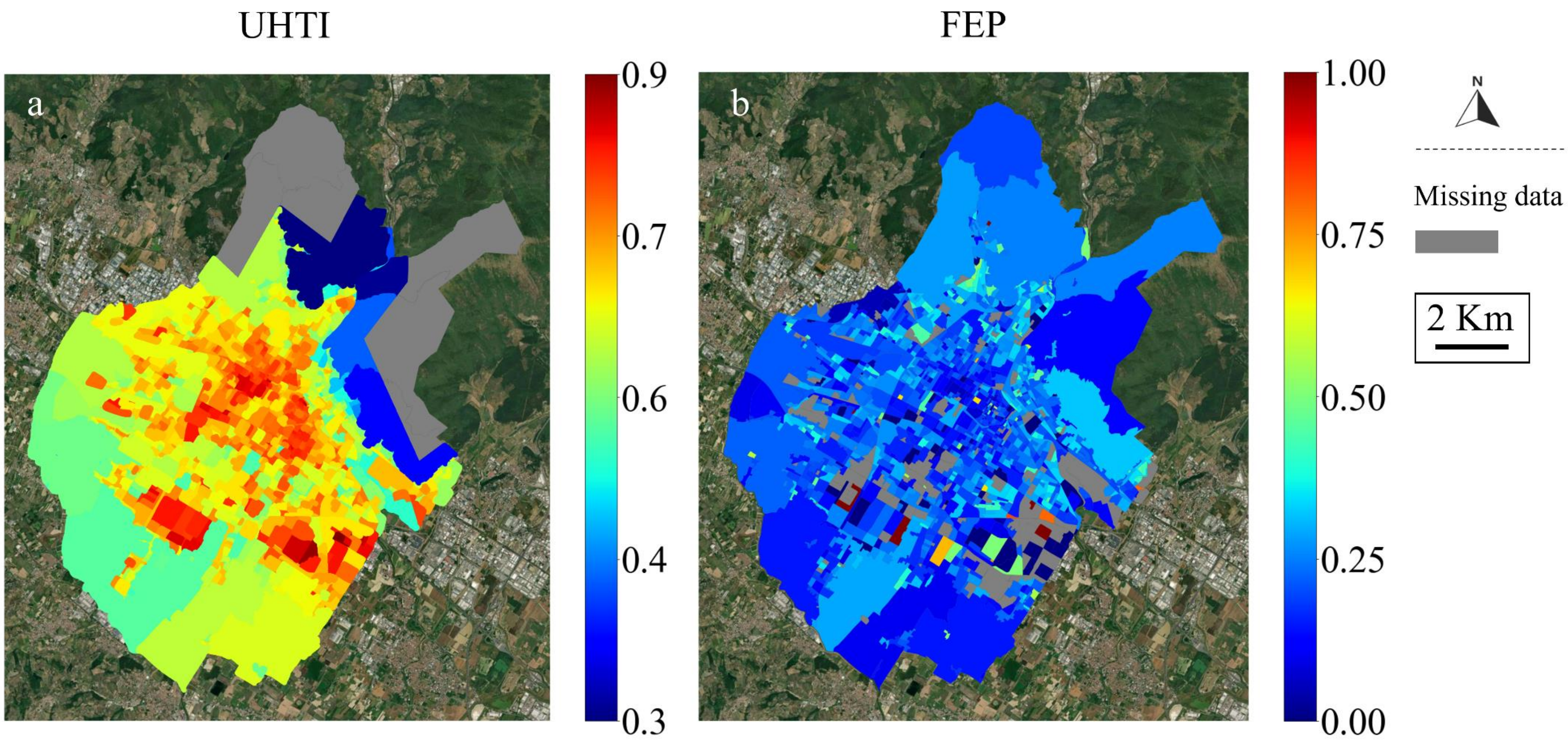

Figure 16. Average UHTI (a) and Fraction of Elderly People (b) at census tract level.

3.1.2. Station network data analysis

The average particulate matter concentration during wintertime were 26.4 µg m^{-3} (PM_{10}) and 16.7 µg m^{-3} ($PM_{2.5}$, Table A5). The highest values were observed for ID 08 (PM_{10}=50.1 µg m^{-3} and $PM_{2.5}$=27.1 µg m^{-3}) and 03 (PM_{10}=48.7 µg m^{-3} and $PM_{2.5}$=25.1 µg m^{-3}, Table A5), which are located in the central-western area characterized by a major road and several industrial activities (Fig. 15). By contrast, the lowest concentrations were found for ID 07 (PM_{10}=14.6 µg m^{-3} and $PM_{2.5}$=11.6 µg m^{-3}, Table A5), located in a green and low-traffic area including the city hospital (Fig. 17).

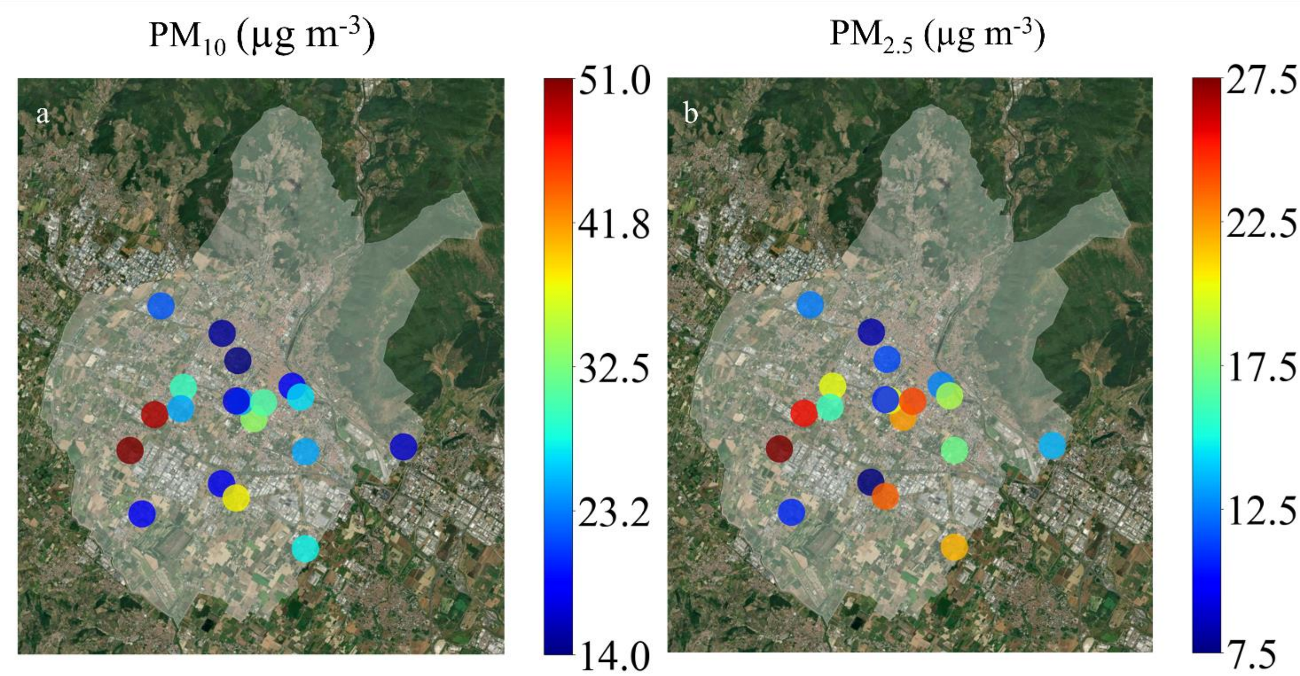

Figure 17. Winter (01/12/2022-28/02/2023) average PM_{10} (a) and $PM_{2.5}$ (b) concentrations at each monitoring site.

Mean air temperature during summertime ranged between 26.5 and 28.5°C (Fig. 18), with an average of 27.7 °C (Table A5). Air temperature typically exhibited lower values in peri-urban areas, especially in the northern green hilly areas for ID 10 (26.5 °C) and 15 (27.0 °C (Table A5), and higher values in downtown for 07 (28.5 °C) and 02 (28.4 °C).

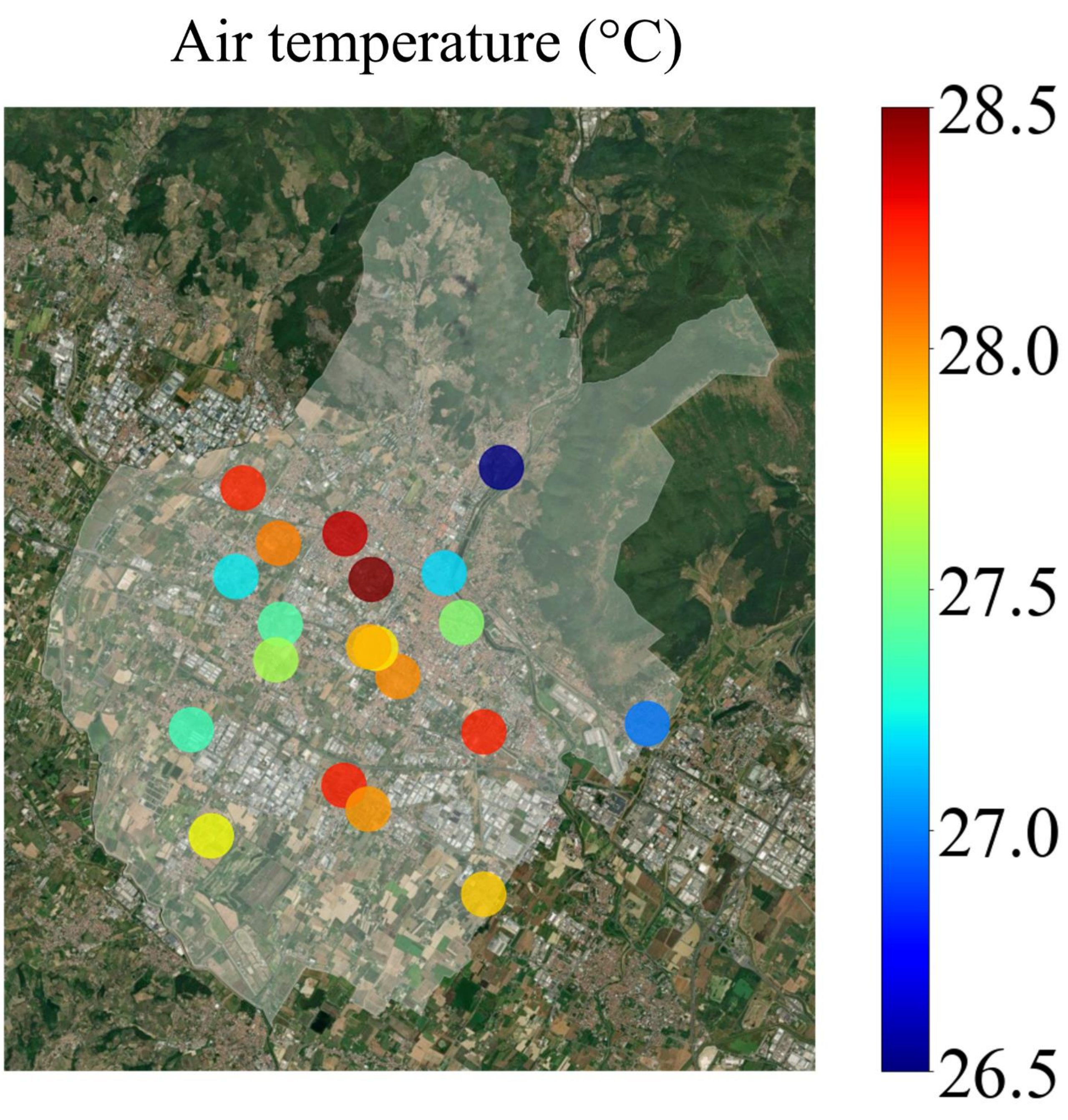

Figure 18. Average summer-season (01/06/2022-31/08/2022) air temperature (°C) computed at each monitoring site.

After the extraction of the spatial data (Fig.17 and Fig.18) at each station buffer, UHTI showed the highest values (0.76±0.03) at ID 07, while the lowest (0.63±0.05) at 01 (Table A5 and Fig. A4). The highest deprivation index (DI) value was observed at ID 19 (1.58), while the highest fraction of elderly people (FEP) at 04 (0.32). The IDs 07 and 15 showed an opposite pattern for FEP and DI, with 07 reporting the second highest DI (1.30±0.3) and the lowest FEP (0.14±0.01), and 15 reporting the lowest DI (-0.94±0.4) and the second highest FEP (0.31±0.02, Table A5 and Fig. A4). For income deciles (I), the highest value (7.4±0.2) was observed at ID 15, 20 and 21, while the lowest (5.3±0.1) at 07 (Table A5 and Fig. A4).

In Fig. A5 the wind rose and wind speed percentile rose observed at the Prato Università meteorological station (ID 23, Fig. 6) during the 01/12/2022-28/02/2023 period are presented. Overall, North-East is the largely prevailing wind sector (22%), followed by the East-North-East (10%) and East-South-East (9%) sectors (Fig. A5a). The predominant North-East winds are also the strongest, as they exhibit a mean value of 2.8 and maxima of 5 m s^{-1} (Fig. A5b). Remarkably, winds blowing from all directions other than North-East and East-North-East (about 68%, Fig. A5a) are very weak, as they exhibit mean values of 1 m s^{-1} or even lower (Fig. A5b). This results in a very low overall wind speed mean value (1.28 m s^{-1}).

3.1.3. Hazards and socioeconomic vulnerability

UHTI and air temperature were found to be positively correlated each other and with DI (Fig. 16b,d), and negatively correlated with I (Fig. 19a,c). Pearson's correlation coefficients confirmed this relationship (Table A6), with significant values for both DI ($R_{UHTI,\ DI}=0.96$, $R_{AirT,\ DI}=0.84$) and I ($R_{UHTI,\ I}= -0.94$, $R_{AirT,\ I}= -0.88$). As income increases from lower (I≤5) to higher deciles (I≥8), air temperature varies from 27.9 °C to 27.5 °C and UHTI from 0.75 to 0.68. PM_{10} and $PM_{2.5}$ concentrations did not show a linear correlation with either DI (Fig. 19f, h) or I (Fig. 19e, g). Pearson's correlation coefficients confirmed such result, with values that were not significant for both DI ($R_{PM10,\ DI} = -0.25$, $R_{PM2.5,\ DI} = -0.15$) and I ($R_{PM10,\ I} = 0.21$ and $R_{PM2.5,\ I} = 0.16$, Table A6). Conversely, inversely U-shaped relations were found for PM concentrations. The lowest and highest income classes experienced lower PM concentrations compared to middle-income classes. For PM10, the 7th

and 8th income deciles, with DI= –0.04 for the 7th and DI= –1.18 for the 8th, reported a value of 25.5 μg m^{-3} and 25.8 μg m^{-3}, respectively, while the lowest (DI=2.80) and the highest (DI= –1.94) deciles reported a value of 22.8 μg m^{-3} and 22.3 μg m^{-3}, respectively. The highest $PM_{2.5}$ concentrations were associated with the 8th decile (18.13 μg m^{-3}), whilst the lowest and the highest income deciles showed a value of 15.4 μg m^{-3} and 14.6 μg m^{-3}, respectively.

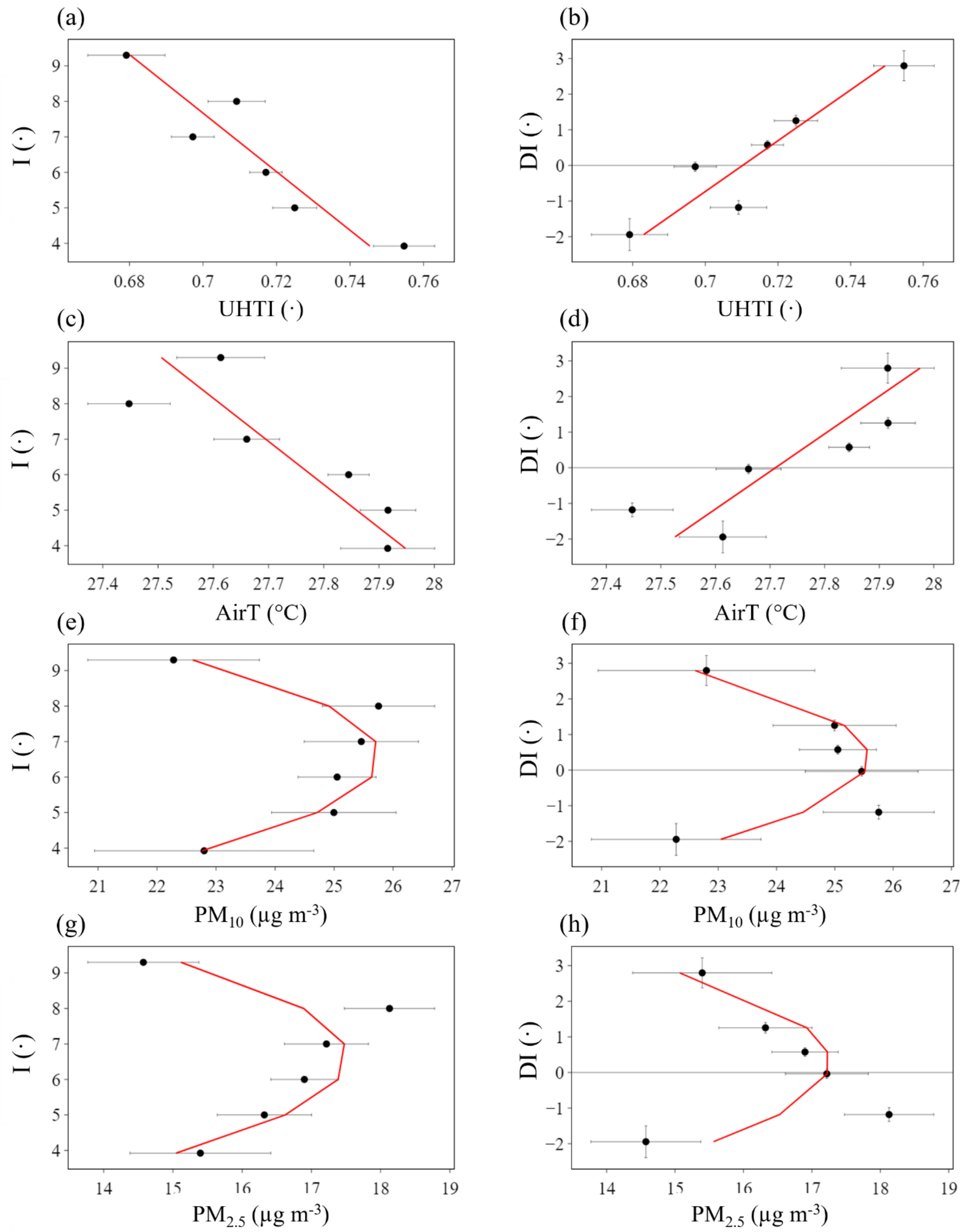

Figure 19. Relation between hazards (UHTI, AirT, PM concentrations) and vulnerability (DI, I) variables averaged for income deciles grouped in classes of similar size. Red lines and curves were estimated through simple and second-degree polynomial regression models. Error bars represent standard error.

3.1.4. PCA

The PCA analysis was performed by processing data of all seven variables, generating new uncorrelated data (Fig. 20).

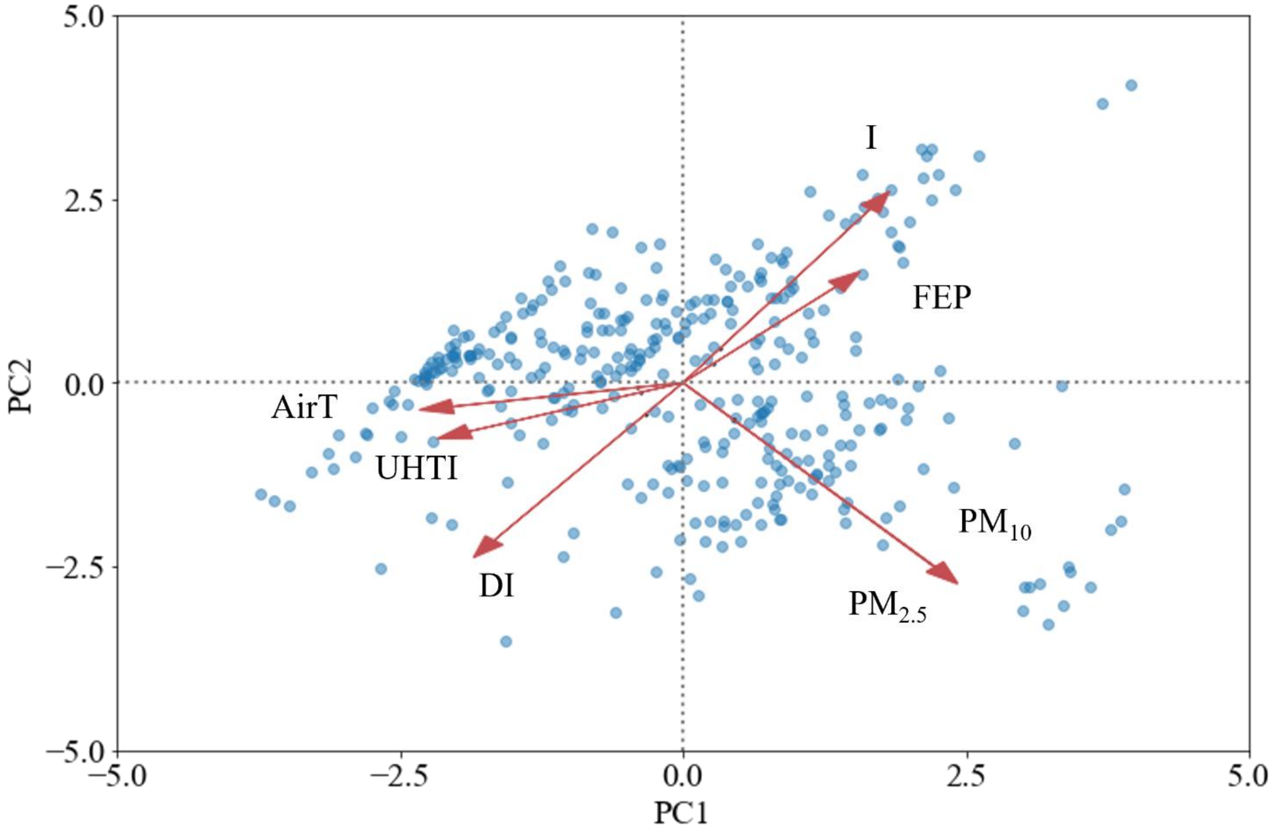

Figure 20. Scatterplots of the principal components data (PC1 and PC2). Red arrows represent the loadings vectors (see Table 4) of each variable. For figure readability red arrows were multiplied by a constant factor (k=5).

Within the PCA preliminary tests (Table 3), the Bartlett's sphericity test rejected the null hypothesis that the correlation matrix (Table A7) was equal to the identity matrix (*p-value* ≈ 0). The KMO test produced a result of approximately 0.57, indicating that the sample was eligible for PCA (Keiser, 1974). The first two eigenvalues were selected since *Lpct* were greater than 1 ($Lpct_1$ = 3.1, $Lpct_2$ = 1.8), and the first two associated PCs explained more than half the variance of the dataset used (59.9%). Finally, the highest positive loadings of PC1 were those of PM concentrations ($l_{1, PM10}$ =0.45, $l_{1, PM2.5}$ = 0.45), while the highest negative loadings were those of air temperature (–0.41) and

UHTI (–0.38), indicating that these two hazards had opposite correlation with PC1. Socioeconomic variables showed positive loadings for income and elderly people ratio, while negative for deprivation index ($l_{1,I}$ = 0.33, $l_{1,FEP}$ = 0.27, $l_{1,DI}$ = –0.33). This revealed a positive correlation between PC1 and wealthy areas, with low levels of material deprivation, a high fraction of elderly residents and high PM concentrations. For PC2, the variables with the highest positive loading were income (0.47) and FEP (0.26), while the variables with the highest negative loading were PM concentrations and DI ($l_{2,PM10}$ = –0.50, $l_{2,PM2.5}$ = –0.50, $l_{2,DI}$ = –0.43). Summer heat intensity showed negative values although the absolute values were smaller than those of PM concentrations ($l_{2,AirT}$= –0.07 and $l_{2,UHTI}$ = –0.13). Thus, high positive values of this component mainly refer to census tracts with low PM concentrations and a high fraction of elderly residents.

Description	Tests		
Pre-PCA test	Bartlett's test	121.3	
	(*p-value*)	(4.1e^{-16})	
	KMO	0.57	
	Parameters	PC1	PC2
Eigenvalues	λ	5.8	3.2
	[*Lpct; Upct*]	[3.1; 6.3]	[1.8; 3.4]
	Explained Variance (%)	34.5	25.4
	Cumulative explained variance (%)	34.5	59.9
Loadings	l_{PM10}	0.45	–0.50
	$l_{PM2.5}$	0.45	–0.50
	l_{AirT}	–0.41	–0.07
	l_{UHTI}	–0.38	–0.13
	l_{I}	0.33	0.47
	l_{DI}	–0.33	–0.43
	l_{FEP}	0.27	0.26

Table 3. Results of tests run before PCA, eigenvalues and corresponding loadings for the principal components (PC1 and PC2).

3.2 Urban Heat spatial modelling

3.2.1 Gap-filling performance

The model exhibited excellent predictive performance for air temperature across all monitoring stations, with R2 values consistently above 0.98 and RMSE values below 1.1 °C (Fig. 21). In particular, the highest agreement between observed and modelled temperatures was found at the Braga site (ID=, R2 = 0.995, RMSE = 0.59 °C), while the Calice station (ID=24) showed the largest residual variability (R2 = 0.987, RMSE = 1.02 °C). Overall, the strong coefficients of determination ($0.986 \leq R^2 \leq 0.996$, Table B1) and low errors ($0.59 \leq$ RMSE ≤ 1.02 °C, Table B1) confirm the robustness and reliability of the model in reproducing air temperature dynamics across the Prato urban network.

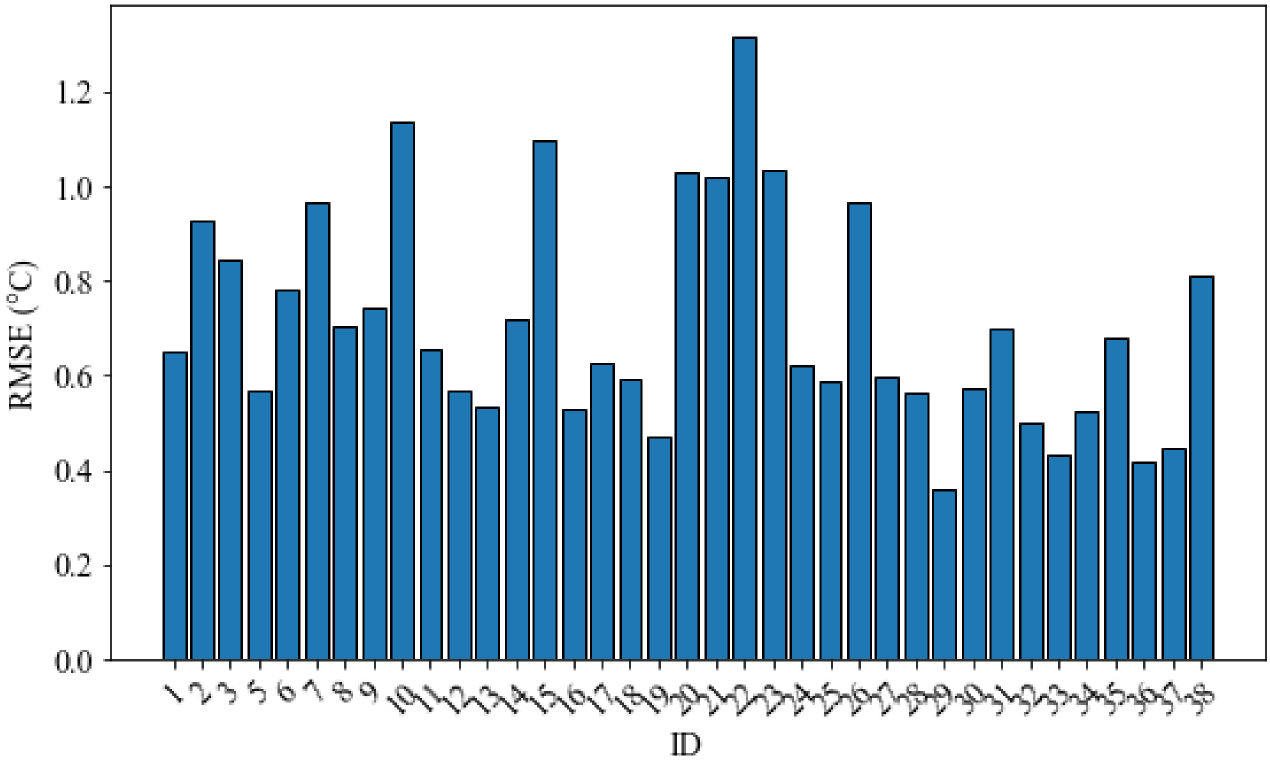

Figure 21. Gap-filling RMSE for each ID station site.

The resulting gap-filled mean air temperatures of the central hours of the 16th July 2024 are reported in Figure 22 and Table B2. The station showing the higher temperatures are mainly located in the downtown and in built-up peri-urban areas. Specifically, the Campolmi (ID=25), ESTRA (ID=5) and Cava (ID=3) sites registered an average of 35.93°C, 35.81°C and 35.56°C, respectively. On the other hand, the lowest temperatures were observed by the stations in the proximity of the river Bisenzio and in a peri-urban site. Specifically, Marradi (ID=10), Capponi (ID=27), Stazione (ID=41), Università (ID=23), San Marco (ID=20) and Calice (ID=24) showed average temperatures of 33.87°C, 33.97°C, 33.57°C, 33.53°C, 33.19°C and 32.97°C, respectively.

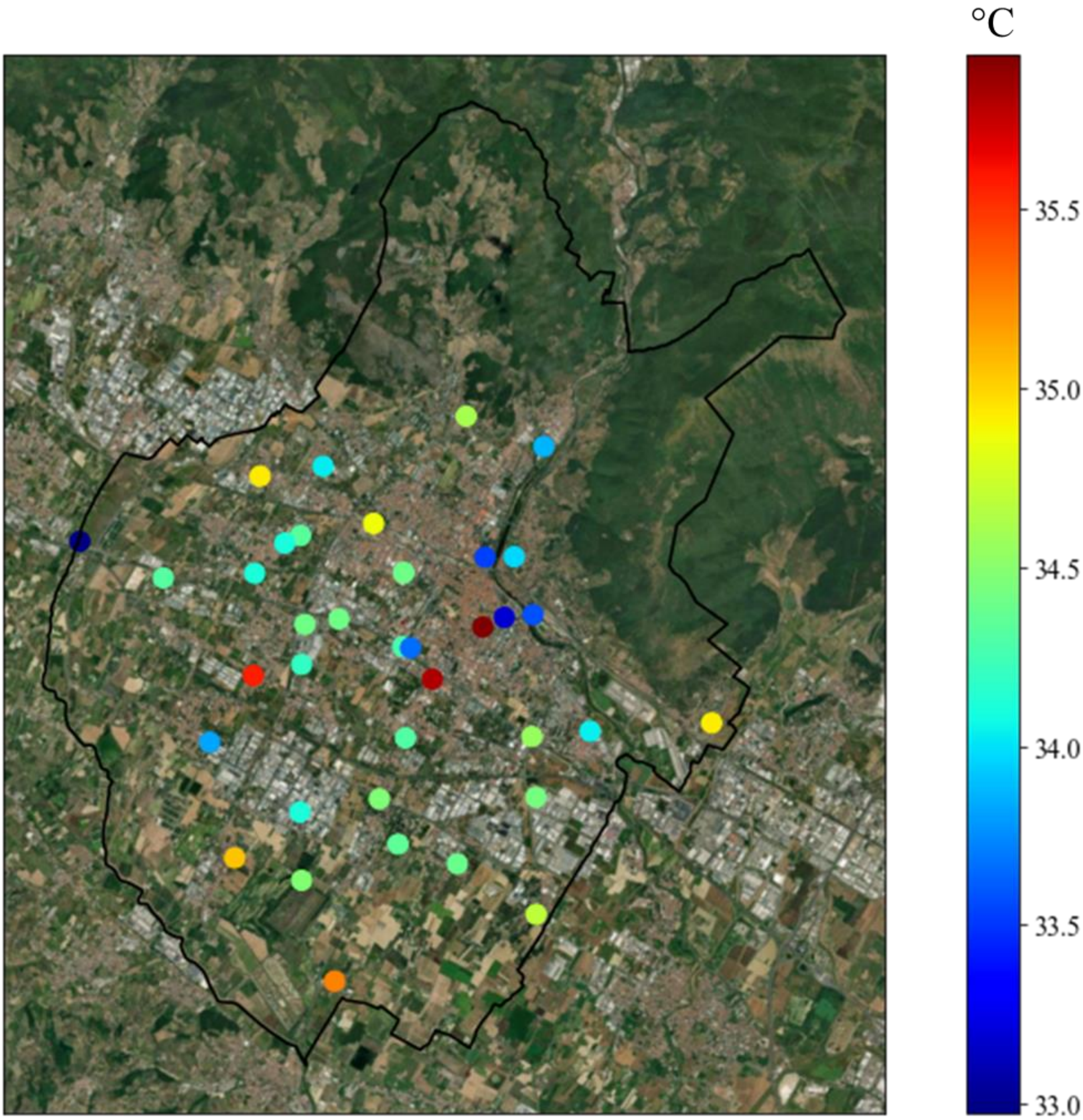

Figure 22. Average AirT between 12:00 and 16:00 observed the 16th July 2024.

3.2.2 Air temperature modelling

The relationships between near-surface air temperature (AirT) and the three predictor variables used in the modelling framework — Sky View Factor (SVF), Vegetation Fraction Cover (VFC), and

Land Surface Temperature (LST) — were firstly evaluated through simple linear regression analyses (Fig. 23). Air temperature exhibited a significant negative correlation with SVF ($R2 = 0.21$, $p = 0.007$) and a weaker, marginally significant inverse relationship with VFC ($R2 = 0.11$, $p = 0.056$). These results indicate that areas characterized by denser vegetation or lower sky openness tend to experience cooler near-surface air conditions. Conversely, a positive and statistically significant correlation was found between LST and AirT ($R2 = 0.18$, $p = 0.014$), confirming the strong thermal coupling between land surface temperature and the air layer immediately above it.

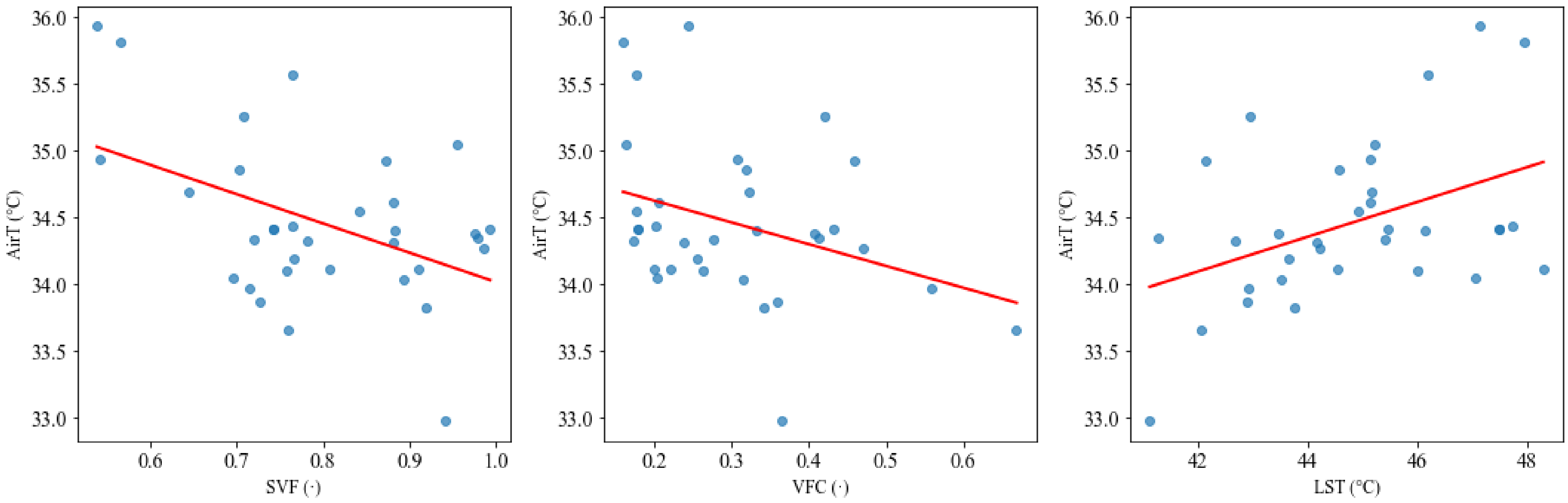

Figure 23. Scatterplots of SVF (a), VFC (b) and LST (c) versus AirT

The multiple linear regression model exhibited an improved goodness of fit (R2 = 0.30) compared to the individual simple regressions. It effectively reproduced the spatial variability of the observed air temperature patterns, although moderate deviations were observed at the lower and upper extremes of the temperature range (Fig. 24). The overall model error was 0.51 °C, while the cross-validated RMSE showed a slight increase (RMSE-CV = 0.56 °C). When compared with other time intervals of the day (Table B3), the model performance was slightly lower in terms of R2 than those obtained for 00:00–06:00 (R2 = 0.38, RMSE = 0.58, RMSE-CV = 0.66) and 17:00–23:00 (R2 = 0.36, RMSE = 0.43, RMSE-CV = 0.48), but higher than that achieved for 07:00–11:00 (R2 = 0.11, RMSE = 0.49, RMSE-CV = 0.58).

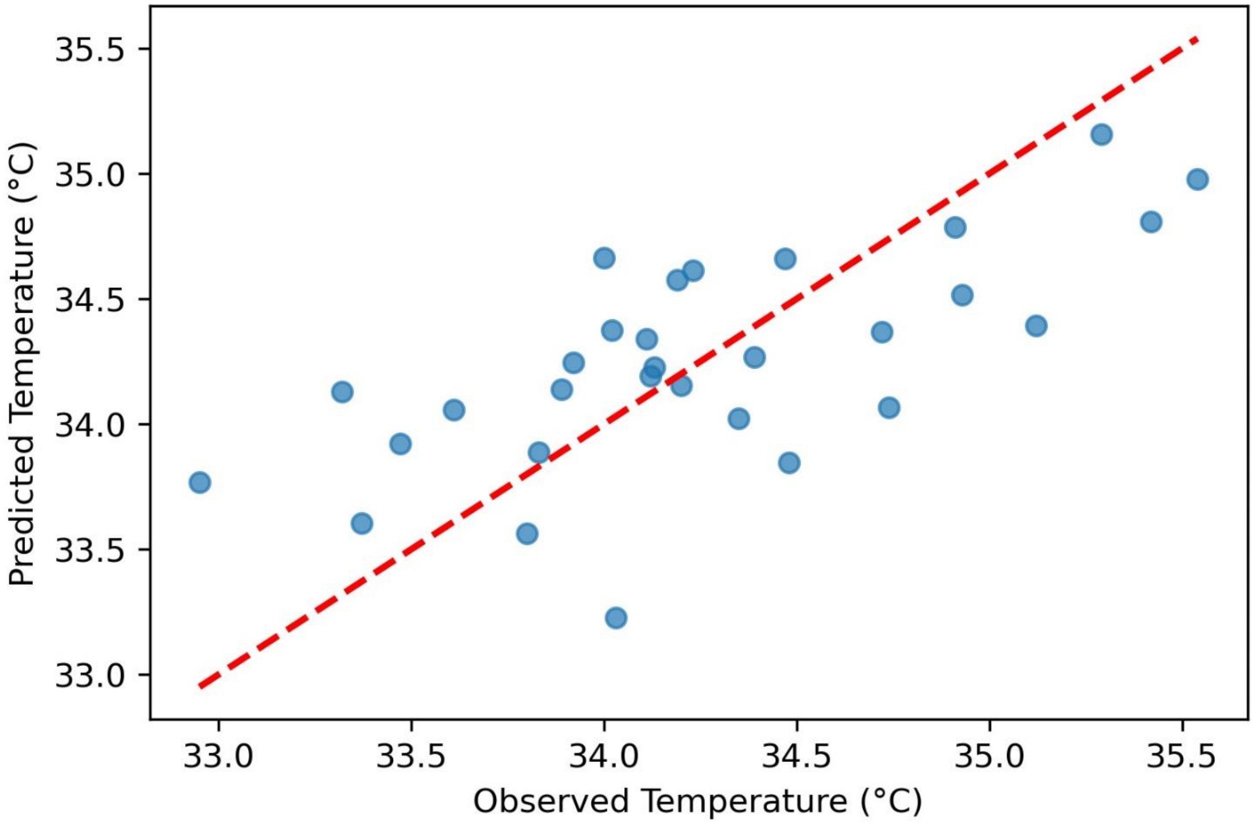

Figure 24. Scatterplot between observed and multiple linear regression modelled air temperature values.

The coefficients derived from the regression model were applied to generate a spatially continuous map of near-surface air temperature at a 10 m resolution across the entire urban domain (Fig. 25), yielding an average city-wide value of 34.2±0.50 °C. As expected, this value was higher than the averages observed during other time intervals of the same day (Fig. B1). The highest temperature values (max = 36.28 °C) were concentrated within the central and southern sectors of the municipality, corresponding to densely built-up areas dominated by impervious surfaces, limited vegetation, and elevated anthropogenic heat emissions. Conversely, lower temperature values (min = 32.92 °C) were primarily observed along the peripheral and peri-urban zones, where vegetation cover, open spaces, and agricultural land contribute to enhanced evaporative cooling and thermal regulation.

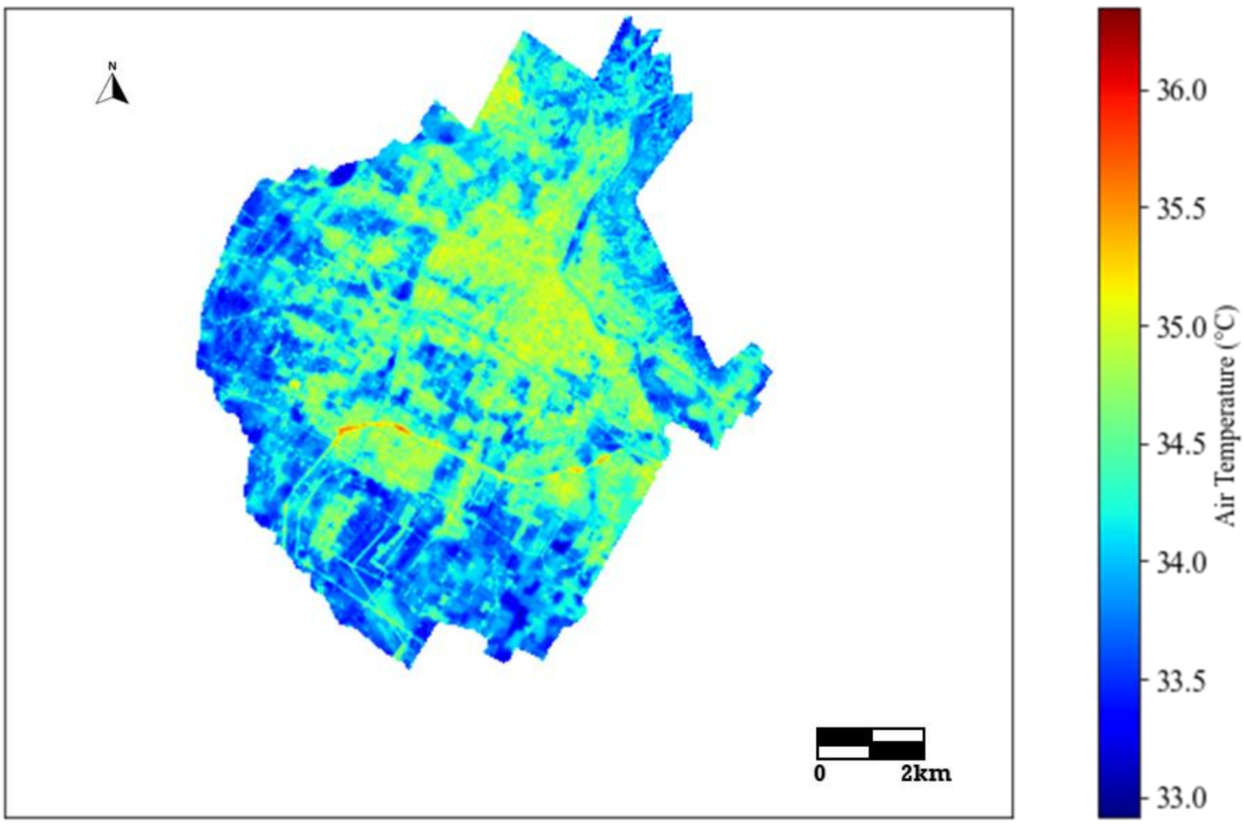

Figure 25. Spatial distribution of modelled air temperature across Prato.

3.2.3 Comparative analysis of UHTI and modelled air-temperature

UHTI and the predicted air temperature were found to be positively with each other. The Pearson correlation coefficient (R = 0.34, p<0.001) indicated a moderate linear association between the two variables, suggesting that areas characterized by higher heat intensity levels also tend to exhibit warmer near-surface temperature. The Bivariate Moran's further, computed on pixel-based values aggregated at 100m resolution, confirmed a strong and statistically significant spatial autocorrelation (I-Moran = 0.43, p < 0.001), implying that the spatial distribution of UHTI and air temperature was not random but spatially clustered. Specifically, zones with high air temperature values were spatially associated with neighboring areas of elevated UHTI, whereas areas with low temperature values coincided with lower UHTI (Fig. 26).

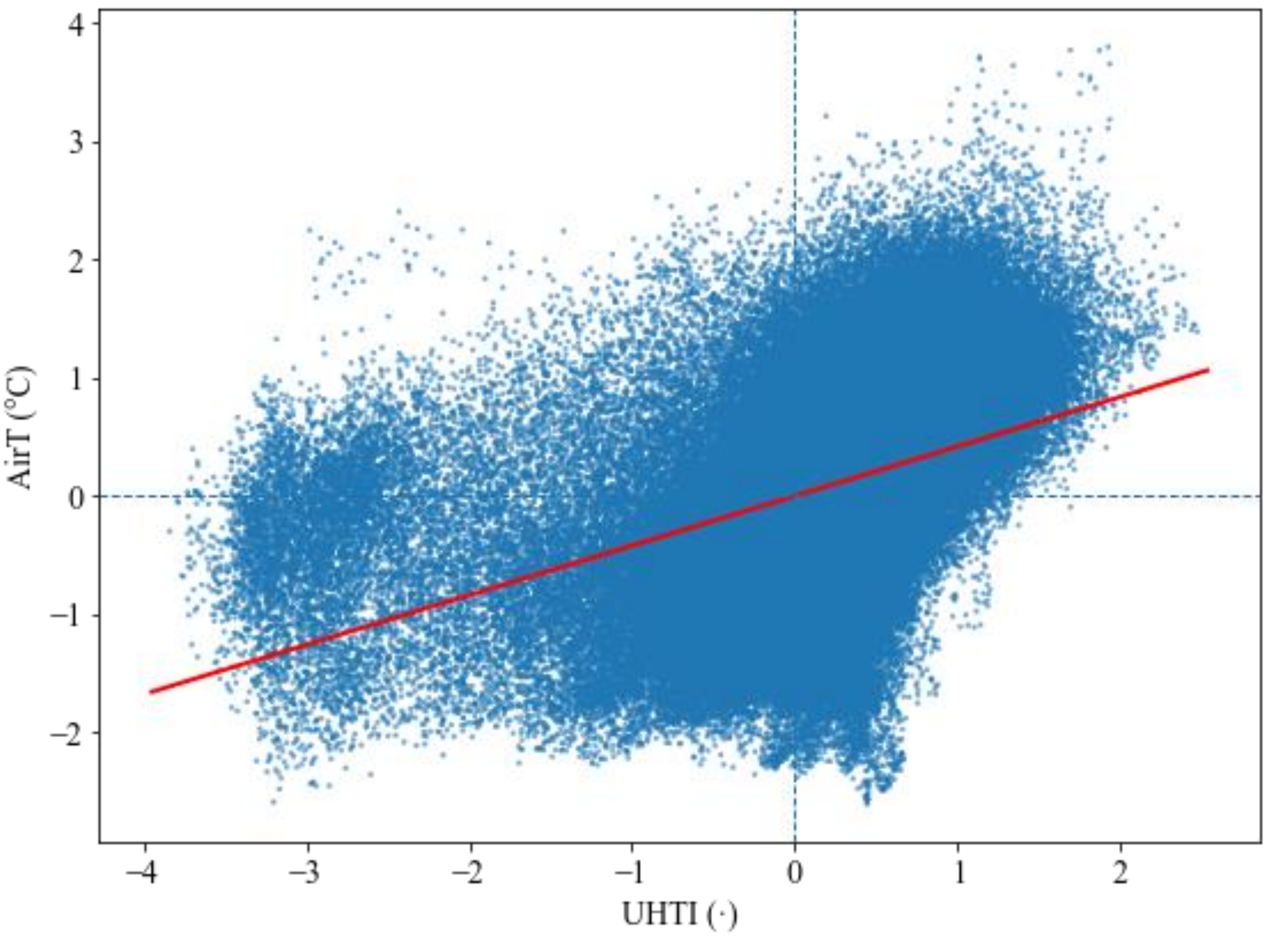

Figure 26. Bivariate Moran's plot of UHTI and modelled AirT.

The Local Indicator of Spatial Association (LISA) analysis revealed a significant spatial association between the predicted air temperature and the UHTI across the study domain, with 59.2 % of all observations showing significant local autocorrelation ($p < 0.05$). High–High (HH) clusters, corresponding to areas where high UHTI values coincided with neighborhoods characterized by elevated air temperature, accounted for 25.9 % of the total domain and were mainly concentrated in the central and densely built-up sectors. Low–Low (LL) clusters, denoting low UHTI values surrounded by cooler temperature, represented 18.7 % of the area and were primarily located in peripheral and vegetated zones. Altogether, HH and LL clusters (44.6 %) confirm a strong spatial coherence between UHTI and the surrounding air temperature. Conversely, the Low–High (LH, 3.7 %) and High–Low (HL, 10.7 %) clusters were less frequent (Fig. 27).

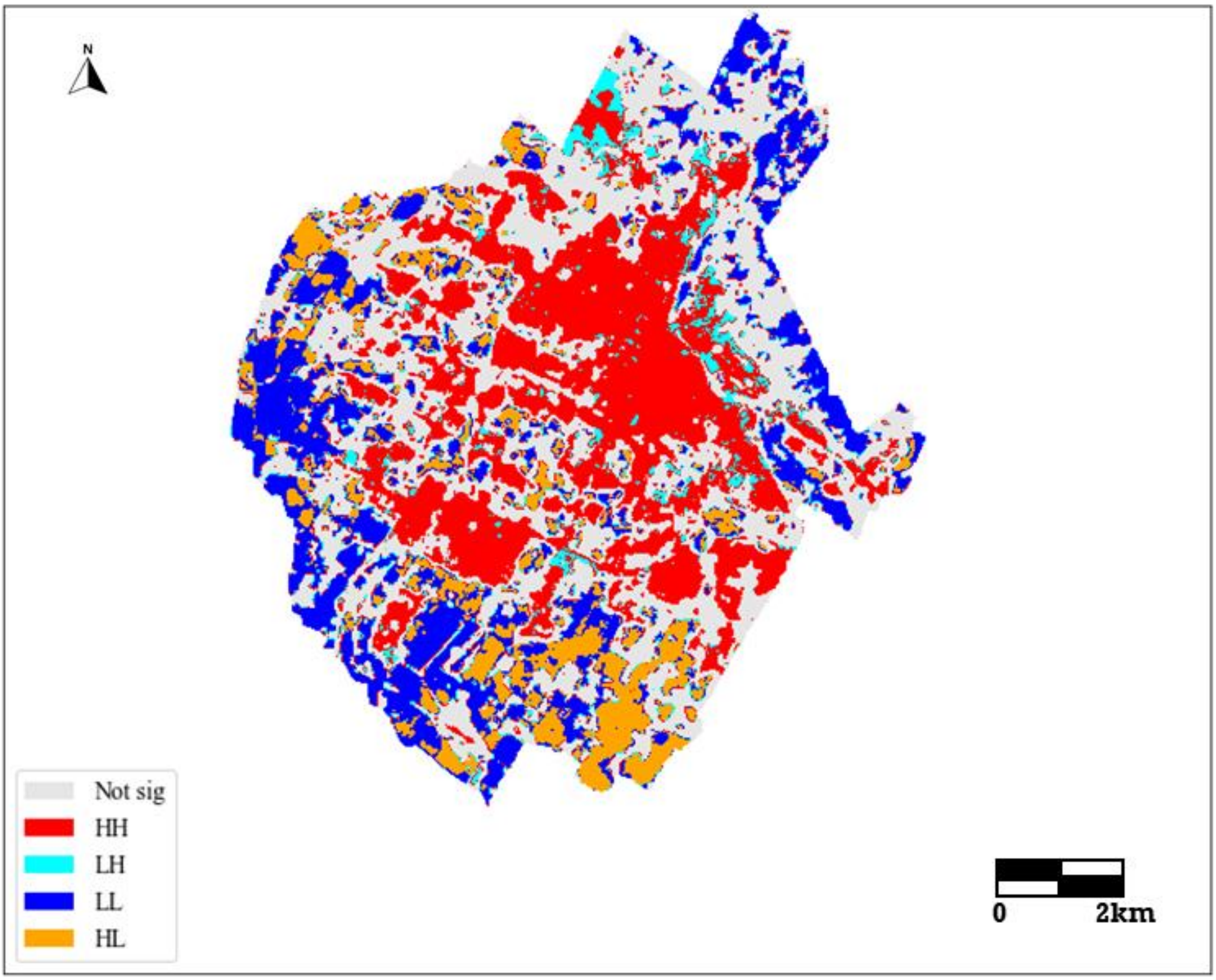

Figure 27. Bivariate LISA map of modelled AirT and UHTI.

3.3 Urban Irrigation

3.3.1 ENVI-met model performance

Model validation demonstrated overall good performance in reproducing AirT and RH at both validation sites (Fig. 28). At the irrigated site (Site A), air temperature dynamics well captured the diurnal dynamics, slightly overestimating early morning and evening hours, resulting in a RMSE of 2.05 °C and coefficient of determination (R2) of 0.98 (Fig. C4). Similarly, RH dynamis were well captured, with a slight underestimation during early morning and evening periods, resulting in RMSE of 9.99% (Fig. C4) and R2= 0.96. Validation at the rainfed site yielded results broadly consistent with those obtained for the irrigated site, with AirT and RH simulations more closely matching observations (RMSE= 1.53 °C and 5.37%; R2 = 0.99 and 0.93).

In the irrigated site, the tuning of soil properties exhibited a substantial enhancement compared to the default soil setting, with SWC simulated values more closely matching both the observed magnitude and pattern (Fig. 28). This resulted in a marked reduction in RMSE from 0.07 $m^3\ m^{-3}$ to 0.01 $m^3\ m^{-3}$ and an increase in R2 from 0.52 to 0.60 (Fig. C4). When the tuned parametrization was applied at the rainfed site, the R2 did not improve while RMSE decreased from 0.06 $m^3\ m^{-3}$ to 0.01 $m^3\ m^{-3}$ (Fig. C4).

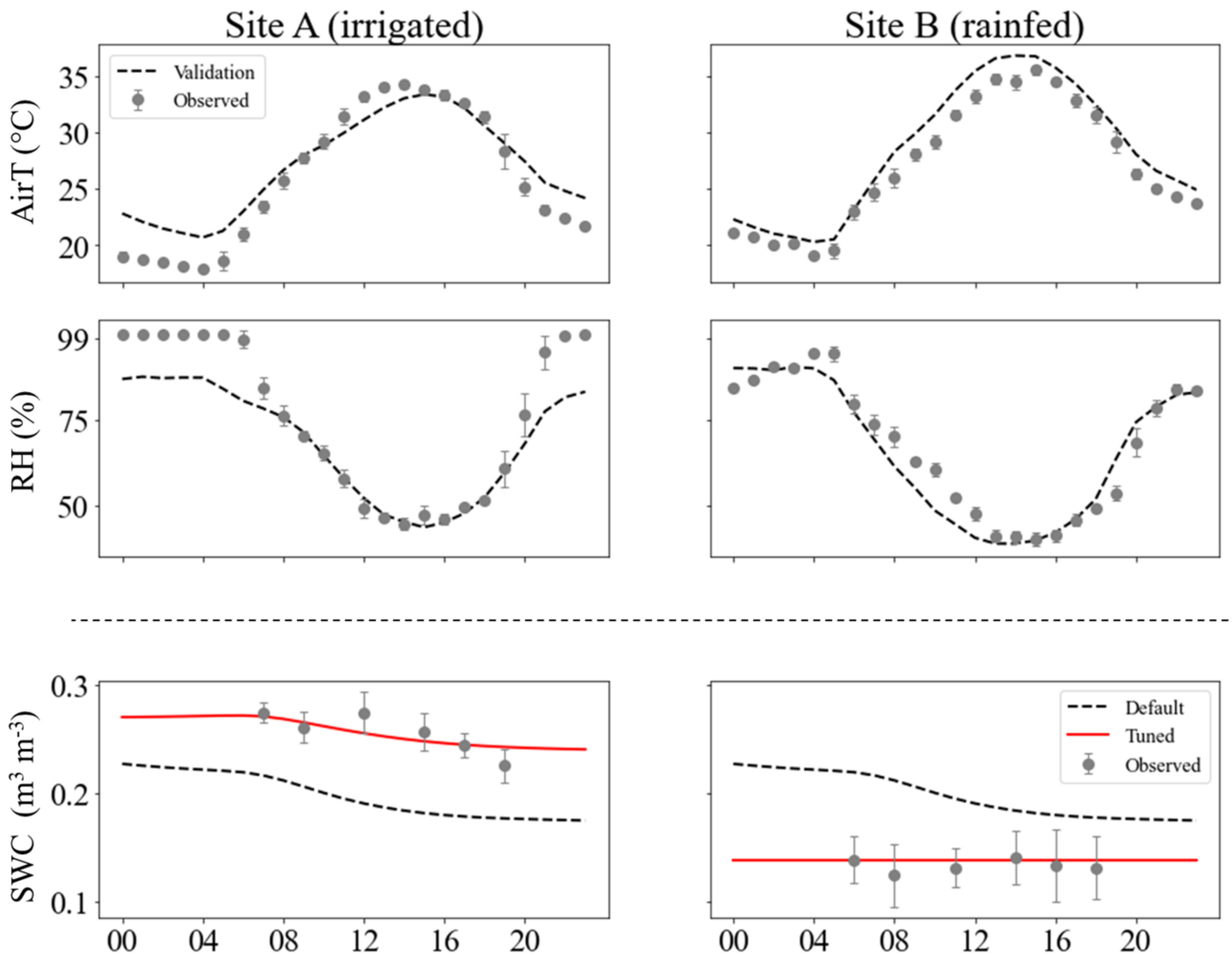

Figure 28. Validation of the ENVI-met model for irrigated and rainfed sites against observations (grey filled dots). Simulated values obtained with default soil properties are shown as a black dotted line; error bars represent the corresponding standard deviation. Simulated SWC dynamics are also reported for default (black dotted line) and calibrated/tuned (red line) soil properties against observations (grey filled dots).

3.3.2 Effect of irrigation on AirT, RH and SWC

The diurnal courses of AirT, RH and SWC were reported as the hourly difference (Δ) between each of the four irrigation scenarios (AS1–AS4) and the corresponding baseline across all tree-density and microclimate classes (Fig. 29). Concerning AirT, in both microclimate classes the irrigation-induced cooling exhibited negligible effects during nighttime and early morning hours, while a pronounced temperature reduction was observed during the central part of the day, with ΔAirT ranging from −1.2 to −2.0 °C under AS4. Across all tree-density classes, the magnitude of cooling

(ΔAirT) increased progressively from AS1 to AS4. Conversely, as tree-density increased, the average daily cooling across all irrigation scenarios (AS1 to AS4) decreased in both microclimate classes, with CL4 showing lower values (−0.45 and −0.39 °C) compared to those found in CL1 (−0.53 and −0.51 °C), for NR and IC, respectively. Concerning RH, in both microclimate classes the irrigation provided an increase in ΔRH during the central part of the day. The maximum ΔRH was achieved under AS4, ranging from +4.8 to +8.5 % considering all classes. Across all tree-density classes, the ΔRH increased progressively from AS1 to AS4. As tree-density increased, the response of ΔRH across all irrigation scenarios tended to be stable or slightly decreased, with CL4 generally showing a lower increase in ΔRH (+2 and +1.6 %) compared to that observed in CL1 (+2.4 and +2.2 %), for NR and IC, respectively. The daily course of ΔSWC showed a relatively smooth diurnal pattern, with limited short-term variability compared to atmospheric variables. Across both microclimate classes, ΔSWC increases monotonically from AS1 to AS4, typically range from approximately +0.08 to +0.12 $m^3 m^{-3}$ under AS1 and increase to about +0.14 to +0.18 $m^3 m^{-3}$ under AS4, depending on tree-density. A slight daytime decrease was observed around midday (≈12:00–15:00), followed by a gradual recovery during the late afternoon and evening. The influence of tree-density on ΔSWC was comparatively weaker than that observed for ΔAirT and ΔRH, with differences among CL1–CL4 that remain modest across both microclimate classes.

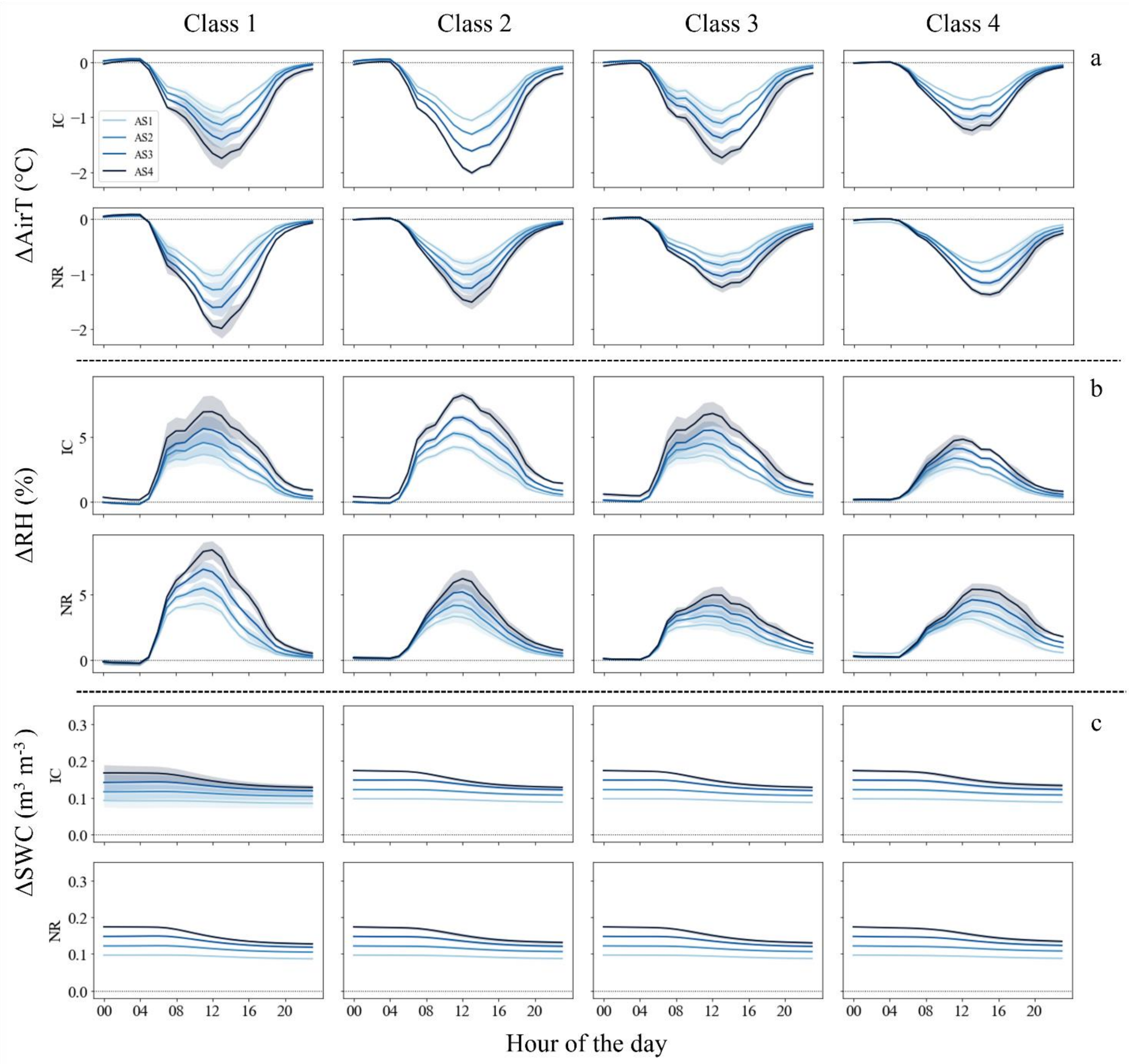

Figure 29. Average diurnal differences in AirT (a), RH (b), and SWC (c) between the baseline and the four irrigation scenarios (AS1–AS4), simulated across four tree-density classes (CL1–CL4) for the urban park domains located in the inner-city (IC) and near-river (NR) classes. Shaded areas indicate confidence intervals arising from the spatial aggregation of the simulated domain and reflect sub-grid spatial variability.

3.3.3 Assessment of thermal mitigation potential

The average air temperature (°C) during the warmest hours of the day (12:00-16:00) and the corresponding temperature classes, were summarized using heatmaps. Results revealed clear and consistent thermal patterns driven by increasing tree-density and irrigation intensity across both microclimate classes. Air temperature systematically decreased from CL1 to CL4, with an average reduction between the lowest (CL1) and highest (CL4) tree-density classes of ~1.5 and ~0.5 °C for NR and IC classes, respectively. Similarly, irrigation intensity increases from baseline to AS4 led to a closer decrease of average air temperature for both microclimate classes, slightly higher for IC (~1.6°C) than for NR (~1.4°C). The combined effect of increasing both tree-density and irrigation intensity resulted in a pronounced shift toward cooler air temperature classes, with mean values transitioning from highest (> 35.0 °C) to lowest (< 34.0°C) classes in both microclimate classes, with absolute temperatures slightly higher in the IC class across all scenarios.

Air temperature(°C) (12:00-16:00)

	Near-river						Inner-city					
Class	BS	AS1	AS2	AS3	AS4	AVG.	BS	AS1	AS2	AS3	AS4	AVG.
CL1	35.64	34.85	34.61	34.27	33.89	***34.65***	35.73	34.95	34.73	34.46	34.13	***34.80***
CL2	34.89	34.19	34.02	33.80	33.58	***34.10***	35.57	34.64	34.39	34.07	33.70	***34.47***
CL3	34.51	33.89	33.74	33.55	33.36	***33.81***	35.33	34.56	34.34	34.08	33.73	***34.41***
CL4	33.97	33.24	33.08	32.88	32.69	***33.17***	35.02	34.39	34.23	34.05	33.87	***34.31***
AVG.	***34.75***	***34.04***	***33.86***	***33.63***	***33.38***		***35.41***	***34.64***	***34.42***	***34.17***	***33.86***	

Air T. classes (scale 1-8)

	Near-river						Inner-city					
Class	BS	AS1	AS2	AS3	AS4	AVG.	BS	AS1	AS2	AS3	AS4	AVG.
CL1	8	6	6	5	4	***5.8***	8	6	6	5	5	***6.0***
CL2	6	5	5	4	4	***4.8***	8	6	5	5	4	***5.6***
CL3	6	4	4	4	3	***4.2***	7	6	5	5	4	***5.4***
CL4	4	3	3	2	2	***2.8***	7	5	5	5	4	***5.2***
AVG.	***6.0***	***4.5***	***4.5***	***3.8***	***3.3***		***7.5***	***5.8***	***5.3***	***5.0***	***4.25***	

Air T. classes (0.50°C)		
Initial	Final	Value
35.51	36.00	8
35.01	35.50	7
34.51	35.00	6
34.01	34.50	5
33.51	34.00	4
33.01	33.50	3
32.51	33.00	2
32.01	32.50	1

Figure 30. Heatmaps of average air temperature (°C) and corresponding temperature classes (0.5 °C bins) simulated for near-river (NR, left) and inner-city (IC, right) urban park microclimate classes under baseline (BS) and four irrigation scenarios (AS1–AS4), across four tree-density classes (CL1–CL4). Values represent mean conditions during the time-window (12:00–16:00), averaged across the eight urban park domains. Cooler colors indicate lower air temperatures. Row and column averages summarize the combined effects of tree-density and irrigation intensity on thermal conditions.

Concerning the incremental cooling contribution of tree-density (Fig. 31), the resulting patterns are comparable between the two microclimate classes, although consistently lower in magnitude for the IC class. Specifically, higher cooling efficiency occurs both at intermediate (0.62 °C and 0.30°C) and high (0.63 °C and 0.16°C) canopy densities for NR and IC, respectively (Fig. 31a). However, whilst a bimodal response where both the initial establishment of tree cover and the transition to fully covered conditions are particularly effective is observed at NR (Fig. 31b), IC reports a higher efficiency during the initial establishment of tree cover (55%) followed by diminishing marginal returns with additional canopy cover (Fig. 31c).

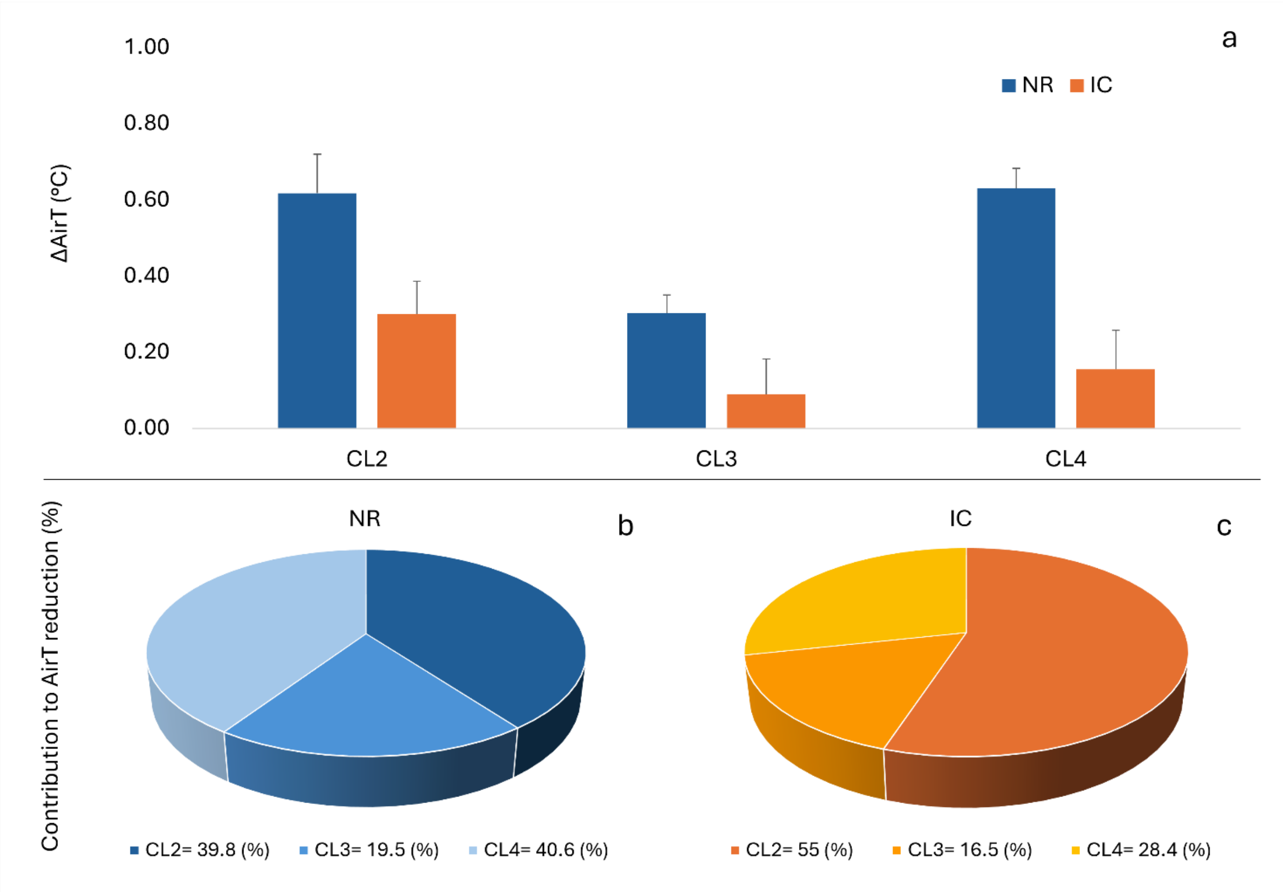

Figure 31. Incremental contribution of tree-density to air-temperature mitigation in near-river (NR) and inner-city (IC) microclimatic class. Upper panel (a) shows the incremental air-temperature reduction (ΔAirT, °C) associated with increasing tree-density classes (CL2–CL4) for NR (blue bars) and IC (orange bars); error bars indicate variability across aggregated domains. Lower panels

illustrate the relative contribution (%) of each tree-density class to the total cooling effect within NR (b) and IC (c) microclimate classes.

When analyzing the effect of irrigation intensity, the incremental cooling patterns and their magnitude are highly comparable between the two microclimate classes, characterized by a strongest cooling response at the first irrigation step followed by diminishing marginal returns with irrigation intensity increase (Fig. 32). The transition from BS to AS1 produces the largest temperature reduction in both NR (0.71°C) and IC (0.78 °C). The following increments are consistent but about three times lower in magnitude, included in a range of 0.18–0.25 °C and IC of 0.21–0.31 °C across AS2–AS4 for NR and IC respectively (Fig. 32a). Globally, AS1 accounts for approximately half of the total irrigation-induced cooling in NR (51.7%) and IC (50%), whilst the remaining scenarios account for 13-20% each (Fig. 32b,c).

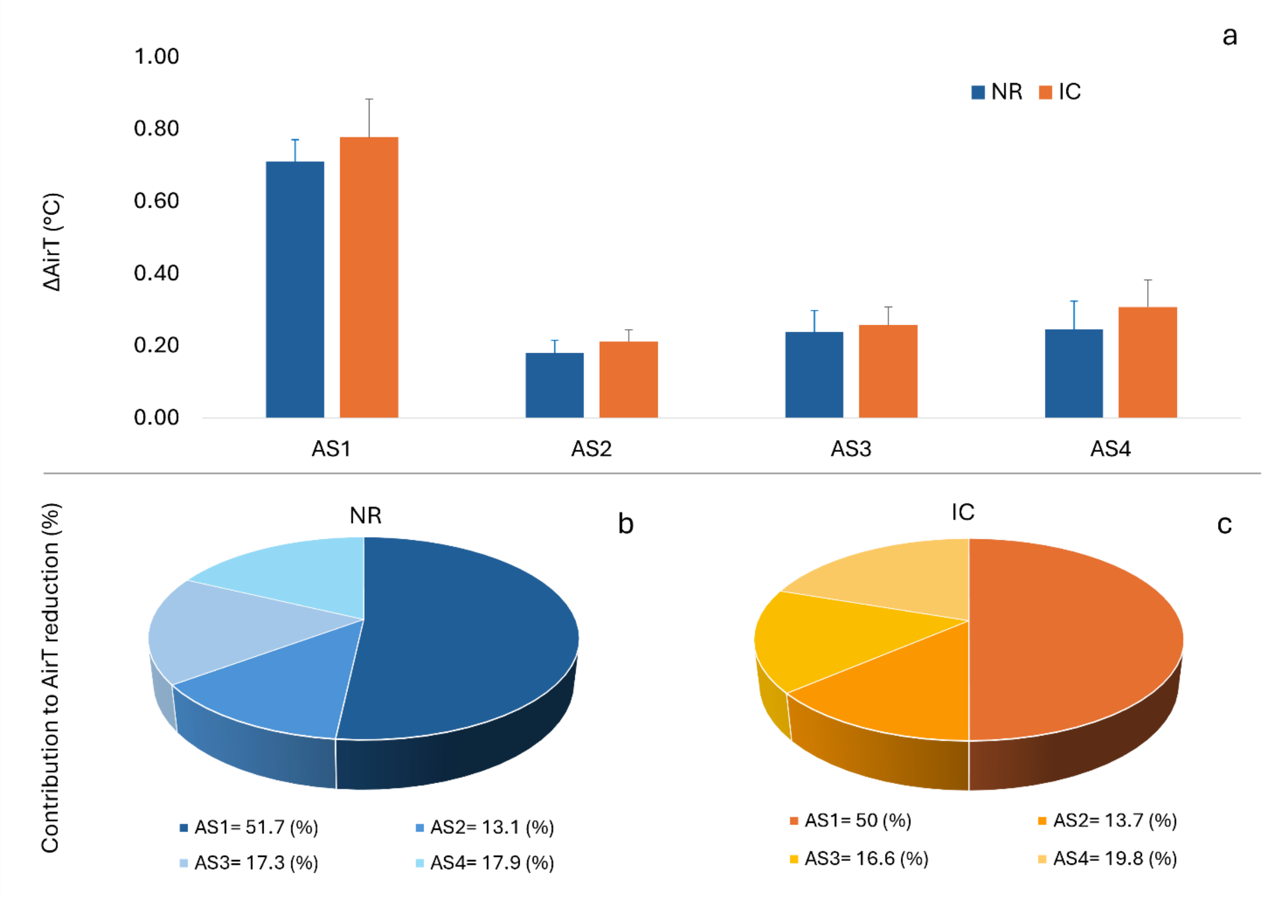

Figure 32. Incremental contribution of irrigation intensity to air-temperature mitigation in near-river (NR) and inner-city (IC) microclimatic classes. Upper panel (a) shows the incremental air-temperature reduction (ΔAirT, °C) associated with increasing irrigation intensity (AS1–AS4) for NR (blue bars) and IC (orange bars); error bars indicate variability across aggregated domains. Lower panels illustrate the relative contribution (%) of each irrigation scenario to the total cooling effect within NR (b) and IC (c) microclimate classes.

3.3.4 Economic analysis of irrigation scenarios

The economic analysis was performed combining the response of total irrigation costs with air temperature reduction (ΔAirT), and normalized cooling efficiency (°C €$^{-1}$, 0–1) for combined microclimatic classes scenarios (IC–NR), with values averaged across tree cover density classes (Fig. 33).

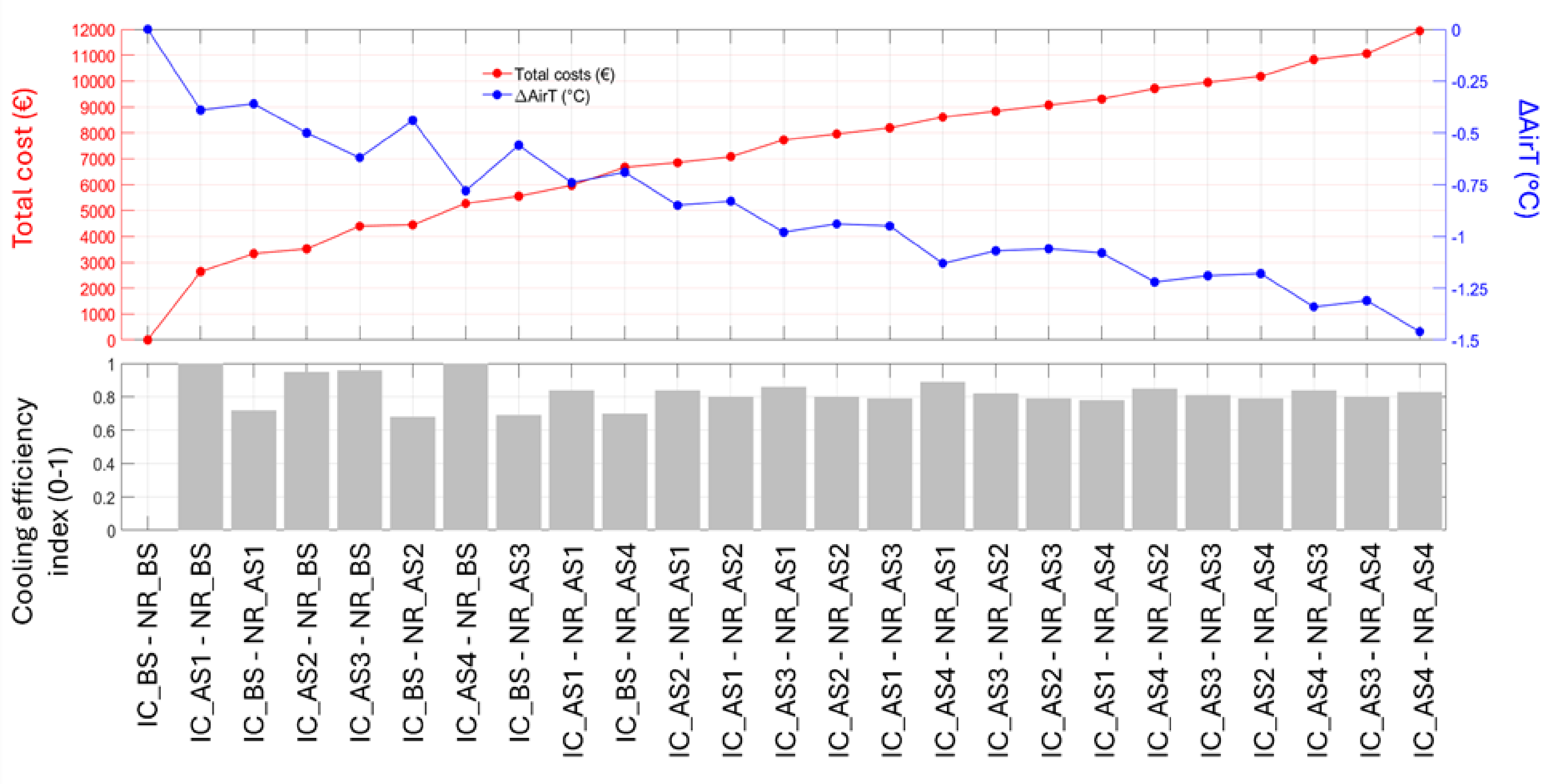

Figure 33. Joint economic–thermal response of irrigation strategies aggregated at climate classes. The figure shows the relationship between total daily irrigation costs (€, red line, left y-axis), air temperature reduction (ΔAirT, °C; blue line, right y-axis), and normalized cooling efficiency (°C €$^{-1}$, scaled 0–1; grey bars) for combined inner-city and near-river microclimate classes scenarios (IC–NR), with values averaged across tree-density classes.

The analysis suggested that total costs can vary from 0 € (no irrigation intervention) up to a maximum of approximately 11940 € d^{-1} for the most intensive irrigation combination (IC_AS4–NR_AS4). The related air temperature reduction response showed a non-linear but consistent response to increasing costs. From the analysis emerged that low-irrigation scenarios, which include at least one baseline (i.e., no irrigation) in one of the two microclimate classes (e.g., IC_AS1–NR_BS and IC_AS2–NR_BS) already produce measurable cooling effects (−0.39 to −0.50 °C) at total costs between 2600 and 3500 € d^{-1}. Cooling values exceeding −0.75 °C are systematically observed once total costs reach 5000–5500 € d^{-1}, while for achieving air temperature reductions greater than −1.0 °C occur beyond approximately 7500–8000 € d^{-1}. The maximum cooling effect (−1.46 °C) is achieved only under the highest-cost configuration. The normalized cooling efficiency (°C €$^{-1}$, scaled between 0 and 1) exhibits a clear peak under low-to-moderate irrigation intensities, with maximum normalized efficiency values (0.95–1.00) observed under scenarios involving baseline conditions (i.e., IC_AS1–NR_BS, IC_AS2–NR_BS, and IC_AS4–NR_BS) which provide total costs below 5300 € d^{-1} and ΔAirT between −0.39 and −0.78 °C. At higher cost (> 8,000 € d^{-1}), normalized efficiency stabilizes around 0.78–0.85.

4 Discussion

4.1 Assessment of risk components

The development of a risk assessment framework for the city of Prato by combining information on concurrent hazards (i.e., heat stress and air pollution), socioeconomic vulnerabilities and demographic exposure (i.e., elderly population), merging multiple data sources, allowed to draw a comprehensive and insightful picture of the inter-relations between socioeconomic and environmental factors. The first outcome indicated that socioeconomic vulnerability was positively and linearly correlated with summer heat intensity (Fig. 19a,b,c,d). The regression analysis showed that an increase in air temperature of about 0.1 °C was associated with an Income decrease of ≈1 decile and a Deprivation Index increase of 0.76 (Table A6). Similarly, as UHTI increased by approximatively 0.01 on a scale of 0.68 to 0.75 (+14.3%), income decreased by about 1 decile and deprivation index increased by 0.62 (Table A6). These findings suggest that both economic and social inequalities can be exacerbated by the intraurban heat distribution during the summer season, raising the issue of environmental injustice. Specifically, environmental injustice in urban areas of the developed countries often occurs when the lower-income communities cannot access to beneficial ecosystem services provided by urban greening (i.e., gardens, parks and agronomic cultivations). Vegetation can modify local microclimate by transpiration and evaporative cooling, improve air quality through pollutant absorption, and results in increased mental benefits (Tyrväinen et al., 2014; Sæbø et al., 2017; Rahman et al., 2020). The lack of these services for the lower-income communities can increase inequalities with respect to the higher-income communities, resulting in increased health and mental risks and related health-costs for municipalities. In Prato, the most socially vulnerable population was found downtown, which is characterized by fewer green spaces, high-density buildings and roads with impermeable surfaces and heat-release materials compared to the surrounding areas. The latter, by contrast, particularly the hilly areas, show higher income and lower social deprivation, and are characterized by higher greening and lower building and population density.

This outcome is in line with studies carried out in other cities worldwide. Chen et al. (2022) explored the spatial correlation between heat intensity and heat vulnerability in Taipei (Taiwan), finding that the most vulnerable districts, characterized by a high density of artificially built areas and low-income and socially vulnerable groups, lived in the center of the metropolitan area. Hulley et al. (2019), using a heat vulnerability index integrating socioeconomic conditions of residents with heat intensity, observed that Los Angeles (US) downtown areas were characterized by high heat intensity and presence of low-income communities. Assessing the relationship between income and heat intensity distribution for 25 cities around the world, Chakraborty et al. (2019) found that the majority of the city centers were characterized by low-income communities and higher temperatures. For the city of Turin (Italy), Ellena et al. (2023) showed that the urban development during the 20th century influenced the current heat intensity patterns, which was higher in the downtown compared to the suburban areas due to the presence of buildings characterized by heat-releasing materials, fewer green spaces, and higher levels of socioeconomic deprivation. A similar pattern was also reported in Padua (Italy) by Pappalardo et al. (2023): analyzing heat-related risks using a climate justice approach including low-income residents, they observed that central areas were characterized by both high heat intensity and most low-income residents.

The current urban structure of several European cities such as Prato, Turin and Padua originate from the past urban development. The central areas of these cities, initially surrounded by medieval defensive walls, were densely built and populated, whilst the suburban areas were mainly characterized by natural or agricultural systems. Later, with city expansion, suburban areas were slowly incorporated in the main urban settlement. Then, in the 1950s’ and 1960s’, at the start of the industrialization process, rural population migrated to urban areas, further increasing population density within urban agglomerations (Accetturo and Mocetti, 2019) and making modern suburban areas usually less densely populated and greener. A similar urban development was also observed by Depietri et al. (2013) in Cologne (Germany), where current wealthier residents are located in the greener areas surrounding the center whilst the high heat intensity is found in downtown. In support of this evidence, a recent analysis on 14 major European cities from Rocha et al. (2024) showed that low-income residents mainly live in areas with less green space, thus being more exposed to heat stress. This pattern can also be extended to the non-European cities mentioned above, such as Taipei (Chen et al. 2022) and Los Angeles (Hulley et al. 2019), where heat stress and socioeconomic vulnerability have shown similar correlations, although historical and geographical differences make direct comparison with European cities difficult. By contrast, a different pattern was found in large cities such as Rome and Paris. In Rome, analyzing the relation between environmental and social vulnerability, Badaloni et al. (2023) found that the higher heat intensity was associated with lower socioeconomic deprivation in the city center. In Paris, Forceville et al. (2024) did not find a clear relation between higher temperatures and higher social deprivation levels. Compared to Prato, these opposite results may be explained by the large and rapid urban expansion experienced by Rome and Paris, which led to patchy urban growth where high building density and poor vegetation were not systematically associated with social deprivation. Concerning air quality, the relationship between environmental hazards and socioeconomic conditions has been much less explored in the literature, as urban air quality data monitored by reference stations are too coarse and dense networks rarely exist or perform for short campaigns only (Carotenuto et al., 2023). The sensor network deployed in Prato allowed to perform a spatially-resolved analysis that suggested an inverse U-shaped non-linear relation between socioeconomic vulnerability and air pollution (Fig. 19e,f,g,h). This relation indicates that middle-income classes are exposed to the highest PM concentrations. This result is in line with other studies carried out worldwide at different spatial scales, from cities to country level. At country level, Niu et. al. (2024), investigating the main drivers of PM10 and PM2.5 concentrations in 2273 cities in China, found an inverse U-shaped relation between economic development and air pollution levels. Across Europe, Gosztonyi et al. (2023) investigated the relationship between PM2.5 concentrations and income in Helsinki (Finland), observing that median income classes experienced the highest PM2.5 concentrations. Havard et al. (2009) analyzed the association between traffic-related air pollution and a deprivation index computed from data of 190 census blocks (spatial unit equivalent to the Italian census tracts) in Strasburg (France). They found that middle levels of socioeconomic deprivation were associated with the highest air pollution levels. In Italy, a nonlinear relation was observed by Conte Keivabu (2023), who correlated the socioeconomic status of 23,000 Italian districts with PM2.5 concentrations, and by Germani et al. (2014). The latter assessed the relation between income and industrial air pollutant emissions to determine whether socioeconomic and demographic characteristics could explain the pollutant emissions due to industrial activities in several Italian provinces. The inverse U-shape observed here appears to reflect the Environmental Kutznez Curve (EKC) theory, which states that environmental degradation increases up to a maximum level as income increases and then reverts when such maximum is reached (Grossman and Krueger, 1995). The pattern can be explained by the fact that middle-income communities are mostly working-class, living and working in areas characterized by intensive emissions from road transport, industries, and by high demographic and building density. On the other hand, high-income classes either carry out economic activities with low environmental burden or simply live in areas with a lower number of pollutant-emitting activities. Finally, low-income communities may have low productivity and be located in areas that are degraded but where pollutant emissions are likely lower. Such conditions can be observed in Prato, where the most polluting activities are found in middle-income areas, located in some central and south-western peri-urban areas. By contrast, highest-income districts (I≥9 and DI≤–1.90) are located in hilly areas, characterized by a lower number of economic activities and, in turn, fewer emission sources, while lowest-income and most socially deprived districts (I≤4 and DI≥2.80) are few in numbers and likely associated with reduced emissions. This pattern reflects the industrialization history of Prato and likely of many other European cities, that experienced a strong industrial development between the 19th and 20th centuries, which stands to nowadays. In this period, several textile activities grew up patchworked within the city of Prato, often seamlessly with residential houses.

The heterogeneous relationship within the risk component analysis including vulnerability, exposure, and hazards was properly described by the PCA analysis (Fig. 20). PC1 was found to be positively associated with FEP, I, PM10 and PM2.5, thus high values of PC1 can be interpreted as a condition of lower levels of socioeconomic vulnerability and a high fraction of elderly residents exposed only to winter air pollution hazard and not to summer heat. PC2 was found to be positively associated with FEP and I, thus high values of PC2 can be interpreted as a condition of lower levels of socioeconomic vulnerability and a high fraction of elderly residents that are not exposed to both winter and summer hazards. Therefore, PC1 and PC2 likely refer to a wealthy FEP associated with low socioeconomic vulnerability for which summer heat generally has low intensity, while winter air pollution has both high and low intensity. This outcome leads to two important considerations. First, it suggests that most of the elderly people live in peri-urban cooler districts and are part of medium-to-high income households with low social deprivation. Such privileged average condition likely improves the capacity to access to adaptation measures that improves their capability to cope with hazards. This condition plays a crucial role in the overall risk assessment for the exposed population since adaptation measures can be associated with a reduction of vulnerability and thus to lower heat-related and air pollution related mortality and morbidity. Specifically, socioeconomic status can have a protective effect against heat stress, since high socioeconomic status individuals can afford expensive houses minimizing heat-transfer also located in vegetated districts, air conditioning systems, high-quality health care, and are more likely to have high-level education and thus healthy lifestyles (Yardley et al., 2011). These adaptation measures could also make these individuals more protected from poor air quality, although they were found more exposed to PM than to heat and, therefore, these adaptation measures may be less effective.

Second, elderly people living in peri-urban and greener districts where heat is less intense can be exposed, however, to elevated winter PM concentrations, and thus may experience high air pollution risks. This condition was observed in the south-western part of Prato, specifically for ID 03 and 08 (Fig. 17,18), where medium-low air temperature was associated with higher PM concentrations and middle levels of income and deprivation index (Fig. 15). The higher PM concentrations recorded in these less densely populated and greener area may be due not only to the significant presence of various highly-emitting pollution sources such as highly travelled roadways or commercial and industrial activities, but also to the recurrence of very weak winds along these directions (Fig. A5b), proving unable to develop an advection strong enough to prevent the stagnation of pollutants emitted from those sources.

The presence of multiple emission sources associated with high population density concentrated in the middle class, requires first to design and implement decarbonization mitigation policies aimed at decreasing both greenhouse gas and pollutant emissions at the same time. On the other hand, urban regenerative policies based on greening can be optimally designed and placed, providing both a relevant cooling ecosystem service coupled to a moderate service for pollution abatement.

4.2 Spatialization of air temperatures

The AirQino low-cost stations network deployed in Prato allowed to spatially model near surface temperature. Firstly, an initial gap-filling procedure based on K-Nearest Neighbor Estimation criterion was performed to maximize the number of ground-based observations. Following the approach adopted by Nardino et al. (2022) and Fiorillo et al. (2023), the ground-based air temperature observations were then integrated to remote sensing inputs to predict air-temperature city-wide at fine-scale resolution, providing a tool that could be employed by the local municipality to detect air temperature hazard hot-spot.

The modelling approach used to spatialize summer heat was multiple linear regression (MLR), which has been widely employed in previous studies to spatialize near-surface air temperature (AirT) (Wang et al., 2017; Alonso et Renard, 2019; Jain et al., 2022; Barthwal et al., 2022; Chen et al., 2025). MLR is a supervised statistical learning technique that models the linear relationship between a dependent variable and multiple predictors. In spatial prediction studies, MLR is often used as a baseline model to benchmark the performance of more complex machine learning algorithms. However, such models are generally less interpretable, require larger datasets to ensure robustness, and may be more prone to overfitting when applied to limited sample sizes (Zhu et al., 2023). In this study, the number of observations available for model training was relatively small (n = 39), and cross-validation results indicated limited predictive performance for more complex models (Table B4). Under these conditions, multiple linear regression (MLR) provided a suitable trade-off between predictive accuracy and interpretability, while also allowing for more direct comparison with the UHTI.

Alternative approaches for spatializing AirT include stochastic geostatistical methods, such as kriging and regression kriging, which rely on the spatial autocorrelation structure inferred from point observations to provide best linear unbiased predictions at unmonitored locations (Rakowska et al., 2024; Holobaca et al., 2025). These methods are particularly effective when combining deterministic relationships with environmental predictors and stochastic modelling of residual spatial variability, as in the case of regression kriging. This approach enables the simultaneous representation of large-scale trends driven by explanatory variables and local heterogeneities captured through spatial dependence (Li et Heap, 2008). However, the effectiveness of geostatistical methods strongly depends on the presence of significant spatial autocorrelation in the data. In this study, the diurnal variability of the spatial autocorrelation structure of AirT during summer 2024 was evaluated using variogram parameters (sill, nugget, and range) and Moran's I. Results indicated generally weak spatial autocorrelation over the average diurnal cycle (Figure B2, B3), thus limiting the applicability and expected performance of geostatistical approaches.

The predictive performance of the MLR (R2 = 0.30, RMSE = 0.51 °C, RMSE-CV=0.56 °C) indicated the challenges associated with modelling near-surface air temperature at high spatial resolution across large and heterogeneous urban areas during the warmest hours of the day. Specifically, this could be explained by the complex interplay of surface heterogeneity, anthropogenic heat emissions, and non-linear atmospheric turbulence that generates pronounced spatial variability of local microclimates that is difficult to capture with linear predictors (Buyantuyev et al., 2010). Similar limitations have been reported in previous studies. Venter et al. (2020) applied a Random Forest regression model over Oslo integrating crowdsourced air temperature data with remote sensing inputs for 2018, and achieved an average RMSE of 1.85 °C when mapping daily maximum air temperature, a value which is way lower compared to average (RMSE=0.51°C) and minimum daily temperature (RMSE=1.46°C). Gkirmpas et al. (2025) modelled street-level air temperatures in

Thessaloniki using random forest regression during a July 2021 heatwave using low-cost sensors and a set of environmental predictors, finding good nighttime accuracy but inconsistent daytime patterns due to model's limited ability to capture fine-scale microclimatic variability.

The comparative analysis between the UHTI and the modelled air temperature revealed a notable spatial correlation between the two approaches used to map urban heat (R = 0.34, I-Moran = 0.41). LISA cluster analysis showed that urbanized areas in the city center were consistently characterized by both high air temperature and high UHTI values (HH), whereas most rural and peri-urban zones exhibited low temperature–low UHTI associations (LL). These spatial agreements, which accounted for 44.6% of all identified clusters, align with widely documented findings in urban heat modelling literature, which consistently demonstrate that impervious and densely built-up surfaces are associated with elevated thermal conditions, while vegetated and green areas typically remain cooler (Oke, 1982; Buyantuyev et al., 2009). Furthermore, the HH clusters overlapped with areas characterized by higher poverty and social deprivation levels, reinforcing the strong link between environmental hazards and socioeconomic vulnerability, as detailed in the risk component analysis. Conversely, mismatched clusters - namely high UHTI but low air temperature (HL) and vice versa (LH) - were sparsely distributed, predominantly in rural and peri-urban fringes. In the southern part of the study area, a relevant HL cluster was identified in a predominantly agricultural zone, characterized by extensive crop fields and sporadic built-up areas. Such discrepancies can likely be attributed to differing sensitivities of the explanatory variables (VFC, SVF, and LST) to the response variable (air temperature) within the two modeling frameworks. For example, SVF exhibits a positive contribution in the formulation of the UHTI (Eq. 3), whereas it is associated with a negative coefficient in the MLR model (Table B3). This difference suggests that, within the UHTI formulation, lower SVF values act as a proxy for increased shading and therefore reduced air temperature, whereas in the MLR framework a lower SVF may instead reflect enhanced radiative trapping and reduced longwave heat loss, leading to higher near-surface air temperatures, particularly under low-ventilation conditions that are common during heatwave conditions. Overall, these contrasting results highlight the inherent difficulty of fully capturing the complexity of urban thermal environments and disentangling the relative contributions of the factors that shape fine-scale spatial temperature patterns.

4.3 Urban heat mitigation

4.3.1 Model performances and thermal mitigation effect

In this part of the thesis, the ENVI-met model reproduced irrigation by prescribing increased initial SWC in the upper soil layer (0–20 cm), set above the permanent wilting point, thus using SWC enhancement as a proxy for irrigation practices. This approach has previously been adopted in an ENVI-met-based study by Gobatti et al. (2025), which evaluated three irrigation conditions (dry non-irrigated and field capacity states) by varying soil moisture between the permanent wilting point and field capacity within a simplified urban environment, to assess how irrigated urban green spaces can influence human thermal comfort across three Local Climate Zones in Switzerland. Despite to our knowledge no other studies involving ENVI-met model to simulate irrigation effect were found, the use of SWC variation as a proxy for irrigation is consistent with several modelling studies employing different modelling frameworks. For instance, Sorooshian et al. (2011) implemented a dynamic irrigation scheme within the mesoscale MM5 atmospheric model, whereby soil water content was restored to field capacity whenever it dropped below crop-specific depletion thresholds. Similarly, Li et al. (2023a) applied an irrigation parameterization within the CLM4.5 land surface model to replenish soil moisture toward a dynamic target threshold when water availability limited photosynthesis. Gao et al. (2020) coupled the WRF model with an Urban Canopy Scheme and simulated irrigation of vegetated surfaces by increasing soil water content in the upper soil layers to a prescribed value (0.33). Heusinger et al. (2018) adopted a comparable strategy in the EnergyPlus simulation framework by prescribing volumetric water content in the soil substrate to represent non-irrigated, sustainable, and unrestricted irrigation scenarios.

The increase in SWC as a proxy for irrigation led to a reduction in near-surface air temperature relative to the corresponding baseline across all tree-density classes, with average cooling ranging from 1.15 to 1.87 °C and maximum reductions reaching up to 2.5°C in the strongest irrigation scenario (Fig. C5, C6). These values are consistent with findings reported in other modelling studies investigating irrigation-induced thermal mitigation. For instance, Sorooshian et al. (2011) reported irrigation-driven changes in air temperature in California, with daily mean reductions below 1 °C and maximum reductions reaching up to 4 °C in adjacent non-irrigated areas. Li et al. (2023a) estimated annual mean reductions in maximum surface temperature ranging from −0.6 °C to −1.2 °C in strongly irrigated regions across China, together with smaller but systematic decreases in minimum temperatures (−0.2 to −0.6 °C) relative to non-irrigated conditions. Furthermore, Asmus et al. (2023) showed that across Mediterranean regions, irrigation during heatwave conditions can induce mean air temperature reductions of up to 4.5 °C, accompanied by increases in relative humidity of up to 20%. Similarly, Gao et al. (2024) reported that irrigated green infrastructure in desert environments can reduce summer mean air temperature by approximately 2–3 °C, while wintertime impacts remain below 0.5 °C. Overall, these findings support the robustness of the modelling outcomes and corroborate the effectiveness of representing irrigation-induced cooling through soil moisture enhancement across different modelling frameworks and climatic contexts.

The concomitant decrease in near-surface AirT and increase in RH observed in the diurnal cycles during the warmest hours of the day (Fig. 29) reflect a shift in surface energy partitioning. Under irrigated conditions, higher soil water availability promotes the conversion of a larger fraction of available energy into latent heat flux (LE) at the expense of sensible heat flux (H) (Lunel et al., 2024; Jiang et al., 2014; Spronken-Smith et al., 2000). Consistently, the simulated daily courses of LE and H (Fig. C7) show a progressive increase in LE accompanied by a corresponding decrease in H as irrigation intensity increased from AS1 to AS4, indicating the ability of the model to well reproduce key physical and physiological processes governing vegetation–atmosphere interactions at high spatial resolution. These changes predominantly occurred during midday, when high solar radiation, air temperature and elevated vapor pressure deficit usually intensify evapotranspiration and vapor diffusion, thereby amplifying the irrigation-induced cooling effect (Cheung et al., 2024; Kool et a., 2014).

While maximum average cooling provided by irrigation scenarios was broadly comparable between the two microclimatic classes (−1.37 °C and −1.56 °C for NR and IC, respectively), the shading effect associated with increased tree cover differed markedly. Specifically, the average maximum air temperature reduction attributable solely to shading was substantially greater in the NR class (−1.48 °C) than in the IC class (−0.49 °C). This suggested that the cooling effectiveness of tree shading is reduced in warmer, more compact urban environments, such as the simulated inner-city green spaces, compared to cooler urban zones. Several factors may explain this behavior. First, the parks simulated within the IC class are characterized by surrounding tightly packed buildings with low inter-building spacing, whereas NR parks, being closer to river corridors, experience a more open urban configuration. These differences in urban morphology likely altered local airflow dynamics, since low inter-building spacing restricts ventilation and reduces the longwave radiative heat loss, thereby limiting warm air dispersion with a consequent reduction in cooling efficiency from vegetation (Li et al., 2024; Han et al., 2023; Morakinyo et al., 2017). Moreover, stomatal regulation governing the ecophysiological responses of simulated urban trees to heat and water stress was parameterized uniformly across microclimatic classes, potentially introducing bias in the estimated cooling effects. This assumption may have exaggerated the physiological stress imposed by high temperatures on parks within the IC class, thereby representing them as less resilient than those in the NR class. Consequently, the simulated differences in cooling effects of urban tree cover between IC and NR conditions may have been partially overestimated relative to real-world observations.

Without specific parameterizations of stomatal behavior for both microclimate classes under contrasting thermal and hydric regimes, the models cannot fully capture the adaptive capacity of vegetation to warmer environments (Chen et al., 2024). As a result, plant functioning is represented as more stressed and less adaptable than in reality, which may lead to an underestimation of transpiration-driven cooling and a bias in the simulated cooling potential across microclimatic contexts.

Moreover, the model may not fully reproduce additional vegetation responses to hot and dry conditions due to simplified details of tree geometries such as canopy size, leaf type and Leaf Area Density (LAD), and radiation interactions such as foliage shortwave transmittance, and foliage shortwave albedo, all of which can influence the accuracy of the model to reproduce even little change in cooling response among different scenarios (Xu et al., 2025; Liu et al., 2018). Another key aspect could be the lack of the model to reproduce the isohydric behavior of some tree species, which can maintain transpiration under declining leaf water potential, thereby maintaining a non-negligible cooling effect even during periods of water stress (Sade et al., 2012; Grote et al., 2016; Pace et al., 2021). In addition, the higher cooling effect observed in NR parks may be further reinforced by local hydrological conditions that are not fully represented in the model. Proximity to river systems can indeed promote shallow groundwater tables and upward capillary fluxes, enabling vegetation to sustain higher transpiration rates and physiological efficiency during heat stress (Li et al. 2023b; Missik et al., 2019; Chen et al., 2016). Overall, these limitations in the representation of vegetation behavior introduce a certain degree of uncertainty in the quantification of cooling due to tree-density classes

Overall, taking into account differences between tree density classes, the maximum near-surface air temperature reduction reached up to 3 °C (AS4-CL4) compared to the baseline scenario (BS-CL1). This result suggests that vegetation alone may not be sufficient to mitigate extreme heat conditions, particularly during the hottest hours of the day. A temperature reduction of about 3 °C represents a substantial cooling effect under extreme summer conditions and can significantly attenuate peak thermal stress during the warmest hours. However, despite this reduction, baseline air temperatures remained sufficiently high that simulated AirT values exceeded 30 °C, highlighting that combined heat mitigation strategies, while effective, may not be sufficient on its own to fully restore optimal thermal comfort conditions ((Gobatti et al., 2025; Olivieri et al., 2024; Salman and Saleem, 2021; Battista et al., 2019). Nevertheless, these findings highlight that the synergistic interaction between tree cover and irrigation constitutes a robust and effective adaptation strategy in warm and dry conditions, particularly for reducing peak air temperatures and moderating heat extremes. Such combined approaches may therefore play a crucial role in urban heat mitigation strategies under future climate scenarios characterized by more frequent and intense heat waves.

4.3.2 Economic analysis

Most of the current literature have predominantly focused on the biophysical cooling effects of irrigation or on broader aspects of urban green infrastructure planning, such as economic evaluations of alternative urban park designs, sustainable management practices for urban green spaces, or assessments of eco-economic benefits related to irrigated urban greening strategies. For instance, Cheung et al. (2024) in a field experiment conducted on turfgrass plots in an urban context in Australia, indicated that that irrigation scheduling plays a decisive role in enhancing the cooling performance of urban green spaces, reporting as multiple daytime irrigations generated significantly stronger afternoon cooling (−0.9 °C) than both single night-time (−0.6 °C) and single daytime irrigation (−0.5 °C). Doll et al., (2024), in a benefit–cost analysis to assess alternative urban park designs that increase drought-tolerant native vegetation to reduce water demand in Perth (Australia), indicated that the most efficient design included approximately 60% native vegetation and 40% watered grass, yielding the highest net benefits for both new ($887000) and retrofitted parks ($64200). Lv et al (2021) reported a cost–benefit assessment for irrigated urban green spaces in Zhengzhou (China, 2018), suggesting as reclaimed water irrigation costs were approximately 46% lower than those of tap water irrigation, with a positive net benefit of $2.00 billion. Arbat et al. (2013) assessed irrigation-related energy consumption and costs for private urban gardens using simplified hydraulic designs in two Spanish cities, reporting mean total irrigation costs of €2974 ha^{-1} yr^{-1} in Girona and €3383 ha^{-1} yr^{-1} in Elche, with energy costs accounting for 11.4% and 23.0% of total costs, respectively. Shurtz et al., (2022) investigated the optimization of urban irrigation by analyzing relationships among water use, irrigated area, satellite-based vegetation index, and water pricing structures in USA, indicating that tiered water rates reduced water use compared to flat rates for comparable plant health, and that plant health exhibits an optimal irrigation threshold beyond which additional watering provides no benefit. However, these approaches have often overlooked the explicit linkage between water-related costs and quantifiable thermal mitigation outcomes.

In this study, explicitly coupling irrigation-related costs with modelled thermal benefits enabled a more realistic evaluation of irrigation as an urban climate adaptation strategy for the city of Prato. This integrated perspective addresses a critical knowledge gap by supporting the identification of cost-efficient nature-based solutions for mitigating heat stress in a typical urban environment.

Considering the wastewater treatment facility of Prato, which has an estimated residual capacity of approximately 6.5 million m^3 yr^{-1} beyond the 3.5 million m^3 currently reused, the development of irrigation strategies for urban green spaces appears feasible without competing with potable water resources for citizens. Under the highest irrigation configuration (AS4) for all of the eight parks included in both IC and NR microclimate classes, the total daily water demand was estimated to be 3326 m^3 d^{-1} (Tab. C5). Assuming an irrigation period of 100 days per year to cover the warmest season, the total annual water requirement for the highest irrigation configuration would amount to approximately 332600 m^3, corresponding to only about 5 % of the secondary treated wastewater annually available. This would suggest that reclaimed wastewater could represent a viable and underutilized resource for irrigating urban green space, thus resulting in a suitable and economic viable heat-mitigation strategy for the Municipality of Prato.

Concerning the thermal reduction, results indicated that a ΔAirT reduction threshold of −0.5 °C on average, is associated with a relatively low daily costs (<5000 € d^{-1}) but a limited number of feasible irrigation scenarios (n = 4). Despite their limited number, these scenarios coincide with the highest normalized cooling efficiency (°C $€^{-1}$) because of the inclusion of at least a no irrigation treatment in one of the microclimate classes. Beyond this threshold, an additional cooling of approximately 0.5 °C on average can be achieved by increasing total daily costs up to a maximum of 8000 € d^{-1}, thereby enabling a further set of ten adaptation strategies. A subsequent incremental cooling of up to 0.5 °C on average requires an increase in daily costs between 8000 and 12000 € d^{-1}, corresponding to an additional ten irrigation strategies. This progressive increase in costs for diminishing incremental cooling gains reflects a pattern of decreasing marginal cost-effectiveness, despite continued absolute reductions in air temperature. The observed decline in normalized efficiency at higher irrigation intensities suggests that intermediate irrigation scenarios may offer the most balanced trade-off between economic investment and thermal mitigation benefits.

The cost–benefit relationships identified in this study should not be interpreted as a universal transferable value, but rather as outcomes strictly representative of this case study. Major limitations concern in the cost analysis presented here does include the lack of capital expenditures associated with the installation of new irrigation infrastructure, such as water conveyance networks, pumping systems, or the construction of irrigation facilities, which could significantly affect the overall economic feasibility. However, the proposed framework can represent an informative decision-support layer that can assist policymakers and urban planners in the strategic design and prioritization of green infrastructure within the Municipality. Such considerations can be fundamental also for enhancing vegetation performance in terms of evaporative cooling and atmospheric CO_2 sequestration. This dual benefit aligns with broader climate-adaptation and mitigation objectives, including the goals of the “100 Climate-Neutral and Smart Cities” initiative, reinforcing the role of urban green spaces as multifunctional assets in future climate-resilient cities.

5 Conclusion

This thesis aimed to build a holistic understanding of two relevant urban hazards in the city of Prato (Italy), with a detailed focus on urban heat, by linking three complementary strands of research. It combined a risk assessment based on fine-scale environmental and socio–economic data, a city-wide modelling of near-surface summer air temperatures using low-cost sensors and remote sensing inputs, and an investigation of irrigation as a possible mitigation strategy for urban parks during heatwaves. Integrating these components allowed the work to address both the drivers of heat exposure and vulnerability and to explore how targeted interventions can modify microclimatic conditions.

5.1 Risk assessment framework

The risk assessment framework developed in the first part of the thesis (Chapter 2), based on the IPCC benchmark, is designed to assess the main environmental issues of a typical mid-sized European city such as Prato (Italy). While relating the effects of climate and human-induced hazards to citizens vulnerability, this approach can be applied to identify possible adaptation measures in urban contexts that are relevant for decision-making processes aimed at fulfilling equality and social justice at both local and national level. The main novelty lies in the use of multiple data sources (air temperature, PM concentrations, UHTI, income, deprivation index and fraction of elderly people) at fine spatial resolution to assess risk components and their relations. The development of a dense network of LC air quality stations, which provided high-frequency data of air pollution and air temperature, allowed a sound characterization of the spreading of heatwaves at fine spatial scale (i.e., neighborhoods). Furthermore, this approach included the use of a thermal index (UHTI) that, to our knowledge, was never applied in other studies to perform a risk components analysis.

The risk assessment framework indicated that socioeconomic vulnerability was positively correlated with summer heat intensity, while it showed an inverse U-shaped relation with winter PM concentrations mainly affecting middle-income classes. Also, socioeconomic vulnerability associated with heat intensity was found to reflect the Italian urbanization history. Finally, elderly people living in peri-urban and greener districts resulted to be exposed to higher winter PM concentrations as well as lower heat intensity due to the heterogeneous emission sources and wind regime affecting the urban area.

Main limitation of the study lies in the urban-scale representativeness of air pollution data. Whilst UHTI index was applied to evaluate the summer heat over the whole city, further corroborating the results found in the correlation analysis, data from LC air quality stations only represented a specific area around each station, thus not covering the whole municipal area. To this aim, a denser network is currently under development in Prato.

As a general guideline for other cities where sensor networks were deployed or are to be installed, they must be dense enough to provide reliable estimates of spatial variability. This type of data-driven approach may be further improved by including high spatial resolution population health data into the framework. Furthermore, local stakeholders, such as policymakers and citizens, could be involved in collecting relevant information on population habits. All these factors could improve quantitative and qualitative relations to support public investments within forthcoming mitigation and adaptation plans. Future research could integrate additional health data and ad-hoc questionnaires into the proposed risk assessment framework to improve its performance.

5.2 Modelling near-surface air temperature

The second component of the thesis investigated how near-surface summer air temperatures can be modelled at fine spatial resolution. A gap-filling procedure using a K-Nearest Neighbors estimator was first applied to maximize the availability of ground observations. These observations were then integrated with remote sensing predictors (SVF, VFC, LST) in a multiple linear regression model to predict air temperatures across the city. The approach demonstrated the feasibility of combining dense LC sensor networks with earth observation data to produce high-resolution temperature maps that can support the risk assessment linked to extreme heat presented in the previous section.

Nevertheless, the predictive performance was modest ($R^2 \approx 0.30$, RMSE ≈ 0.51 °C), reflecting many well-known challenges of modelling near-surface temperatures in complex urban environments. Despite these challenges, the modelled air temperatures correlated spatially with the UHTI. R of 0.34 and a I-Moran of 0.41 indicated a moderate association between the two approaches. LISA outcomes (Fig. 32) revealed that high-temperature/high-UHTI clusters (HH) were located in the urbanized city-center, whereas low-temperature/low-UHTI clusters (LL) occurred in rural and peri-urban areas. Moreover, HH clusters overlapped with neighborhoods displaying higher poverty and social deprivation, underscoring the social dimension of heat exposure identified in the risk assessment.

The main limitation of this study concerned the low-spatial coverage of the LC sensors network necessary to spatially model AirT, also relying on more advanced machine learning techniques. Future analysis could aim at improving urban temperature modelling through both methodological and spatial coverage, further increasing the network or using other data sources. Machine learning techniques (e.g., random forests, gradient boosting) and non-linear predictors may capture microclimatic variation more effectively. Incorporating finer spatial data such as building heights, surface materials, anthropogenic heat sources, and water bodies could also improve predictive skill. Finally, cross-validating model outputs and exploring temporal dynamics would offer a more robust basis for decision-making. These improvements could enable city planners to detect heat hot-spots more accurately and evaluate the efficacy of mitigation interventions.

5.3 Irrigation as a heat-mitigation strategy

The third research strand evaluated the potential of irrigating urban parks to mitigate heat during summer heatwaves. Field measurements were combined with informative vegetation layers to parameterize the ENVI-met model and quantify the thermal mitigation potential of combined irrigation and tree density scenarios in urban parks under contrasting microclimatic conditions. The model was validated at two sites with contrasting water management (irrigated and rainfed), while four irrigation scenarios (AS1–AS4), together with a non-irrigated baseline (BS), were simulated for eight selected parks showing low to high tree-density classes (CL1–CL4) and belonging to two microclimatic classes (IC and NR). An economic analysis was also performed to obtain a realistic evaluation of the cost-benefits of irrigating urban parks.

The main findings indicated that irrigation primarily affected daytime conditions, reducing temperature and increasing humidity. Irrigation and tree density contributed to cooling, with stronger effects when combined, as their interaction produced a clear synergistic cooling effect compared to baseline conditions. The economic analysis results showed diminishing returns, with the highest efficiency at lower irrigation investments.

The simulated irrigation scenarios stem on water availability, which could emerge as a critical constraint. Despite being a potential mitigation strategy, irrigation to cool down extreme summer temperatures may be of difficult realization, especially in areas facing water scarcity. In Europe, an average of 30% of the territory and 34% of the population experienced water scarcity during the 2000–2020 period. In Southern Europe, water scarcity affects about 70% of the population because of a combination of drought, insufficient water quantity, poor quality, and limited accessibility that results in water demand exceeding supply. These trends are not expected to improve in the future, as climate change will likely increase the frequency and intensity of drought events and intensify seasonal fluctuations in freshwater availability (EEA, 2025). To tackle water scarcity, recovering wastewater through treatment systems could be a promising solution (Pereira et al., 2002). Not only could an efficient wastewater treatment system mitigate water scarcity but also generate a water surplus, which may be used to irrigate green areas and, thus, help reduce extreme summer air temperatures. In this direction, the city of Prato, Italy, hosts a unique centralized wastewater treatment system, used mainly by the industrial sector and currently not used at full capacity. The high cumulative volumes estimated in this study could therefore be potentially covered by the reclaimed water.

The main limitations of this study rely on some model simplification assumptions, which could lead to deviations in the estimated cooling potential compared to real-world conditions. Many within-park heterogeneous characteristics, such as variability in soil texture, tree height, canopy shape, and spatial disposition, could substantially influence microclimatic responses and the effectiveness of irrigation-induced cooling. These features were necessarily generalized in the modelling framework, potentially overlooking fine-scale heterogeneities that modulate evapotranspiration, shading, and energy flux partitioning. Moreover, the model assumes homogeneous soil and vegetation parameters within each simulated park, neglecting the spatial gradients in hydraulic conductivity, root density, or leaf area index that are typically observed in real park settings. As a consequence, the simulated temperature reductions should be interpreted as potential upper or lower bounds rather than precise absolute estimates of actual cooling effects. Future work could benefit from incorporating more detailed vegetation structures, field-calibrated soil properties, and dynamic irrigation management data to enhance model realism and better capture the complex feedbacks between vegetation, soil moisture, and atmosphere in heterogeneous urban environments.

5.4 Synthesis and future directions

Overall, the three parts of this thesis underscore the complexity of urban heat risk and the need for integrated, multi-disciplinary approaches to mitigation. The risk assessment showed that heat exposure is not evenly distributed. The modelling work highlighted both the promise and limitations of using low-cost sensor networks and remote sensing to predict high-resolution temperatures; despite moderate predictive skill, the models identified hot-spots that aligned with socio-economic vulnerability, reinforcing the equity dimension of heat risk. The irrigation simulations demonstrated that water-based cooling can provide measurable relief during heatwaves but that its effectiveness depends on context (e.g., proximity to water bodies, canopy density) and requires substantial water resources. Several recommendations emerge from this integrated analysis:

- Expand and diversify data networks. In Prato and similar cities, investing in dense air quality and temperature sensor networks will improve the spatial representativeness of hazard assessments. Integrating high-resolution health data and socio-economic surveys can further refine risk analyses and support targeted interventions.
- Advance modelling techniques. Future research should explore non-linear and machine learning approaches to better capture microclimatic variability. Incorporating detailed land-use, building geometry, anthropogenic heat emissions and water bodies into models will likely enhance predictive performance. Coupling physical models such as ENVI-met with data-driven models may yield hybrid approaches that leverage the strengths of both.
- Design water-efficient mitigation. While irrigation provides cooling, its high-water demand calls for careful planning. Combining moderate irrigation with strategic vegetation management (e.g., mixed turfgrass and trees) and other interventions (cool pavements, reflective materials, shade

structures) can reduce reliance on water. Evaluating alternative water sources, such as greywater or harvested rainwater, may improve sustainability.

Enhance participatory governance – Engaging local stakeholders, including policy makers, health authorities and community members, in data collection and decision making can ensure that adaptation strategies align with social priorities. Co-designed surveys and citizen science initiatives may also enrich data sets and foster public support.

By combining risk assessment, modelling and mitigation analyses, this thesis provides a comprehensive framework for understanding and addressing urban heat hazards. The findings emphasize that effective adaptation requires not only technological solutions but also social and institutional innovations that account for environmental justice and resource constraints. As climate change intensifies heatwaves in Mediterranean cities, such integrated approaches will be essential for safeguarding public health and enhancing urban resilience.

References

Accetturo, A., Mocetti, S., 2019. Historical Origins and Developments of Italian Cities. Ital Econ J 5, 205–222. https://doi.org/10.1007/s40797-019-00097-w

Aleksandrowicz, O., Vuckovic, M., Kiesel, K., Mahdavi, A., 2017. Current trends in urban heat island mitigation research: Observations based on a comprehensive research repository. Urban Climate 21, 1–26. https://doi.org/10.1016/j.uclim.2017.04.002

Alizadeh, M.R., Abatzoglou, J.T., Adamowski, J.F., Prestemon, J.P., Chittoori, B., Akbari Asanjan, A., Sadegh, M., 2022. Increasing Heat-Stress Inequality in a Warming Climate. Earth's Future 10, e2021EF002488. https://doi.org/10.1029/2021EF002488

Allen, R.G. (Ed.), 2000. Crop evapotranspiration: guidelines for computing crop water requirements, repr. ed, FAO irrigation and drainage paper. Food and Agriculture Organization of the United Nations, Rome.

Alonso, L., Renard, F., 2019. Integrating Satellite-Derived Data as Spatial Predictors in Multiple Regression Models to Enhance the Knowledge of Air Temperature Patterns. Urban Science 3, 101. https://doi.org/10.3390/urbansci3040101

Anselin, L., 1995. Local Indicators of Spatial Association—LISA. Geographical Analysis 27, 93–115. https://doi.org/10.1111/j.1538-4632.1995.tb00338.x

Arbat, G., Pujol, J., Pelegrí, M., Puig-Bargués, J., Duran-Ros, M., Ramírez de Cartagena, F., 2013. An approach to costs and energy consumption in private urban Spanish Mediterranean landscapes from a simplified model in sprinkle irrigation. Span. j. agric. res. 11, 244–257. https://doi.org/10.5424/sjar/2013111-3113

ARPAT - Grafici per qualità dell'aria per zone omogenee [WWW Document], n.d. URL https://www.arpat.toscana.it/temi-ambientali/aria/qualita-aria/grafici_bollettino/index/PM10 (accessed 11.15.23).

Asmus, C., Hoffmann, P., Pietikäinen, J.-P., Böhner, J., Rechid, D., 2023. Modeling and evaluating the effects of irrigation on land–atmosphere interaction in southwestern Europe with the regional climate model REMO2020–iMOVE using a newly developed parameterization. Geoscientific Model Development 16, 7311–7337. https://doi.org/10.5194/gmd-16-7311-2023

Badaloni, C., De Sario, M., Caranci, N., de' Donato, F., Bolignano, A., Davoli, M., Leccese, L., Michelozzi, P., Leone, M., 2023. A spatial indicator of environmental and climatic vulnerability in Rome. Environment International 176, 107970. https://doi.org/10.1016/j.envint.2023.107970

Barlow, J.F., 2014. Progress in observing and modelling the urban boundary layer. Urban Climate 10, 216–240. https://doi.org/10.1016/j.uclim.2014.03.011

Barthwal, A., Sharma, K., 2022. Analysis and prediction of urban ambient and surface temperatures using internet of things. International Journal of System Assurance Engineering and Management 13, 516–532. https://doi.org/10.1007/s13198-021-01502-3

Battista, G., de Lieto Vollaro, R., Zinzi, M., 2019. Assessment of urban overheating mitigation strategies in a square in Rome, Italy. Solar Energy 180, 608–621. https://doi.org/10.1016/j.solener.2019.01.074

Bonett, D.G., Wright, T.A., 2000. Sample size requirements for estimating pearson, kendall and spearman correlations. Psychometrika 65, 23–28. https://doi.org/10.1007/BF02294183

Bonfils, C., Lobell, D., 2007. Empirical evidence for a recent slowdown in irrigation-induced cooling. Proceedings of the National Academy of Sciences 104, 13582–13587. https://doi.org/10.1073/pnas.0700144104

Brilli, L., Carotenuto, F., Andreini, B.P., Cavaliere, A., Esposito, A., Gioli, B., Martelli, F., Stefanelli, M., Vagnoli, C., Venturi, S., Zaldei, A., Gualtieri, G., 2021. Low-Cost Air Quality Stations' Capability to Integrate Reference Stations in Particulate Matter Dynamics Assessment. Atmosphere 12, 1065. https://doi.org/10.3390/atmos12081065

Broadbent, A.M., Coutts, A.M., Tapper, N.J., Demuzere, M., 2018. The cooling effect of irrigation on urban microclimate during heatwave conditions. Urban Climate 23, 309–329. https://doi.org/10.1016/j.uclim.2017.05.002

Bruse, M., Fleer, H., 1998. Simulating surface–plant–air interactions inside urban environments with a three-dimensional numerical model. Environmental Modelling & Software 13, 373–384. https://doi.org/10.1016/S1364-8152(98)00042-5

Burt, C.M., Mutziger, A.J., Allen, R.G., Howell, T.A., 2005. Evaporation Research: Review and Interpretation. Journal of Irrigation and Drainage Engineering 131, 37–58. https://doi.org/10.1061/(ASCE)0733-9437(2005)131:1(37)

Buyantuyev, A., Wu, J., 2010. Urban heat islands and landscape heterogeneity: linking spatiotemporal variations in surface temperatures to land-cover and socioeconomic patterns. Landscape Ecology 25, 17–33. https://doi.org/10.1007/s10980-009-9402-4

Cao, C., Lee, X., Liu, S., Schultz, N., Xiao, W., Zhang, M., Zhao, L., 2016. Urban heat islands in China enhanced by haze pollution. Nat Commun 7, 12509. https://doi.org/10.1038/ncomms12509

Caranci, N., Biggeri, A., Grisotto, L., Pacelli, B., Spadea, T., Costa, G., 2010. [The Italian deprivation index at census block level: definition, description and association with general mortality]. Epidemiol Prev 34, 167–176.

Carotenuto, F., Brilli, L., Gioli, B., Gualtieri, G., Vagnoli, C., Mazzola, M., Viola, A.P., Vitale, V., Severi, M., Traversi, R., Zaldei, A., 2020. Long-Term Performance Assessment of Low-Cost Atmospheric Sensors in the Arctic Environment. Sensors 20. https://doi.org/10.3390/s20071919

Cavaliere, A., Carotenuto, F., Di Gennaro, F., Gioli, B., Gualtieri, G., Martelli, F., Matese, A., Toscano, P., Vagnoli, C., Zaldei, A., 2018. Development of Low-Cost Air Quality Stations for Next Generation Monitoring Networks: Calibration and Validation of PM2.5 and PM10 Sensors. Sensors 18. https://doi.org/10.3390/s18092843

Chakraborty, T., Hsu, A., Manya, D., Sheriff, G., 2019. Disproportionately higher exposure to urban heat in lower-income neighborhoods: a multi-city perspective. Environ. Res. Lett. 14, 105003. https://doi.org/10.1088/1748-9326/ab3b99

Chen, T.-L., Lin, H., Chiu, Y.-H., 2022. Heat vulnerability and extreme heat risk at the metropolitan scale: A case study of Taipei metropolitan area, Taiwan. Urban Climate 41, 101054. https://doi.org/10.1016/j.uclim.2021.101054

Chen, Y., Wang, Y., Zhou, D., Luo, X., 2025. Regression-based predictive modeling of summer urban microclimate: Quantifying contributions from urban design and urban heat emissions. Urban Climate 62, 102550. https://doi.org/10.1016/j.uclim.2025.102550

Chen, Yapeng, Chen, Yaning, Xu, C., Li, W., 2016. The effects of groundwater depth on water uptake of Populus euphratica and Tamarix ramosissima in the hyperarid region of Northwestern China. Environmental Science and Pollution Research 23, 17404–17412. https://doi.org/10.1007/s11356-016-6914-8

Cheung, P.K., Livesley, S.J., Nice, K.A., 2021. Estimating the cooling potential of irrigating green spaces in 100 global cities with arid, temperate or continental climates. Sustainable Cities and Society 71, 102974. https://doi.org/10.1016/j.scs.2021.102974

Cheung, P.K., Nice, K.A., Livesley, S.J., 2024. Impacts of irrigation scheduling on urban green space cooling. Landscape and Urban Planning 248, 105103. https://doi.org/10.1016/j.landurbplan.2024.105103

Cheung, P.K., Nice, K.A., Livesley, S.J., 2022. Irrigating urban green space for cooling benefits: the mechanisms and management considerations. Environ. Res.: Climate 1, 015001. https://doi.org/10.1088/2752-5295/ac6e7c

Conte Keivabu, R., 2023. Spatial and temporal disparities in air pollution exposure at Italian schools. Genus 79, 27. https://doi.org/10.1186/s41118-023-00206-9

Cook, B.I., Puma, M.J., Krakauer, N.Y., 2011. Irrigation induced surface cooling in the context of modern and increased greenhouse gas forcing. Climate Dynamics 37, 1587–1600. https://doi.org/10.1007/s00382-010-0932-x

Coombes, M.A., Viles, H.A., 2021. Integrating nature-based solutions and the conservation of urban built heritage: Challenges, opportunities, and prospects. Urban Forestry & Urban Greening 63, 127192. https://doi.org/10.1016/j.ufug.2021.127192

Copernicus, 2023. 2023 in context. Copernicus, https://climate.copernicus.eu/esotc/2023/temperature-and-thermal-stress

Copernicus, 2023. European State of the Climate 2022 Summary. Copernicus. https://climate.copernicus.eu/esotc/2022/european-state-climate-2022-summary.

D’Amato, G., Vitale, C., De Martino, A., Viegi, G., Lanza, M., Molino, A., Sanduzzi, A., Vatrella, A., Annesi-Maesano, I., D’Amato, M., 2015. Effects on asthma and respiratory allergy of Climate change and air pollution. Multidisciplinary Respiratory Medicine 10, 39. https://doi.org/10.1186/s40248-015-0036-x

Dambha-Miller, H., Cheema, S., Saunders, N., Simpson, G., 2022. Multiple Long-Term Conditions (MLTC) and the Environment: A Scoping Review. International Journal of Environmental Research and Public Health 19, 11492. https://doi.org/10.3390/ijerph191811492

Daniel, M., Lemonsu, A., Viguié, V., 2018. Role of watering practices in large-scale urban planning strategies to face the heat-wave risk in future climate. Urban Climate, ICUC9: The 9th International Conference on Urban Climate 23, 287–308. https://doi.org/10.1016/j.uclim.2016.11.001

De Marco, A., Proietti, C., Anav, A., Ciancarella, L., D'Elia, I., Fares, S., Fornasier, M.F., Fusaro, L., Gualtieri, M., Manes, F., Marchetto, A., Mircea, M., Paoletti, E., Piersanti, A., Rogora, M., Salvati, L., Salvatori, E., Screpanti, A., Vialetto, G., Vitale, M., Leonardi, C., 2019. Impacts of air pollution on human and ecosystem health, and implications for the National Emission Ceilings Directive: Insights from Italy. Environment International 125, 320–333. https://doi.org/10.1016/j.envint.2019.01.064

Depietri, Y., Welle, T., Renaud, F.G., 2013. Social vulnerability assessment of the Cologne urban area (Germany) to heat waves: links to ecosystem services. International Journal of Disaster Risk Reduction 6, 98–117. https://doi.org/10.1016/j.ijdrr.2013.10.001

de Vries, D.A., 1959. THE INFLUENCE OF IRRIGATION ON THE ENERGY BALANCE AND THE CLIMATE NEAR THE GROUND. Journal of Atmospheric Sciences 16, 256–270. https://doi.org/10.1175/1520-0469(1959)016%253C0256:TIOIOT%253E2.0.CO;2

Di Giuseppe, E., Ulpiani, G., Cancellieri, C., Di Perna, C., D'Orazio, M., Zinzi, M., 2021. Numerical modelling and experimental validation of the microclimatic impacts of water mist cooling in urban areas. Energy and Buildings 231, 110638. https://doi.org/10.1016/j.enbuild.2020.110638

Decorte, T., Mortier, S., Lembrechts, J.J., Meysman, F.J.R., Latré, S., Mannens, E., Verdonck, T., 2024. Missing Value Imputation of Wireless Sensor Data for Environmental Monitoring. Sensors 24. https://doi.org/10.3390/s24082416

Doll, C.A., Pannell, D.J., Burton, M.P., 2024. Economic evaluation of alternative urban park designs that conserve irrigation water. Australian Journal of Agricultural and Resource Economics 68, 713–730. https://doi.org/10.1111/1467-8489.12582

EEA, 2023a. Europe's Air Quality Status 2023. https://doi.org/10.2800/59526.

EEA, 2023b. Harm to Human Health From Air Pollution in Europe: Burden of Disease 2023.

EEA, 2025. Water scarcity conditions in Europe https://www.eea.europa.eu/en/analysis/indicators/use-of-freshwater-resources-in-europe-1

Ellena, M., Melis, G., Zengarini, N., Di Gangi, E., Ricciardi, G., Mercogliano, P., Costa, G., 2023. Micro-scale UHI risk assessment on the heat-health nexus within cities by looking at socio-economic factors and built environment characteristics: The Turin case study (Italy). Urban Climate 49, 101514. https://doi.org/10.1016/j.uclim.2023.101514

ENVI-met A holistic microclimate model – Technical Model Webpage https://envi-met.info/doku.php?id=start

Eugenio Pappalardo, S., Zanetti, C., Todeschi, V., 2023. Mapping urban heat islands and heat-related risk during heat waves from a climate justice perspective: A case study in the municipality of Padua (Italy) for inclusive adaptation policies. Landscape and Urban Planning 238, 104831. https://doi.org/10.1016/j.landurbplan.2023.104831

Fairburn, J., Schüle, S.A., Dreger, S., Karla Hilz, L., Bolte, G., 2019. Social Inequalities in Exposure to Ambient Air Pollution: A Systematic Review in the WHO European Region. International Journal of Environmental Research and Public Health 16, 3127. https://doi.org/10.3390/ijerph16173127

Fallmann, J., Forkel, R., Emeis, S., 2016. Secondary effects of urban heat island mitigation measures on air quality. Atmospheric Environment 125, 199–211. https://doi.org/10.1016/j.atmosenv.2015.10.094

Fiorillo, E., Brilli, L., Carotenuto, F., Cremonini, L., Gioli, B., Giordano, T., Nardino, M., 2023. Diurnal Outdoor Thermal Comfort Mapping through Envi-Met Simulations, Remotely Sensed and In Situ Measurements. Atmosphere 14, 641. https://doi.org/10.3390/atmos14040641

Forceville, G., Lemonsu, A., Goria, S., Stempfelet, M., Host, S., Alessandrini, J.-M., Cordeau, E., Pascal, M., 2024. Spatial contrasts and temporal changes in fine-scale heat exposure and vulnerability in the Paris region. Science of The Total Environment 906, 167476. https://doi.org/10.1016/j.scitotenv.2023.167476

Fowler, W.B., Helvey, J.D., 1974. Effect of Large-Scale Irrigation on Climate in the Columbia Basin. Science 184, 121–127. https://doi.org/10.1126/science.184.4133.121

Gao, K., Haddad, S., Paolini, R., Feng, J., Altheeb, M., Mogirah, A.A., Moammar, A.B., Santamouris, M., 2024. The use of green infrastructure and irrigation in the mitigation of urban heat in a desert city. Building Simulation 17, 679–694. https://doi.org/10.1007/s12273-024-1110-0

Gao, K., Santamouris, M., Feng, J., 2020. On the cooling potential of irrigation to mitigate urban heat island. Science of The Total Environment 740, 139754. https://doi.org/10.1016/j.scitotenv.2020.139754

Germani, A.R., Morone, P., Testa, G., 2014. Environmental justice and air pollution: A case study on Italian provinces. Ecological Economics 106, 69–82. https://doi.org/10.1016/j.ecolecon.2014.07.010

Gkirmpas, P., Tsegas, G., Boehnke, D., Vlachokostas, C., Moussiopoulos, N., 2025. Temperature Prediction at Street Scale During a Heat Wave Using Random Forest. Atmosphere 16. https://doi.org/10.3390/atmos16070877

Gobatti, L., Bach, P.M., Maurer, M., Leitão, J.P., 2025. Impact of soil moisture content on urban tree evaporative cooling and human thermal comfort. npj Urban Sustainability 5, 26. https://doi.org/10.1038/s42949-025-00220-0

Gosztonyi, Á., Demmler, J.C., Juhola, S., Ala-Mantila, S., 2023. Ambient air pollution-related environmental inequality and environmental dissimilarity in Helsinki Metropolitan Area, Finland. Ecological Economics 213, 107930. https://doi.org/10.1016/j.ecolecon.2023.107930

Grossman, G.M., Krueger, A., 1995. Economic Growth and the Environment. The Quarterly Journal of Economics 110, 353–377.

Grote, R., Samson, R., Alonso, R., Amorim, J.H., Cariñanos, P., Churkina, G., Fares, S., Thiec, D.L., Niinemets, Ü., Mikkelsen, T.N., Paoletti, E., Tiwary, A., Calfapietra, C., 2016. Functional traits of urban trees: air pollution mitigation potential. Frontiers in Ecology and the Environment 14, 543–550. https://doi.org/10.1002/fee.1426

Gualtieri, G., Ahbil, K., Brilli, L., Carotenuto, F., Cavaliere, A., Gioli, B., Giordano, T., Katiellou, G.L., Mouhaimini, M., Tarchiani, V., Vagnoli, C., Zaldei, A., Bacci, M., 2024a. Potential of low-cost PM monitoring sensors to fill monitoring gaps in areas of Sub-Saharan Africa. Atmospheric Pollution Research 15, 102158. https://doi.org/10.1016/j.apr.2024.102158

Gualtieri, G., Brilli, L., Carotenuto, F., Cavaliere, A., Giordano, T., Putzolu, S., Vagnoli, C., Zaldei, A., Gioli, B., 2024b. Performance Assessment of Two Low-Cost PM2.5 and PM10 Monitoring Networks in the Padana Plain (Italy). Sensors 24. https://doi.org/10.3390/s24123946

Gualtieri, G., Brilli, L., Carotenuto, F., Vagnoli, C., Zaldei, A., Gioli, B., 2022. Long-term COVID-19 restrictions in Italy to assess the role of seasonal meteorological conditions and pollutant emissions on urban air quality. Atmosphere 13, 1156. https://doi.org/10.3390/atmos13071156

Guerri, G., Crisci, A., Messeri, A., Congedo, L., Munafò, M., Morabito, M., 2021. Thermal Summer Diurnal Hot-Spot Analysis: The Role of Local Urban Features Layers. Remote Sensing 13. https://doi.org/10.3390/rs13030538

Guha, S., Govil, H., Dey, A., Gill, N., 2018. Analytical study of land surface temperature with NDVI and NDBI using Landsat 8 OLI and TIRS data in Florence and Naples city, Italy. European Journal of Remote Sensing 51, 667–678. https://doi.org/10.1080/22797254.2018.1474494

Hami, A., Abdi, B., Zarehaghi, D., Maulan, S.B., 2019. Assessing the thermal comfort effects of green spaces: A systematic review of methods, parameters, and plants' attributes. Sustainable Cities and Society 49, 101634. https://doi.org/10.1016/j.scs.2019.101634

Havard, S., Deguen, S., Zmirou-Navier, D., Schillinger, C., Bard, D., 2009. Traffic-Related Air Pollution and Socioeconomic Status: A Spatial Autocorrelation Study to Assess Environmental Equity on a Small-Area Scale. Epidemiology 20, 223. https://doi.org/10.1097/EDE.0b013e31819464e1

Han, Q., Nan, X., Wang, H., Hu, Y., Bao, Z., Yan, H., 2023. Optimizing the Surrounding Building Configuration to Improve the Cooling Ability of Urban Parks on Surrounding Neighborhoods. Atmosphere 14, 914. https://doi.org/10.3390/atmos14060914

Heusinger, J., Sailor, D.J., Weber, S., 2018. Modeling the reduction of urban excess heat by green roofs with respect to different irrigation scenarios. Building and Environment 131, 174–183. https://doi.org/10.1016/j.buildenv.2018.01.003

Holobaca, I.-H., Alexe, M., Temerdek-Ivan, K., Ursu, C.-D., 2026. Enhanced Urban Heat Island Modeling with Machine Learning and Regression Kriging in a Topographically Diverse Medium-Sized City. Land 15, 49. https://doi.org/10.3390/land15010049

Hu, L., Brunsell, N.A., 2013. The impact of temporal aggregation of land surface temperature data for surface urban heat island (SUHI) monitoring. Remote Sensing of Environment 134, 162–174. https://doi.org/10.1016/j.rse.2013.02.022

Huang, C., Hu, T., Duan, Y., Li, Q., Chen, N., Wang, Q., Zhou, M., Rao, P., 2022. Effect of urban morphology on air pollution distribution in high-density urban blocks based on mobile monitoring and machine learning. Building and Environment 219, 109173. https://doi.org/10.1016/j.buildenv.2022.109173

Hulley, G., Shivers, S., Wetherley, E., Cudd, R., 2019. New ECOSTRESS and MODIS Land Surface Temperature Data Reveal Fine-Scale Heat Vulnerability in Cities: A Case Study for Los Angeles County, California. Remote Sensing 11, 2136. https://doi.org/10.3390/rs11182136

Huttner, S., 2012. Further development and application of the 3D microclimate simulation ENVI-met. Doctoral Thesis, Universitat Mainz.

ISTAT, 2022, Il Censimento permanente della popolazione in Toscana https://www.istat.it/it/files//2022/03/Il-Censimento-permanente-della-popolazione-in Toscana_focus-2.pdf (accessed 03 May 2024)

Jain, S., Rathee, S., Kumar, A., Sambasivam, A., Boadh, R., Choudhary, T., Kumar, P., Kumar Singh, P., 2022. Prediction of temperature for various pressure levels using ANN and multiple linear regression techniques: A case study. Materials Today: Proceedings 56, 194–199. https://doi.org/10.1016/j.matpr.2022.01.067

Janatian, N., Sadeghi, M., Sanaeinejad, S.H., Bakhshian, E., Farid, A., Hasheminia, S.M., Ghazanfari, S., 2017. A statistical framework for estimating air temperature using MODIS land surface temperature data. International Journal of Climatology 37, 1181–1194. https://doi.org/10.1002/joc.4766

Jennings, V., Reid, C.E., Fuller, C.H., 2021. Green infrastructure can limit but not solve air pollution injustice. Nat Commun 12, 4681. https://doi.org/10.1038/s41467-021-24892-1

Jiang, L., Ma, E., Deng, X., 2014. Impacts of Irrigation on the Heat Fluxes and Near-Surface Temperature in an Inland Irrigation Area of Northern China. Energies 7, 1300–1317. https://doi.org/10.3390/en7031300

Kaiser, H.F., 1974. An index of factorial simplicity. Psychometrika 39, 31–36. https://doi.org/10.1007/BF02291575

Kanabkaew, T., Mekbungwan, P., Raksakietisak, S., Kanchanasut, K., 2019. Detection of PM2.5 plume movement from IoT ground level monitoring data. Environmental Pollution 252, 543–552. https://doi.org/10.1016/j.envpol.2019.05.082

Kool, D., Agam, N., Lazarovitch, N., Heitman, J.L., Sauer, T.J., Ben-Gal, A., 2014. A review of approaches for evapotranspiration partitioning. Agricultural and Forest Meteorology 184, 56–70. https://doi.org/10.1016/j.agrformet.2013.09.003

Kottek, M., Grieser, J., Beck, C., Rudolf, B., Rubel, F., 2006. World Map of the Köppen-Geiger climate classification updated. Meteorologische Zeitschrift 15, 259–263. https://doi.org/10.1127/0941-2948/2006/0130

Kueppers, L.M., Snyder, M.A., Sloan, L.C., 2007. Irrigation cooling effect: Regional climate forcing by land-use change. Geophysical Research Letters 34. https://doi.org/10.1029/2006GL028679

Kumar, P., Morawska, L., Martani, C., Biskos, G., Neophytou, M., Di Sabatino, S., Bell, M., Norford, L., Britter, R., 2015. The rise of low-cost sensing for managing air pollution in cities. Environment International 75, 199–205. https://doi.org/10.1016/j.envint.2014.11.019

Lam, C.K.C., Gallant, A.J.E., Tapper, N.J., 2020. Does irrigation cooling effect intensify during heatwaves? A case study in the Melbourne botanic gardens. Urban Forestry & Urban Greening 55, 126815. https://doi.org/10.1016/j.ufug.2020.126815

IPCC, 2022, H.O. Portner, D.C. Roberts, M. Tignor, E.S. Poloczanska, K. Mintenbeck, A. Alegria, M. Craig, S. Langsdorf, S. Loschke, V. Moller, A. Okem, B. Rama (Eds.), Climate Change 2022: Impacts, Adaptation, and Vulnerability. Contribution of Working Group II to the Sixth Assessment Report of the Intergovernmental Panel on Climate Change, Cambridge University Press (2022)

Li, J. et Heap, A.D., 2008. A Review of Spatial Interpolation Methods for Environmental Scientists. Geoscience Australia, Record 2008/23, 137 pp.

Li, Y., Schubert, S., Kropp, J.P., Rybski, D., 2020. On the influence of density and morphology on the Urban Heat Island intensity. Nat Commun 11, 2647. https://doi.org/10.1038/s41467-020-164619

Li, H., Zhao, Y., Wang, C., Ürge-Vorsatz, D., Carmeliet, J., Bardhan, R., 2024. Cooling efficacy of trees across cities is determined by background climate, urban morphology, and tree trait. Communications Earth & Environment 5, 754. https://doi.org/10.1038/s43247-024-01908-4

Li, X., Li, Xing, Hua, W., Ma, H., Zhou, J., Pang, X., 2023a. Modeling the effects of present-day irrigation on temperature extremes over China. Frontiers in Earth Science Volume 11-2023. https://doi.org/10.3389/feart.2023.1084892

Li, Y., Ma, Y., Song, X., Zhang, Q., Wang, L., 2023b. Quantifying river water contributions to the transpiration of riparian trees along a losing river: lessons from stable isotopes and an iteration method. Hydrol. Earth Syst. Sci. 27, 3405–3425. https://doi.org/10.5194/hess-27-3405-2023

Liu, Z., Zheng, S., Zhao, L., 2018. Evaluation of the ENVI-Met Vegetation Model of Four Common Tree Species in a Subtropical Hot-Humid Area. Atmosphere 9. https://doi.org/10.3390/atmos9050198

Lunel, T., Boone, A.A., Le Moigne, P., 2024. Irrigation strongly influences near-surface conditions and induces breeze circulation: Observational and model-based evidence. Quarterly Journal of the Royal Meteorological Society 150, 2798–2819. https://doi.org/10.1002/qj.4736

Lv, C., He, Y., Zhang, W., Gu, C., Li, Y., Yan, D., 2021. Quantitative Analysis of Eco-economic Benefits of Urban Reclaimed Water Greening Based on Emergy Theory. Water Resources Management 35, 5029–5047. https://doi.org/10.1007/s11269-021-02987-0

M. A. Zaidan, Y. Xie, N. H. Motlagh, B. Wang, W. Nie, P. Nurmi, S. Tarkoma, T. Petäjä, A. Ding, M. Kulmala, 2022. Dense Air Quality Sensor Networks: Validation, Analysis, and Benefits. IEEE Sensors Journal 22, 23507–23520. https://doi.org/10.1109/JSEN.2022.3216071

Meade, R.D., Akerman, A.P., Notley, S.R., McGinn, R., Poirier, P., Gosselin, P., Kenny, G.P., 2020. Physiological factors characterizing heat-vulnerable older adults: A narrative review. Environment International 144, 105909. https://doi.org/10.1016/j.envint.2020.105909

Missik, J.E.C., Liu, H., Gao, Z., Huang, M., Chen, X., Arntzen, E., Mcfarland, D.P., Ren, H., Titzler, P.S., Thomle, J.N., Goldman, A., 2019. Groundwater-River Water Exchange Enhances Growing Season Evapotranspiration and Carbon Uptake in a Semiarid Riparian Ecosystem. Journal of Geophysical Research: Biogeosciences 124, 99–114. https://doi.org/10.1029/2018JG004666

Moran, P.A.P., 1950. Notes on Continuous Stochastic Phenomena. Biometrika 37, 17–23. https://doi.org/10.2307/2332142

Morakinyo, T.E., Kong, L., Lau, K.K.-L., Yuan, C., Ng, E., 2017. A study on the impact of shadow-cast and tree species on in-canyon and neighborhood's thermal comfort. Building and Environment 115, 1–17. https://doi.org/10.1016/j.buildenv.2017.01.005

Nardino, M., Cremonini, L., Crisci, A., Georgiadis, T., Guerri, G., Morabito, M., Fiorillo, E., 2022. Mapping daytime thermal patterns of Bologna municipality (Italy) during a heatwave: A new methodology for cities adaptation to global climate change. Urban Climate 46, 101317. https://doi.org/10.1016/j.uclim.2022.101317

Niu, L., Zhang, Z., Liang, Y., van Vliet, J., 2024. Spatiotemporal patterns and drivers of the urban air pollution island effect for 2273 cities in China. Environment International 184, 108455. https://doi.org/10.1016/j.envint.2024.108455

Nocco, M.A., Smail, R.A., Kucharik, C.J., 2019. Observation of irrigation-induced climate change in the Midwest United States. Global Change Biology 25, 3472–3484. https://doi.org/10.1111/gcb.14725

Oke, T.R., 1981. Canyon geometry and the nocturnal urban heat island: Comparison of scale model and field observations. Journal of Climatology 1, 237–254. https://doi.org/10.1002/joc.3370010304

Oke, T.R., 1982. The energetic basis of the urban heat island. Quarterly Journal of the Royal Meteorological Society 108, 1–24. https://doi.org/10.1002/qj.49710845502

Oke, T.R., Maxwell, G.B., 1975. Urban heat island dynamics in Montreal and Vancouver. Atmospheric Environment (1967) 9, 191–200. https://doi.org/10.1016/0004-6981(75)90067-0

O'Lenick, C.R., Wilhelmi, O.V., Michael, R., Hayden, M.H., Baniassadi, A., Wiedinmyer, C., Monaghan, A.J., Crank, P.J., Sailor, D.J., 2019. Urban heat and air pollution: A framework for integrating population vulnerability and indoor exposure in health risk analyses. Science of The Total Environment 660, 715–723. https://doi.org/10.1016/j.scitotenv.2019.01.002

Olivieri, F., Sassenou, L.-N., Olivieri, L., 2024. Potential of Nature-Based Solutions to Diminish Urban Heat Island Effects and Improve Outdoor Thermal Comfort in Summer: Case Study of Matadero Madrid. Sustainability 16, 2778. https://doi.org/10.3390/su16072778

OpenDataNetwork - Comune di Prato. http://odn.comune.prato.it/dataset/edificato-prato

Pace, R., De Fino, F., Rahman, M.A., Pauleit, S., Nowak, D.J., Grote, R., 2021. A single tree model to consistently simulate cooling, shading, and pollution uptake of urban trees. International Journal of Biometeorology 65, 277–289. https://doi.org/10.1007/s00484-020-02030-8

PAESC - Piano d'Azione per l'Energia Sostenibile e il Clima. https://www.comune.prato.it/it/per-i-cittadini/ambiente-sostenibile/paes/pagina139.html

Pereira, L.S., Oweis, T., Zairi, A., 2002. Irrigation management under water scarcity. Agricultural Water Management 57, 175–206. https://doi.org/10.1016/S0378-3774(02)00075-6

Perkins, S.E., 2015. A review on the scientific understanding of heatwaves—Their measurement, driving mechanisms, and changes at the global scale. Atmospheric Research 164–165, 242–267. https://doi.org/10.1016/j.atmosres.2015.05.014

Potchter, O., Cohen, P., Bitan, A., 2006. Climatic behavior of various urban parks during hot and humid summer in the mediterranean city of Tel Aviv, Israel. International Journal of Climatology 26, 1695–1711. https://doi.org/10.1002/joc.1330

Rahman, M.A., Stratopoulos, L.M.F., Moser-Reischl, A., Zölch, T., Häberle, K.-H., Rötzer, T., Pretzsch, H., Pauleit, S., 2020. Traits of trees for cooling urban heat islands: A meta-analysis. Building and Environment 170, 106606. https://doi.org/10.1016/j.buildenv.2019.106606

Rakowska, S.B., Adams, M.D., 2024. Modelling the microscale spatial distribution of urban air temperature in suburban sprawl. Urban Climate 58, 102136. https://doi.org/10.1016/j.uclim.2024.102136

Rocha, A.D., Vulova, S., Förster, M., Gioli, B., Matthews, B., Helfter, C., Meier, F., Steeneveld, G.-J., Barlow, J.F., Järvi, L., Chrysoulakis, N., Nicolini, G., Kleinschmit, B., 2024. Unprivileged groups are less served by green cooling services in major European urban areas. Nature Cities 1, 424–435. https://doi.org/10.1038/s44284-024-00077-x

Rousi, E., Kornhuber, K., Beobide-Arsuaga, G., Luo, F., Coumou, D., 2022. Accelerated western European heatwave trends linked to more-persistent double jets over Eurasia. Nat Commun 13, 3851. https://doi.org/10.1038/s41467-022-31432-y

Sæbø, A., Janh¨all, S., Gawronski, S.W., Hanslin, H.M., 2017. Urban Forestry and Pollution Mitigation. Routledge Handbook of Urban Forestry, 1st edition. Imprint

Sade, N., Gebremedhin, A., Moshelion, M., 2012. Risk-taking plants. Plant Signaling & Behavior 7, 767–770. https://doi.org/10.4161/psb.20505

Saher, R., Stephen, H., Ahmad, S., 2021. Urban evapotranspiration of green spaces in arid regions through two established approaches: a review of key drivers, advancements, limitations, and potential opportunities. Urban Water Journal 18, 115–127. https://doi.org/10.1080/1573062X.2020.1857796

Salman, A.M., Saleem, Y.M., 2021. The effect of Urban Heat Island mitigation strategies on outdoor human thermal comfort in the city of Baghdad. Frontiers of Architectural Research 10, 838–856. https://doi.org/10.1016/j.foar.2021.07.002

Scharfstädt, L., Schöneberger, P., Simon, H., Sinsel, T., Nahtz, T., Bruse, M., 2024. From Oasis to Desert: The Struggle of Urban Green Spaces Amid Heatwaves and Water Scarcity. Sustainability 16, 3373. https://doi.org/10.3390/su16083373

Shurtz, K.M., Dicataldo, E., Sowby, R.B., Williams, G.P., 2022. Insights into Efficient Irrigation of Urban Landscapes: Analysis Using Remote Sensing, Parcel Data, Water Use, and Tiered Rates. Sustainability 14. https://doi.org/10.3390/su14031427

Sicard, P., Agathokleous, E., Anenberg, S.C., De Marco, A., Paoletti, E., Calatayud, V., 2023. Trends in urban air pollution over the last two decades: A global perspective. Science of The Total Environment 858, 160064. https://doi.org/10.1016/j.scitotenv.2022.160064

Sicard, P., Agathokleous, E., De Marco, A., Paoletti, E., Calatayud, V., 2021. Urban population exposure to air pollution in Europe over the last decades. Environmental Sciences Europe 33, 28. https://doi.org/10.1186/s12302-020-00450-2

Simoni, M., Baldacci, S., Maio, S., Cerrai, S., Sarno, G., Viegi, G., 2015. Adverse effects of outdoor pollution in the elderly. J Thorac Dis 7, 34–45. https://doi.org/10.3978/j.issn.2072-1439.2014.12.10.

Sobrino, J.A., Jiménez-Muñoz, J.C., Paolini, L., 2004. Land surface temperature retrieval from LANDSAT TM 5. Remote Sensing of Environment 90, 434–440. https://doi.org/10.1016/j.rse.2004.02.003

Spano, D., Mereu, V., Bacciu, V., Barbato, G., Buonocore, M., Casartelli, V., Ellena, M., Lamesso, E., Ledda, A., Marras, S., Mercogliano, P., Monteleone, L., Mysiak, J., Padulano, R., Raffa, M., Ruiu, M.G.G., Serra, V., Villani, V., 2021. Analisi del rischio. I cambiamenti climatici in sei citt`a italiane. https://doi.org/10.25424/cmcc/analisi_del_rischio_2021

Sorooshian, S., Li, J., Hsu, K., Gao, X., 2011. How significant is the impact of irrigation on the local hydroclimate in California's Central Valley? Comparison of model results with ground and remote-sensing data. Journal of Geophysical Research: Atmospheres 116. https://doi.org/10.1029/2010JD014775

Spronken-Smith, R.A., Oke, T.R., Lowry, W.P., 2000. Advection and the surface energy balance across an irrigated urban park. International Journal of Climatology 20, 1033–1047. https://doi.org/10.1002/1097-0088(200007)20:9%253C1033::AID-JOC508%253E3.0.CO;2-U

Spronken-Smith, R.A., Oke, T.R., 1998. The thermal regime of urban parks in two cities with different summer climates. International Journal of Remote Sensing 19, 2085–2104. https://doi.org/10.1080/014311698214884

Stafoggia, M., Schwartz, J., Badaloni, C., Bellander, T., Alessandrini, E., Cattani, G., de' Donato, F., Gaeta, A., Leone, G., Lyapustin, A., Sorek-Hamer, M., de Hoogh, K., Di, Q., Forastiere, F., Kloog, I., 2017. Estimation of daily PM10 concentrations in Italy (2006–2012) using finely resolved satellite data, land use variables and meteorology. Environment International 99, 234–244. https://doi.org/10.1016/j.envint.2016.11.024

Tobias, S., Carlson, J.E., 1969. BRIEF REPORT: BARTLETT'S TEST OF SPHERICITY AND CHANCE FINDINGS IN FACTOR ANALYSIS. Multivariate Behavioral Research. https://doi.org/10.1207/s15327906mbr0403_8

Trane, M., Giovanardi, M., Pejovic, A., Pollo, R., 2024. Overview on Urban Climate and Microclimate Modeling Tools and Their Role to Achieve the Sustainable Development Goals, in: Barberio, M., Colella, M., Figliola, A., Battisti, A. (Eds.), Architecture and Design for Industry 4.0: Theory and Practice. Springer International Publishing, Cham, pp. 247–267. https://doi.org/10.1007/978-3-031-36922-3_15

Tsoka, S., Tsikaloudaki, A., Theodosiou, T., 2018. Analyzing the ENVI-met microclimate model's performance and assessing cool materials and urban vegetation applications–A review. Sustainable Cities and Society 43, 55–76. https://doi.org/10.1016/j.scs.2018.08.009

Tyrväinen, L., Ojala, A., Korpela, K., Lanki, T., Tsunetsugu, Y., Kagawa, T., 2014. The influence of urban green environments on stress relief measures: A field experiment. Journal of Environmental Psychology 38, 1–9. https://doi.org/10.1016/j.jenvp.2013.12.005

Ulpiani, G., 2021. On the linkage between urban heat island and urban pollution island: Three-decade literature review towards a conceptual framework. Science of The Total Environment 751, 141727. https://doi.org/10.1016/j.scitotenv.2020.141727

Venter, Z.S., Brousse, O., Esau, I., Meier, F., 2020. Hyperlocal mapping of urban air temperature using remote sensing and crowdsourced weather data. Remote Sensing of Environment 242, 111791. https://doi.org/10.1016/j.rse.2020.111791

Venter, Z.S., Figari, H., Krange, O., Gundersen, V., 2023. Environmental justice in a very green city: Spatial inequality in exposure to urban nature, air pollution and heat in Oslo, Norway. Science of The Total Environment 858, 160193. https://doi.org/10.1016/j.scitotenv.2022.160193

Vesala, T., Kljun, N., Rannik, Ü., Rinne, J., Sogachev, A., Markkanen, T., Sabelfeld, K., Foken, Th., Leclerc, M.Y., 2008. Flux and concentration footprint modelling: State of the art. Environmental Pollution 152, 653–666. https://doi.org/10.1016/j.envpol.2007.06.070

Vries, D.A. de, 1959. THE INFLUENCE OF IRRIGATION ON THE ENERGY BALANCE AND THE CLIMATE NEAR THE GROUND. Journal of the Atmospheric Sciences 16, 256–270. https://doi.org/10.1175/1520-0469(1959)016%253C0256:TIOIOT%253E2.0.CO;2

Wang, C., Wang, Z.-H., Yang, J., 2019. Urban water capacity: Irrigation for heat mitigation. Computers, Environment and Urban Systems 78, 101397. https://doi.org/10.1016/j.compenvurbsys.2019.101397

Wang, M., He, G., Zhang, Zhaoming, Wang, G., Zhang, Zhengjia, Cao, X., Wu, Z., Liu, X., 2017. Comparison of Spatial Interpolation and Regression Analysis Models for an Estimation of Monthly Near Surface Air Temperature in China. Remote Sensing 9, 1278. https://doi.org/10.3390/rs9121278

WHO, 2004. Heat-Waves: Risks and Responses. https://www.who.int/publications-detail-redirect/9789289010948 (accessed 15 Feb 2024)

WHO, 2024. From smog hanging over cities to smoke inside the home, air pollution poses a major threat to health and climate across the globe. https://www.who.int/teams/environment-climate-change-and-health/air-quality-energy-and-health/health-impacts (accessed 15 Feb 2024)

Wolch, J.R., Byrne, J., Newell, J.P., 2014. Urban green space, public health, and environmental justice: The challenge of making cities 'just green enough.' Landscape and Urban Planning 125, 234–244. https://doi.org/10.1016/j.landurbplan.2014.01.017

Xu, H., Wang, C.C., Shen, X., Zlatanova, S., Paolini, R., 2025. Refined definition of level-of-detail for tree models in support of microclimate simulation. Sustainable Cities and Society 126, 106387. https://doi.org/10.1016/j.scs.2025.106387

Yang, Q., Huang, X., Tang, Q., 2020. Irrigation cooling effect on land surface temperature across China based on satellite observations. Science of The Total Environment 705, 135984. https://doi.org/10.1016/j.scitotenv.2019.135984

Yardley, J., Sigal, R.J., Kenny, G.P., 2011. Heat health planning: The importance of social and community factors. Global Environmental Change 21, 670–679. https://doi.org/10.1016/j.gloenvcha.2010.11.010

Yoshida, R., Iizumi, T., Nishimori, M., Yokozawa, M., 2012. Impacts of land-use changes on surface warming rates and rice yield in Shikoku, western Japan. Geophysical Research Letters 39. https://doi.org/10.1029/2012GL053711

Yu, C.-C., Quinn, J.T., Dufournaud, C.M., Harrington, J.J., Rogers, P.P., Lohani, B.N., 1998. Effective dimensionality of environmental indicators: a principal component analysis with bootstrap confidence intervals. Journal of Environmental Management 53, 101–119. https://doi.org/10.1006/jema.1998.0184

Zhu, J.-J., Yang, M., Ren, Z.J., 2023. Machine Learning in Environmental Research: Common Pitfalls and Best Practices. Environ. Sci. Technol. 57, 17671–17689. https://doi.org/10.1021/acs.est.3c00026

Appendix

Appendix A

Table A1. Technical specifications of AirQino low-cost sensors deployed in Prato.

Parameter	Sensor	Unit	Min	Max	Resolution	Accuracy
Air temperature	AM2315	°C	-40	80	0.30	5%
$PM_{2.5}$, PM_{10}	SDS011	µg/m^3	0	1000	1.00	10%

Table A2. Yearly income deciles and corresponding classes.

Decile	Income classes (€)	No. census tracts
1	< 3,000	2
2	3,000-6,856	3
3	6,857-10,359	8
4	10,360 - 13,809	70
5	13,810-16,798	245
6	16,798 - 19,646	376
7	19,647 - 22,873	301
8	22,874 - 27,243	147
9	27,243 - 35,589	110
10	> 35,589	61
No Data		151

Table A3. Deprivation Index. The data from each parameter were standardized and summed up to generate the final indicator.

Parameter	Description
Low education	Percentage of population aged over 9 with an education level equal to or lower than primary school
Unemployment	Rate of unemployed population
No-house ownership	Percentage of rented residential buildings
Population density	Number of inhabitants per 100 m^2 in residential buildings

Table A4. Location IDs and number of census tracts per location. IDs 1-20 denote LC stations, while IDs 21-23 denote reference stations.

ID	Location name	No. census tracts
01	Baciacavallo	15
02	Campaccio	49
03	Cava	14
04	Da Vinci	18
05	ESTRA	37
06	GIDA	14
07	Giordano	32
08	Longobarda	15
09	Mannocci	21
10	Marradi	19
11	Narnali	18
12	Nenni G. (*garden area*)	25
13	Nenni P. (*parking lot*)	22
14	S. Stefano	10
15	Ragnaia	22
16	Reggiana	13

17	S. Giorgio	17
18	Tavola	16
19	Turchia	11
20	Veneto	63
21	Ferrucci (ARPAT)	45
22	Roma (ARPAT)	60
23	Università (SIR)	53
Total	All	609

Table A5. Mean and standard deviation values of the investigated variables for the whole city (a) and within locations of the stations (b). NaN = missing data.

ID	Location name	PM_{10}	$PM_{2.5}$	AirT	UHTI	FEP	I	DI
		μg m^{-3}		°C		Index		
01	Baciacavallo	18.4±0.5	7.7±0.3	28.3±0.2	0.63±0.01	0.24±0.03	6.0±0.3	0.57±0.2
02	Campaccio	15.6±0.7	8.5±0.4	28.4±0.2	0.75±0.01	0.21±0.01	5.6±0.1	1.01±0.2
03	Cava	48.7±2.0	25.1±1.1	NaN	0.65±0.01	0.21±0.01	6.2±0.3	-0.30±0.2
04	Da Vinci	24.9±1.0	17.1±0.7	28.3±0.2	0.67±0.01	0.32±0.04	7.0±0.3	0.01±0.5
05	ESTRA	33.2±1.3	22.2±0.8	28.0±0.1	0.71±0.01	0.20±0.01	5.9±0.1	0.54±0.2
06	GIDA	37.7±1.3	23.4±0.8	28.0±0.1	0.65±0.02	0.27±0.03	6.0±0.2	0.08±0.4
07	Giordano	14.6±1.1	11.6±0.6	28.5±0.2	0.76±0.01	0.14±0.01	5.3±0.2	1.30±0.3
08	Longobarda	50.1±3.2	27.1±1.2	27.4±0.2	0.66±0.01	0.21±0.04	6.1±0.3	0.05±0.4
09	Mannocci	NaN	NaN	27.5±0.2	0.70±0.01	0.21±0.01	6.5±0.2	0.10±0.5
10	Marradi	NaN	NaN	26.6±0.2	0.67±0.01	0.27±0.02	6.8±0.2	-0.78±0.2
11	Narnali	22.1±0.8	12.6±0.5	28.3±0.2	0.69±0.01	0.26±0.02	6.6±0.3	0.28±0.4
12	Nenni G. (*garden area*)	24.8±1.0	19.8±0.8	27.9±0.2	0.74±0.01	0.18±0.02	6.0±0.2	0.66±0.2
13	Nenni P. (*parking lot*)	17.6±0.6	10.8±0.4	28.0±0.2	0.73±0.01	0.18±0.02	6.0±0.2	0.81±0.2
14	S. Stefano	NaN	NaN	28.1±0.2	0.67±0.01	0.26±0.02	7.1±0.3	-0.52±0.3
15	Ragnaia	17.0±0.9	13.6±0.6	27.0±0.2	0.66±0.01	0.31±0.02	7.4±0.2	-0.94±0.4
16	Reggiana	29.5±1.4	20.0±1.0	27.4±0.2	0.71±0.01	0.24±0.02	6.2±0.3	-0.78±0.4
17	S. Giorgio	27.5±1.3	21.6±0.9	27.9±0.2	0.70±0.01	0.25±0.02	6.0±0.2	1.00±0.7
18	Tavola	19.1±0.7	11.0±0.4	27.8±0.2	0.67±0.01	0.22±0.02	6.7±0.3	-0.27±0.3
19	Turchia	25.0±1.3	15.9±0.8	27.6±0.1	0.67±0.01	0.23±0.01	5.6±0.3	1.58±0.8
20	Veneto	19.1±0.7	12.7±0.5	27.6±0.2	0.73±0.01	0.21±0.01	7.4±0.2	-0.15±0.3
21	Ferrucci (ARPAT)	26.9±1.6	18.5±1.2	NaN	0.70±0.01	0.23±0.01	7.4±0.2	-0.14±0.3
22	Roma (ARPAT)	30.3±1.8	23.9±1.5	NaN	0.74±0.01	0.20±0.01	6.2±0.1	0.44±0.2
23	Università (SIR)	NaN	NaN	27.2±0.1	0.72±0.01	0.17±0.02	6.5±0.2	0.56±0.3
	Average	26.4±1.22	17.0±0.76	27.8±0.2	0.70±0.1	0.23±0.02	6.3±0.2	0.22±0.3

Table A6. Correlation coefficients on hazards and vulnerabilities and 95% confidence intervals (a) and regression results (b). Linear regressions ($y=\beta_0+\beta_1 x$) were run with y as the vulnerabilities and x as hazards. β_1 ($\frac{\partial y}{\partial x}$) expresses the variation of y corresponding to a one-unit change of x. * p-value < 0.05; ** p-value < 0.01; *** p-value < 0.001 (Two-tailed).

Hazard	Vulnerability	a)		b)
		R	R 95% confidence interval	Regression slope (β_1)
UHTI	I	–0.94**	[–0.99; –0.54]	-71.41**
	DI	0.96**	[0.67; 0.99]	61.67**
AirT	I	–0.88*	[–0.99; –0.24]	-8.87*
	DI	0.84*	[0.09; 0.98]	7.63*
PM_{10}	I	0.21	[–0.73; 0.87]	-0.04
	DI	–0.25	[–0.88; 0.70]	-0.08
$PM_{2.5}$	I	0.16	[–0.74; 0.86]	0.77
	DI	–0.15	[–0.85; 0.75]	-0.14

Table A7. Correlation matrix used for PCA computed on data aggregated at census tract level. * p-value < 0.05; ** p-value < 0.01; *** p-value < 0.001 (Two-tailed).

	PM_{10}	$PM_{2.5}$	AirT	UHTI	I	DI	FEP
PM_{10}	-						
$PM_{2.5}$	0.92***	-					
AirT	-0.25***	-0.31***	-				
UHTI	-0.25***	-0.18***	0.24***	-			
I	-0.03	-0.01	-0.36***	-0.29***	-		
DI	-0.04	-0.04	0.21***	0.24***	-0.54***	-	
FEP	0.07	0.06	-0.16**	-0.25***	0.20***	-0.30***	-

Figure A1. Map of Italy, also showing the Po Valley (green shaded area). Cartography basemap: Bing.

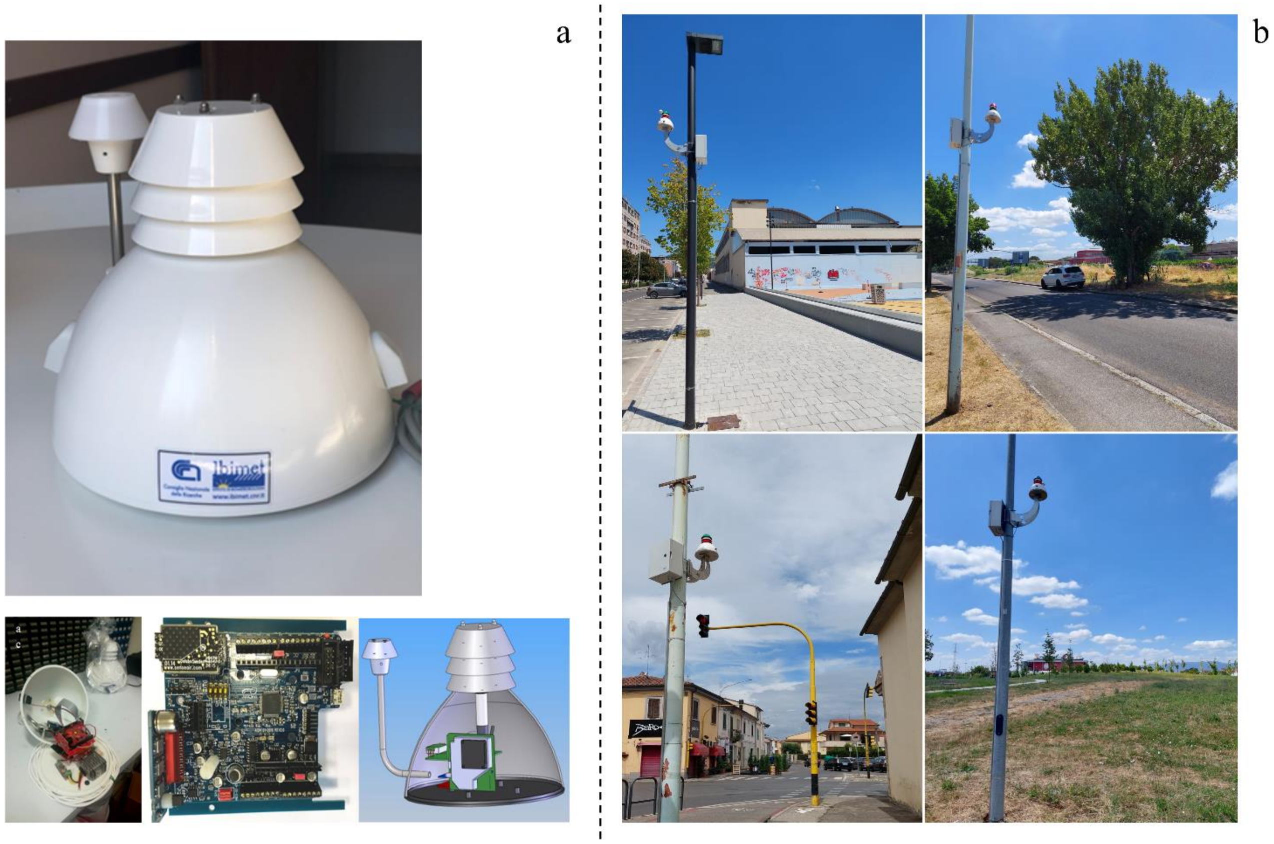

Figure A2. Pictures of the AirQino low-cost air quality monitoring station: (a) layout of the unit and internal motherboard; (b) unit’s installation within Prato municipality.

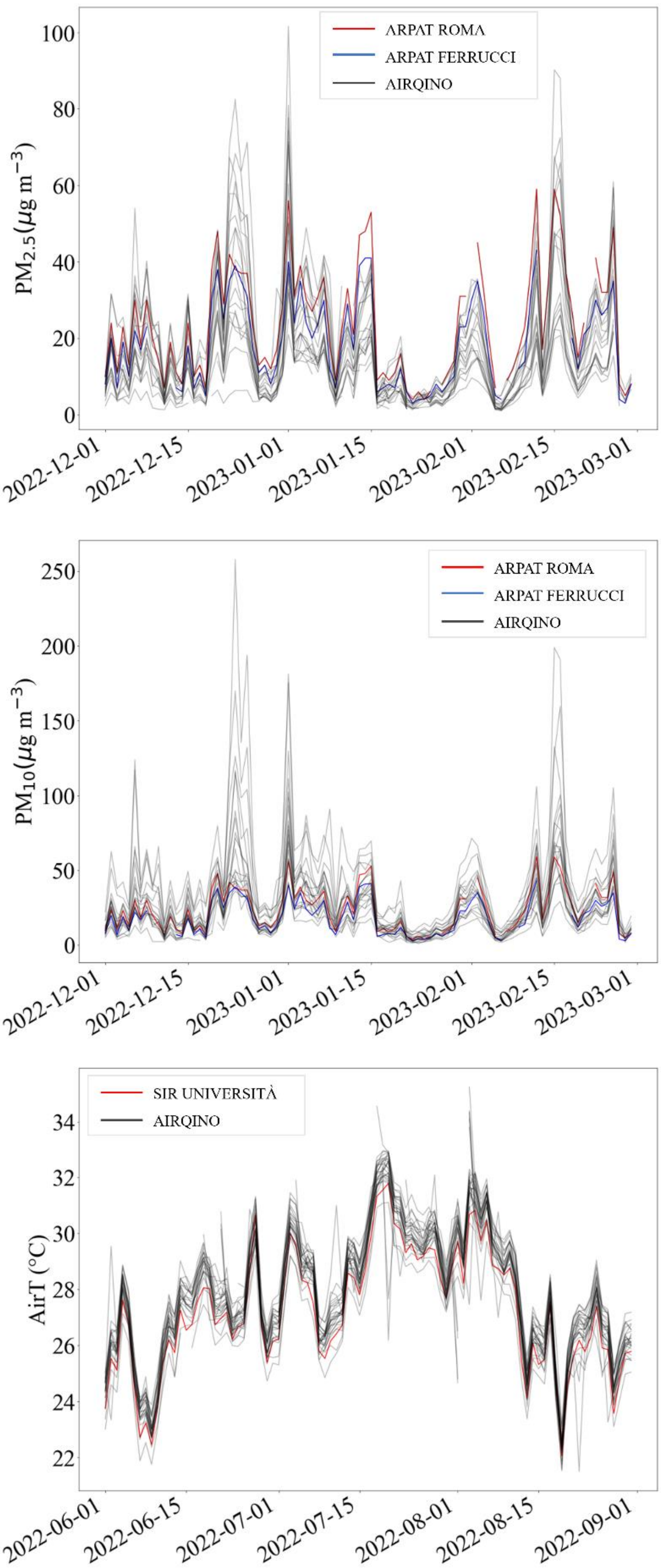

Figure A3. Time series of $PM_{2.5}$ and PM_{10} concentrations and air temperature measured in Prato by the AirQino sensor network as compared to data from the official reference stations (i.e., ARPAT and SIR).

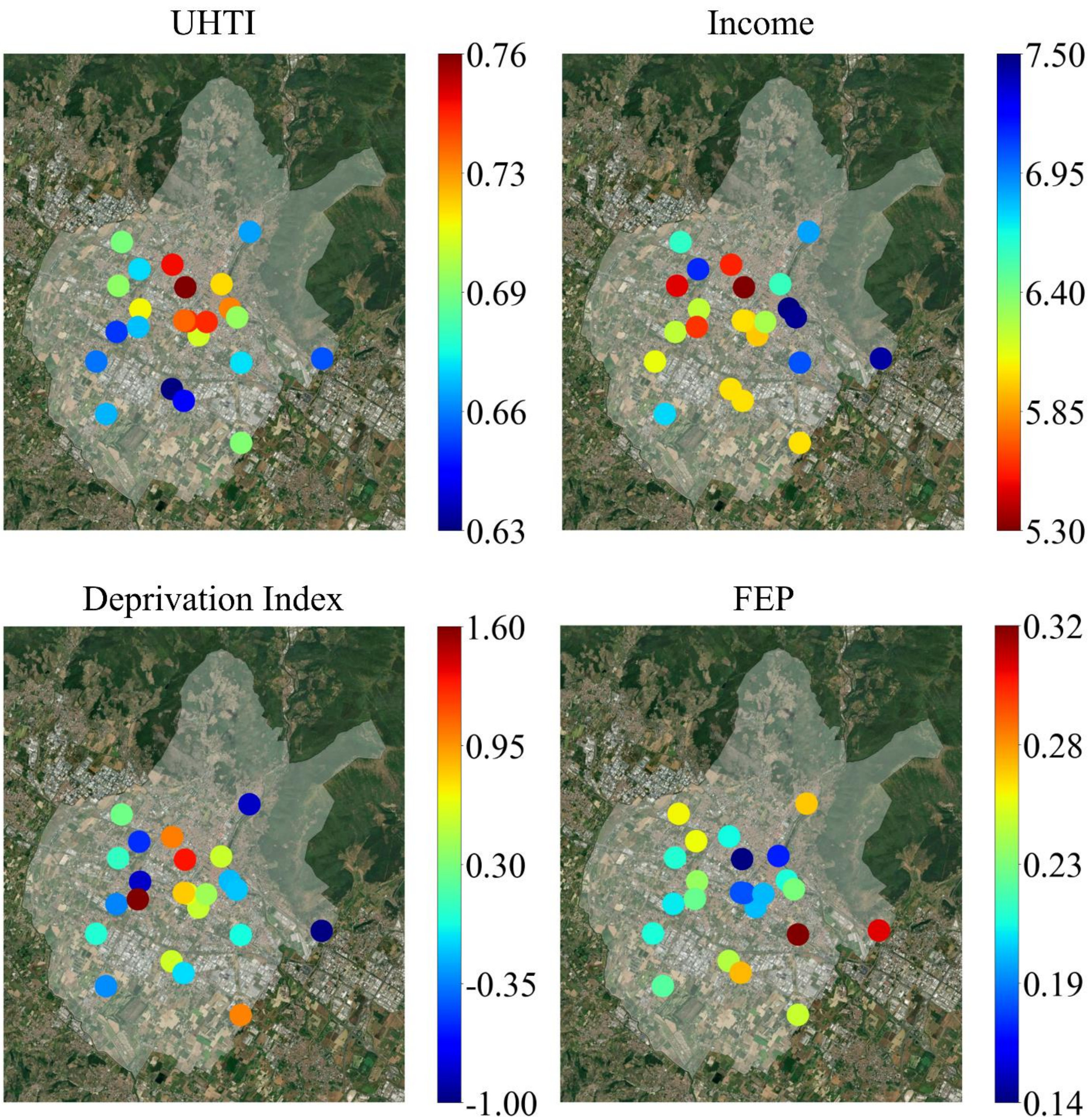

Figure A4. Average values of UHTI, Income, Deprivation index and FEP for each circular buffer analyzed within the Municipality of Prato.

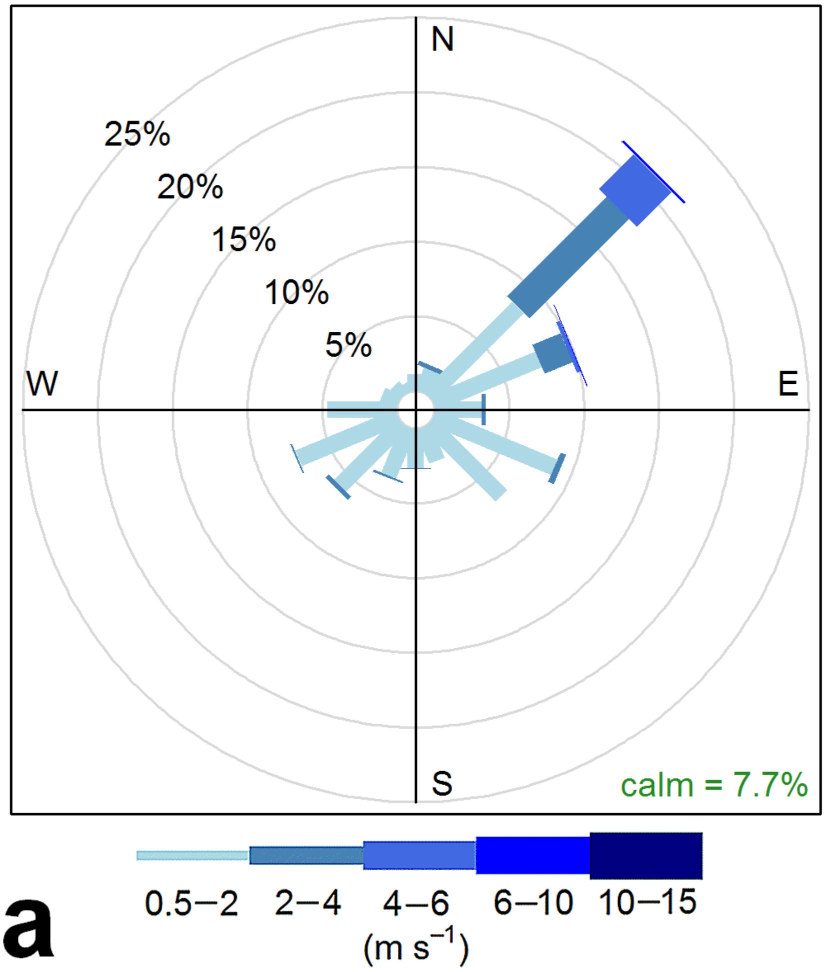

a

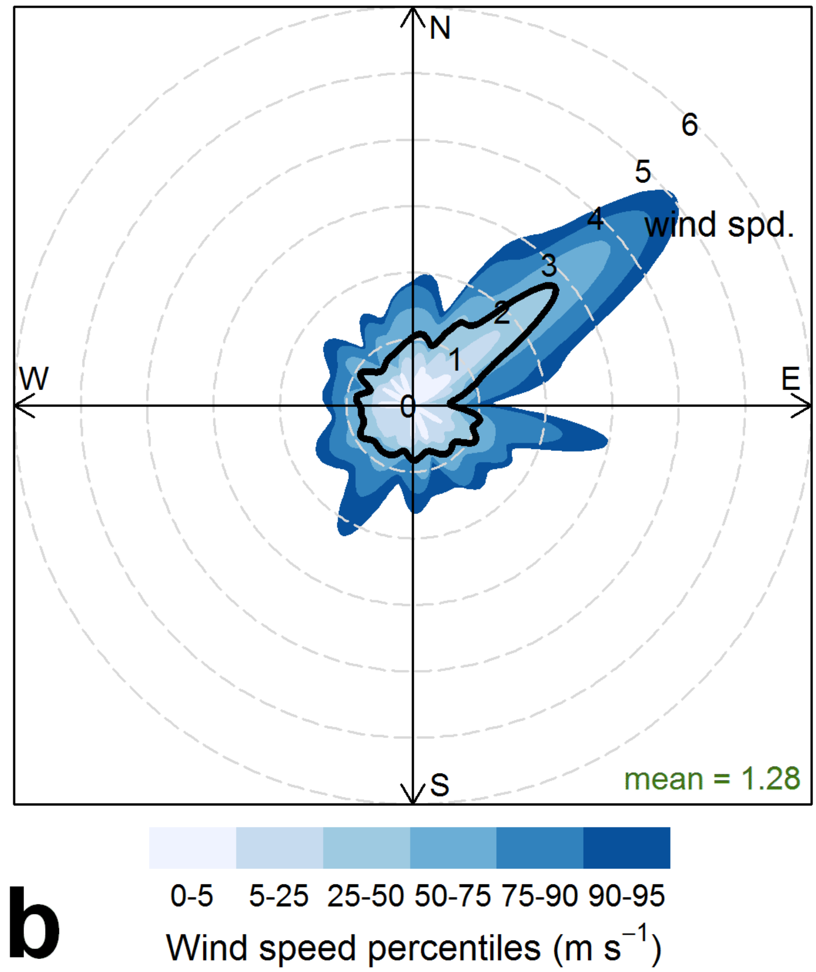

Figure A5. Wind regime observed at the Prato Università SIR meteorological station (ID 23, 01/12/2022-28/02/2023): (a) wind rose; (b) wind speed percentile rose. The bold black line in (b) denotes the average wind speed by direction. The occurrence of wind calm (wind speed below 0.5 m/s) and overall wind speed mean value are also reported.

Appendix B

Table B1. Performance parameters of the K-Nearest Neighbor Estimation imputation gap-filling method employed for estimating missing air temperature data at each station.

AirQino station		Lat	Lon	RMSE	R2
Name	**ID**	**(°N)**	**(°E)**	**(°C)**	**(·)**
Baciacavallo	1	43.8527	11.0775	0.65	0.99
Campaccio	2	43.8911	11.0777	0.93	0.99
Cava	3	43.8703	11.0538	0.84	0.99
Da Vinci	4	43.8608	11.1072	0.68	0.99
ESTRA	5	43.8692	11.0883	0.57	1
GIDA	6	43.8463	11.0809	0.78	0.99
Giordano	7	43.8841	11.0832	0.97	0.99
Bessi	8	43.8612	11.0451	0.7	0.99
Mannocci	9	43.8846	11.0545	0.74	0.99
Marradi	10	43.9012	11.1109	1.14	0.98
Narnali	11	43.8981	11.056	0.66	0.99
Nenni (giardini)	12	43.8736	11.0842	0.57	1
Nenni (parcheggio)	13	43.8738	11.0827	0.54	1
Santo Stefano (1)	14	43.8897	11.0635	0.72	0.99
Ragnaia	15	43.8621	11.1418	1.1	0.98
Reggiana	16	43.8773	11.0639	0.53	1
San Giorgio	17	43.8361	11.1071	0.63	0.99
Braga	18	43.845	11.0493	0.59	1
Turchia	19	43.8717	11.0631	0.47	1
San Marco	20	43.8776	11.1024	1.03	0.98
Ferrucci - ARPAT	21	43.8738	11.1044	NaN	NaN
Roma - ARPAT	22	43.8734	11.0923	NaN	NaN
*Università – SIR	23	43.8856	11.0992	NaN	NaN
Calice	24	43.8896	11.021	1.02	0.99
Campolmi	25	43.8763	11.0982	1.32	0.95
Cantagallo	26	43.9057	11.0961	1.03	0.98
Capponi	27	43.886	11.1046	0.62	0.99
Cascine Tavola	28	43.8416	11.0621	0.59	0.96
Castelnuovo	29	43.8274	11.0679	0.97	0.98
Ciari	30	43.8842	11.0369	0.6	1
Ferrucci	31	43.8614	11.1184	0.56	1
Lodz	32	43.8524	11.1076	0.36	1
Macrolotto1	33	43.8512	11.0621	0.58	1
Maliseti	34	43.8993	11.0682	0.7	0.99
Mercato	35	43.8841	11.0832	0.5	0.99
Miliotti	36	43.8611	11.0828	0.43	1
Paperino	37	43.8434	11.0922	0.53	0.99
Rimini	39	43.8779	11.0705	0.42	1
Santo Stefano (2)	40	43.8887	11.0605	0.45	1
Stazione	41	43.8778	11.108	0.81	0.99
Pavoniere	42	43.8394	11.0537	NaN	NaN

Table B2. Station average air temperature (AirT) estimated during different time intervals of the day on 16 July 2024.

AirQino station		Lat	Lon	00:00-06:00	07:00-11:00	12:00-16:00	17:00-23:00
Name	**ID**	**(°N)**	**(°E)**	**°C**	**°C**	**°C**	**°C**
Baciacavallo	01	43.8527	11.0775	22.04	29.32	34.47	28.69
Campaccio	02	43.8911	11.0777	21.84	28.91	34.86	27.99
Cava	03	43.8703	11.0538	22.5	28.89	35.57	28.94
Da Vinci	04	43.861	11.1069	21.78	28.95	34.41	28.1
ESTRA	05	43.8692	11.0883	22.54	30.17	35.81	28.28
GIDA	06	43.8463	11.0809	20.92	29.19	34.35	27.86
Giordano	07	43.8841	11.0832	21.77	28.93	34.41	28.06
Bessi	08	43.8612	11.0451	21.47	29.04	33.82	27.97
Mannocci	09	43.8846	11.0545	21.35	28.76	34.11	27.96
Marradi	10	43.9012	11.1109	21.34	28.05	33.87	27.39
Narnali	11	43.8981	11.056	22.39	29.68	34.94	28.52
Nenni (giardini)	12	43.8736	11.0842	22.03	29.2	33.66	27.82
Nenni (parcheggio)	13	43.8738	11.0827	21.92	29.09	34.27	28.06
Santo Stefano (1)	14	43.8897	11.0635	21.72	28.92	34.33	28.04
Ragnaia	15	43.8621	11.1418	19.6	28.89	34.92	27.08
Reggiana	16	43.8773	11.0639	21.77	28.93	34.41	28.11
San Giorgio	17	43.8361	11.1071	21.92	28.96	34.69	28.62
Braga	18	43.845	11.0493	21.85	29.58	35.04	28.56
Turchia	19	43.8717	11.0631	21.93	28.68	34.19	28
San Marco	20	43.8776	11.1024	22.61	27.9	33.19	28.63
Ferrucci - ARPAT	21	43.8738	11.1044	NaN	NaN	NaN	NaN
Roma - ARPAT	22	43.8734	11.0923	NaN	NaN	NaN	NaN
*Università – SIR	23	43.8856	11.0992	NaN	NaN	NaN	NaN
Calice	24	43.8896	11.021	20.57	28.12	32.97	27
Campolmi	25	43.8763	11.0982	22.96	30.36	35.93	28.87
Cantagallo	26	43.9057	11.0961	19.98	28.88	34.61	26.91
Capponi	27	43.886	11.1046	21.07	27.75	33.97	27.37
Cascine Tavola	28	43.8416	11.0621	21.64	29.02	34.48	28.2
Castelnuovo	29	43.8274	11.0679	20.07	29.17	35.26	27.71
Ciari	30	43.8842	11.0369	21.3	29.18	34.32	27.64
Ferrucci	31	43.8614	11.1184	21.84	28.29	34.04	28.47
Lodz	32	43.8524	11.1076	21.73	28.99	34.44	28.24
Macrolotto1	33	43.8512	11.0621	22.02	28.54	34.11	28.55
Maliseti	34	43.8993	11.0682	20.74	28.89	34.03	27.1
Mercato	35	43.8841	11.0832	21.75	28.91	34.41	28.05
Miliotti	36	43.8611	11.0828	22.28	28.81	34.31	28.67
Paperino	37	43.8434	11.0922	21.3	29.15	34.38	27.97
Rimini	39	43.8779	11.0705	21.78	28.95	34.41	28.1
Santo Stefano (2)	40	43.8887	11.0605	21.92	28.84	34.1	28.12
Stazione	41	43.8778	11.108	21.88	27.71	33.57	27.64
Pavoniere	42	43.8394	11.0537	NaN	NaN	NaN	NaN

Table B3. Multiple linear regression parameters performance and coefficients estimated during different time intervals of the day on 16 July 2024. Asterisks indicate significance levels (*** p<0.001, ** p<0.01, *p<0.05).

	Model performance parameters			Multiple linear regression coefficients		
Time interval	**R2**	**RMSE (°C)**	**RMSE-CV (°C)**	**LST**	**SVF**	**VFC**
00-06	0.38	0.58	0.66	0.20**	-1.25	0.31
07-11	0.11	0.49	0.58	0.03	-0.74	-0.61
12-16	0.30	0.51	0.56	0.06	-1.69**	-0.68
17-23	0.36	0.43	0.48	0.14**	-0.34	-0.41

Table B4. Coefficient of determination (R2), root mean square error (RMSE), and leave-one-out cross-validated RMSE (LOOCV) for four machine learning models. The Decision Tree regressor was implemented with a maximum tree depth of 3. The Random Forest regressor consisted of 15 trees with a maximum depth of 3 and a minimum of 5 samples per leaf. The Gradient Boosting regressor employed 15 estimators, a learning rate of 0.05, a maximum tree depth of 3, and a subsampling ratio of 0.8.

Model	**R2**	**RMSE**	**RMSE-CV**
Linear	0.30	0.50	0.58
Decision Tree	0.65	0.35	0.70
Random Forest	0.40	0.46	0.57
Gradient Boosting	0.57	0.39	0.59

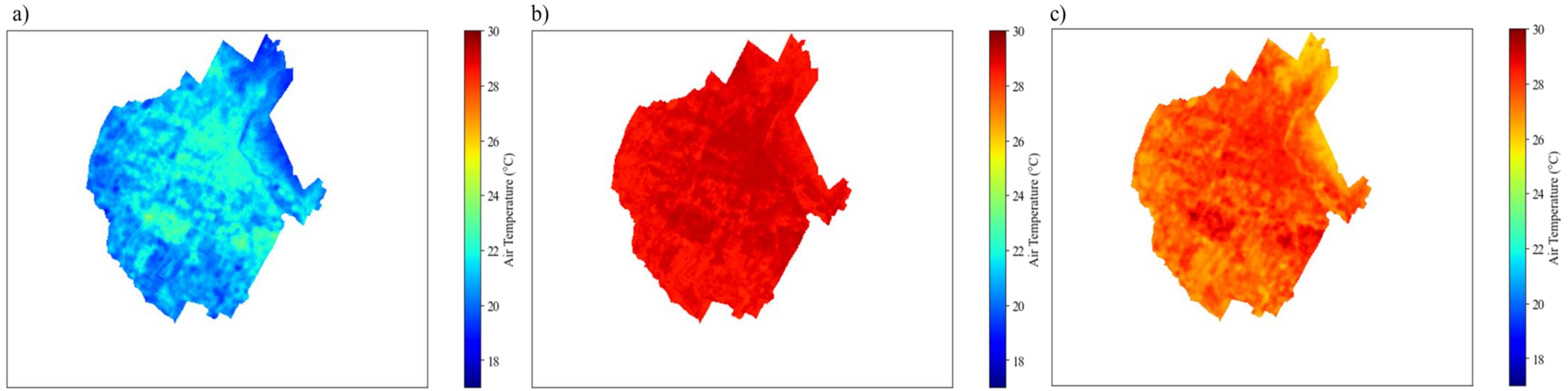

Figure B1. Modelled air temperature for the night (00:00–06:00, a), morning (07:00–11:00, b), and evening (17:00–23:00, c) time intervals. Average temperatures were 21.05 ± 0.80 °C, 28.81 ± 0.27 °C, and 27.57 ± 0.63 °C for the night, morning, and evening periods, respectively.

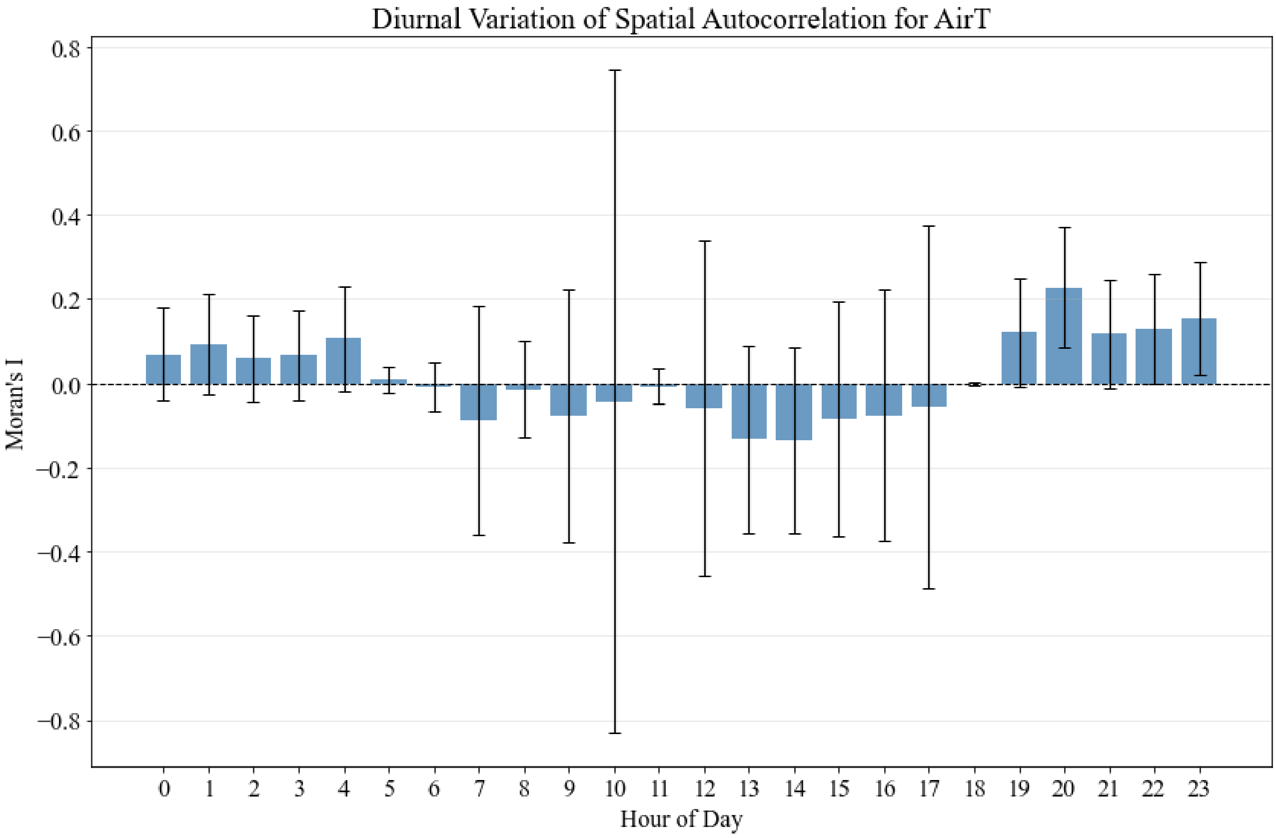

Figure B2. Diurnal variation of Spatial Autocorrelation of air temperature (AirT) assessed using Global Moran's I with a k-nearest-neighbors spatial weights matrix (k = 6), where each observation is connected to its six closest spatial neighbors based on Euclidean distance.

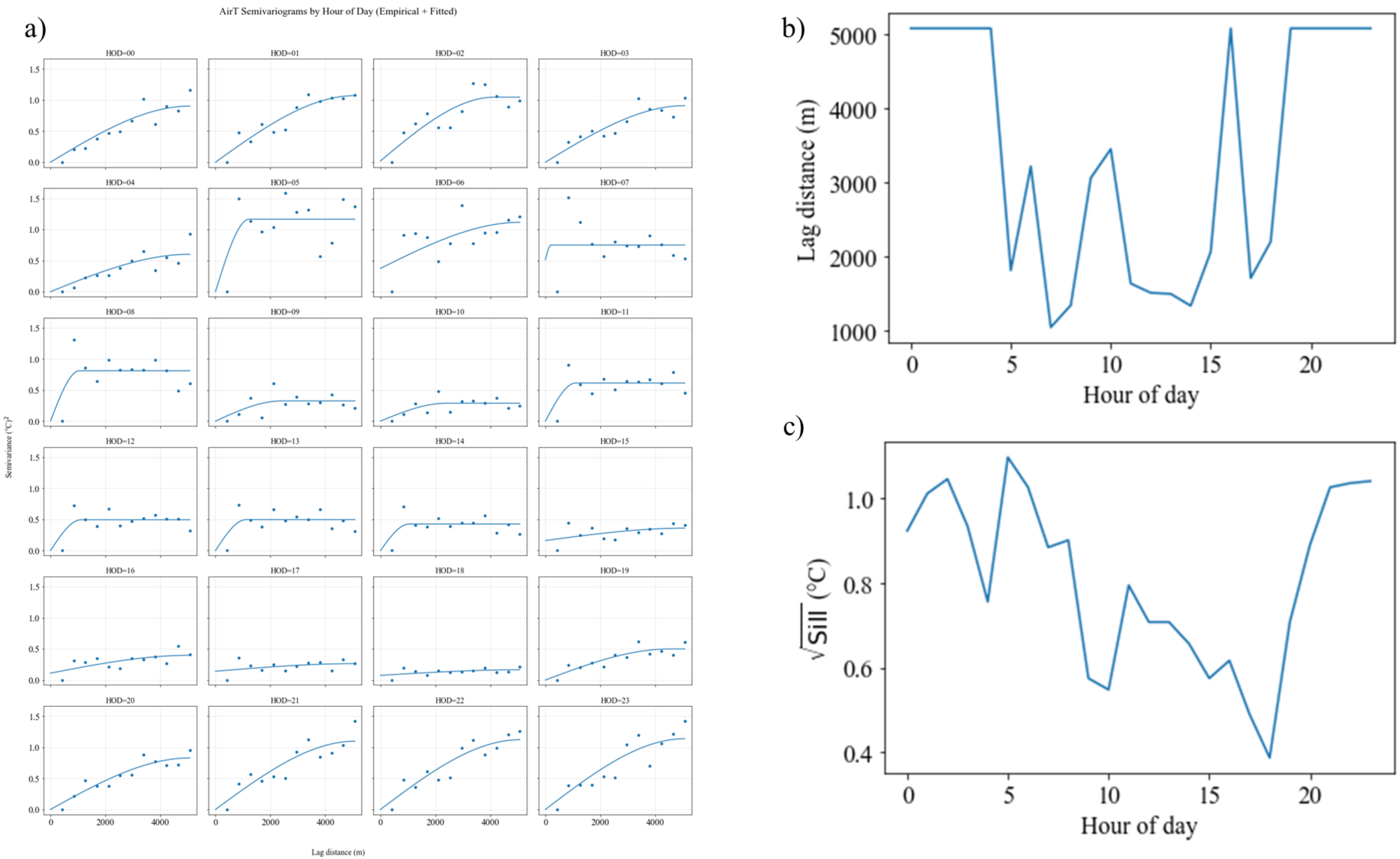

Figure X. Variogram-based assessments (a), Lag-distance (b) and Sill (C) of air temperature to evaluate spatial autocorrelation for each hour of the day (exponential model fitted using 12 lag classes up to a maximum separation distance of 5000 m).

Appendix C

Table C1. Observed soil water content (SWC, $m^3\ m^{-3}$) measured during the field campaign conducted on 15 July 2025 at both irrigated and rainfed validation sites. Values represent averages of 10 Time Domain Reflectometry (TDR) measurements collected at 3.5 cm soil depth for each time window (7:00, 9:00, 12:00, 15:00, 17:00, and 19:00).

Daytime	**Measurements x site**	**Site A (Irrigated)**	**Site B (Rainfed)**
- --	N°	SWC ($m^3\ m^{-3}$)	
7:00	10	0.27 ± 0.01	0.14 ± 0.02
9:00	10	0.26 ± 0.01	0.12 ± 0.03
12:00	10	0.27 ± 0.02	0.13 ± 0.02
15:00	10	0.26 ± 0.02	0.14 ± 0.02
17:00	10	0.24 ± 0.01	0.13 ± 0.03
19:00	10	0.22 ± 0.02	0.13 ± 0.03
7:00-19:00	120	Avg 0.25 ± 0.02	Avg. 0.131 ± 0.03

Table C2. Inventory of the 53 urban parks within the Municipality of Prato, including geographic coordinates, number of trees, park area, tree-density (trees m^{-2}), normalized tree-density (%), and classification into four tree-density classes (Class 1–4) based on quartile distribution.

ID	**Urban park**	**lon**	**lat**	**Trees**	**Area**	**Tree-density**	**Tree-density normalized**	**Class**
	Name	(°)	(°)	N°	m^2	(N° m^{-2})	%	
01	La Querce	11.14	43.86	7	4046.66	0.0017	0.00	1
02	Pieta	11.10	43.89	27	13479.57	0.0020	0.02	1
03	De Gasperi	11.12	43.87	16	7060.36	0.0023	0.04	1
04	Grignano	11.08	43.86	27	8817.38	0.0031	0.11	1
05	Como	11.09	43.84	31	9034.65	0.0034	0.14	1
06	Le Betullaie	11.09	43.89	49	13963.88	0.0035	0.15	1
07	Casale	11.04	43.87	25	6857.19	0.0036	0.16	1
08	Mediterraneo	11.05	43.89	89	23891.55	0.0037	0.16	1
09	Ferraris	11.10	43.86	86	22250.95	0.0039	0.18	1
10	Maliseti	11.07	43.90	196	48163.33	0.0041	0.19	1
11	San Giorgio	11.11	43.84	44	9892.55	0.0044	0.22	1
12	Vivaldi	11.08	43.89	39	8066.96	0.0048	0.26	2
13	Turchia	11.06	43.87	163	31731.63	0.0051	0.28	2
14	Vergaio	11.06	43.88	46	8567.17	0.0054	0.30	2
15	Bellandi	11.05	43.85	22	4043.12	0.0054	0.31	2
16	Campaccio	11.08	43.89	82	14656.71	0.0056	0.32	2
17	Montegrappa	11.12	43.86	135	24070.08	0.0056	0.32	2
18	Corte delle Girandole	11.09	43.88	6	1041.95	0.0058	0.33	2
19	Garibaldi	11.05	43.90	12	2014.83	0.0060	0.35	2
20	Roma	11.08	43.85	106	17211.22	0.0062	0.37	2
21	Liberazione e Pace	11.08	43.87	706	112559.21	0.0063	0.38	2
22	Badie	11.09	43.86	80	12477.57	0.0064	0.39	2
23	Pratocchio	11.06	43.88	81	12397.68	0.0065	0.40	2
24	Iolo	11.04	43.87	24	3475.11	0.0069	0.43	2
25	Rondine	11.12	43.88	96	13307.48	0.0072	0.45	2
26	Tobbiana	11.05	43.87	94	13002.13	0.0072	0.45	2
27	Galciana	11.05	43.89	44	6058.19	0.0073	0.46	2
28	Giocagi	11.11	43.90	132	17444.20	0.0076	0.48	2
29	Picasso	11.11	43.86	45	5794.27	0.0078	0.50	3
30	Valori	11.06	43.89	26	3280.98	0.0079	0.51	3
31	Colombo	11.09	43.88	111	13945.14	0.0080	0.51	3
32	Ex-Magnolfi	11.11	43.88	47	5820.61	0.0081	0.52	3
33	Tirso	11.09	43.90	52	6181.08	0.0084	0.55	3
34	Fanfani	11.05	43.88	9	1069.35	0.0084	0.55	3
35	Beethoven	11.09	43.86	33	3906.42	0.0084	0.55	3
36	Sacra Famiglia	11.12	43.88	263	30142.52	0.0087	0.58	3

37	Centro Ventrone	11.07	43.87	17	1905.28	0.0089	0.59	3
38	Tobbiana	11.06	43.87	52	5731.96	0.0091	0.61	3
39	Nenni	11.08	43.87	90	9847.65	0.0091	0.61	3
40	F.lli Ventura	11.07	43.91	60	6463.88	0.0093	0.62	3
41	Teatro	11.08	43.88	57	6087.87	0.0094	0.63	3
42	Viaccia	11.06	43.90	36	3747.35	0.0096	0.65	3
43	Marx	11.09	43.87	98	9934.08	0.0099	0.67	3
44	Borgonuovo	11.07	43.89	36	3563.55	0.0101	0.69	3
45	Menabuoni	11.11	43.87	67	6375.86	0.0105	0.72	3
46	Puccini	11.10	43.90	104	9625.03	0.0108	0.75	4
47	Gianni	11.08	43.85	13	1175.93	0.0111	0.77	4
48	Passerella	11.10	43.88	44	3961.46	0.0111	0.77	4
49	Marchini	11.10	43.87	40	3307.15	0.0121	0.86	4
50	Stazione	11.11	43.88	195	16052.96	0.0121	0.86	4
51	Ciparrisso	11.15	43.87	184	15077.72	0.0122	0.86	4
52	Macine	11.13	43.87	14	1026.24	0.0136	0.98	4
53	San Paolo	11.07	43.89	47	3396.03	0.0138	1.00	4

Table C3. Initializing hourly values of AirT and RH for both irrigated and rainfed sites

Hour of day	Irrigated		Rainfed	
	AirT	RH	AirT	RH
00:00	21.3	93.72	21.21	94.5
01:00	20.75	94.12	20.29	94.57
02:00	20.1	91.97	19.92	93.54
03:00	19.73	92.48	19.94	94.84
04:00	19.32	92.11	19.34	94.07
05:00	19.74	91.51	19.44	90.05
06:00	21.94	82.3	22.55	79.14
07:00	23.89	75.79	23.82	74.03
08:00	25.7	69.96	26.1	68.4
09:00	27.46	64.4	28.08	63.51
10:00	29.29	56.56	29.79	56.39
11:00	31.34	48.88	32.04	51.27
12:00	33	43.24	33.58	47.07
13:00	34.38	40.12	34.96	45.35
14:00	35.04	42.1	34.91	45.51
15:00	35.19	41.71	35.14	46.13
16:00	34.53	47.2	34.36	48.43
17:00	32.88	50.66	33.49	52.01
18:00	31.4	56.23	32	57.35
19:00	29.48	67.32	29.8	70.53
20:00	27.08	80.41	26.75	83.05
21:00	25.58	85.71	25.45	87.19
22:00	24.99	89.88	25.09	90.39
23:00	24.15	90.93	24.2	90.56

Table C4. Soil hydraulic parameters adjusted during ENVI-met model validation, including water content at saturation, field capacity, wilting point, matric potential, hydraulic conductivity, volumetric heat capacity, and the Clapp & Hornberger constant for both rainfed and irrigated sites.

Section	Parameters	Soil properties		
		Default	Irrigated Tuned	Rainfed Tuned
Hydraulic parameters	Water content at saturation (m^3_{water}/m^3_{soil})	0.42	0.477	0.477
	Field Capacity (FC, m^3_{water}/m^3_{soil})	0.255	0.322	0.322
	Wilting Point (WP, m^3_{water}/m^3_{soil})	0.175	0.218	0.218
	Matrix Potential (m)	-0.299	-0.356	-0.356
	Hydraulic Conductivity ((m/s) 10^{-6})	6.3	1.7	1.7
	Volumetric Heat Capacity ((j/m^3k) 10^{-6})	1.175	1.317	1.317
	Clapp & Hornberger Constant (none)	7.12	7.75	7.75
Simple forcing wind conditions	Wind speed (m s^{-1})	- - -	1.5	1.5
	Wind direction (°)	- - -	270	270
Initial soil water content (0-20cm)	SWC_{IN} (m^3 m^{-3})	0.227	0.270	0.139

Table C5. Irrigation scenarios (BS and AS1–AS4), applied water volumes, and related costs for urban parks grouped by microclimatic classes (IC, Inner City; NR, Near River) and tree-density class (1–4). Reported variables include irrigation rate, total applied water, and total irrigation cost (€), disaggregated into acquisition (A), storage (S), and water treatment (WT). Aggregated values at microclimate classes level (IC-All and NR-All) are also provided.

Class	Tree cover class	Park surface	Irr. Scenarios	Irrigation x day	Irrigation x day	Cost x day A	Cost x day S	Cost x day WT	TOTAL x day
- - -	- - -	(m^2)	- - -	(m^3m^{-2})	(m^3)	(€)	(€)	(€)	(€)
IC	1	8817.38	BS	0	0	0	0	0	0
			AS1	0.018	158.7	312.7	141.3	115.9	569.8
			AS2	0.024	211.6	416.9	188.3	154.5	759.7
			AS3	0.03	264.5	521.1	235.4	193.1	949.6
			AS4	0.036	317.4	625.3	282.5	231.7	1139.6
	2	11868.42	BS	0	0	0	0	0	0
			AS1	0.018	213.6	420.9	190.1	156.0	766.9
			AS2	0.024	284.8	561.1	253.5	207.9	1022.6
			AS3	0.03	356.1	701.4	316.9	259.9	1278.2
			AS4	0.036	427.3	841.7	380.3	311.9	1533.9
	3	10500.02	BS	0	0	0	0	0	0
			AS1	0.018	189.0	372.3	168.2	138.0	678.5
			AS2	0.024	252.0	496.4	224.3	184.0	904.7
			AS3	0.03	315.0	620.6	280.4	230.0	1130.9
			AS4	0.036	378.0	744.7	336.4	275.9	1357.0
	4	9610.03	BS	0	0	0	0	0	0
			AS1	0.018	173.0	340.8	154.0	126.3	621.0
			AS2	0.024	230.6	454.4	205.3	168.4	828.0
			AS3	0.03	288.3	568.0	256.6	210.5	1035.0
			AS4	0.036	346.0	681.5	307.9	252.6	1242.0
NR	1	13479.57	BS	0	0	0	0	0	0
			AS1	0.018	242.6	478.0	215.9	177.1	871.0
			AS2	0.024	323.5	637.3	287.9	236.2	1161.4
			AS3	0.03	404.4	796.6	359.9	295.2	1451.7
			AS4	0.036	485.3	956.0	431.9	354.2	1742.1
	2	6561.26	BS	0	0	0	0	0	0
			AS1	0.018	118.1	232.7	105.1	86.2	424.0
			AS2	0.024	157.5	310.2	140.1	115.0	565.3
			AS3	0.03	196.8	387.8	175.2	143.7	706.6
			AS4	0.036	236.2	465.3	210.2	172.4	848.0
	3	15485.33	BS	0	0	0	0	0	0
			AS1	0.018	278.7	549.1	248.1	203.5	1000.7
			AS2	0.024	371.6	732.1	330.8	271.3	1334.2
			AS3	0.03	464.6	915.2	413.5	339.1	1667.8
			AS4	0.036	557.5	1098.2	496.1	407.0	2001.3

	4	16053	BS	0	0	0	0	0	0
			AS1	0.018	289.0	569.2	257.2	210.9	1037.3
			AS2	0.024	385.3	759.0	342.9	281.2	1383.1
			AS3	0.03	481.6	948.7	428.6	351.6	1728.9
			AS4	0.036	577.9	1138.5	514.3	421.9	2074.7
IC	All	40795.85	BS	0	0	0	0	0	0
			AS1	0.07	734	1447	654	536	2636.2
			AS2	0.10	979	1929	871	715	3515.0
			AS3	0.12	1224	2411	1089	893	4393.7
			AS4	0.14	1469	2893	1307	1072	5272.5
NR	All	51579.16	BS	0	0	0	0	0	0
			AS1	0.07	928	1829	826	678	3333.0
			AS2	0.10	1238	2439	1102	904	4444.1
			AS3	0.12	1547	3048	1377	1130	5555.1
			AS4	0.14	1857	3658	1653	1356	6666.1

Figures

Figure C1. AirQino low-cost air quality monitoring station: (a) design and internals; (b) examples of installation sites across Prato

Figure C2. Diurnal cycles of AirT and RH for the near-river (NR, blue) and inner-city (IC, red) microclimate classes. Panel (a) shows mean hourly patterns averaged over the summer period (1 June–31 August 2024), while panel (b) reports hourly averages for the representative day used for model initialization (15 July 2025), derived from 6 (NR) and 17 (IC) AirQino stations. Error bars indicate inter-station variability.

Figure C3. Localization of the 53 urban parks located within the Municipality of Prato as reported by the official database.

Figure C4. Statistics of ENVI-model calibration for both irrigated and rainfed sites.

Figure C5. ENVI-met maps of ΔAirT provided by the urban parks located in the near-river (NR) class under the four irrigation scenarios across the tree-density classes during the 12:00-16:00 time-window.

Figure C6. ENVI-met maps of ΔAirT provided by the urban parks located in the inner-city (IC) class under the four irrigation scenarios across the tree-density classes during the 12:00-16:00 time-window.

Figure C7. Average diurnal differences in latent heat (a) and sensible heat (b) between the baseline and the four irrigation scenarios (AS1–AS4), simulated across four tree-density classes (CL1–CL4) for the urban park domains located in the inner-city (IC) and near-river (NR) microclimate classes. Shaded areas indicate confidence intervals arising from the spatial aggregation of the simulated domain and reflect sub-grid spatial variability

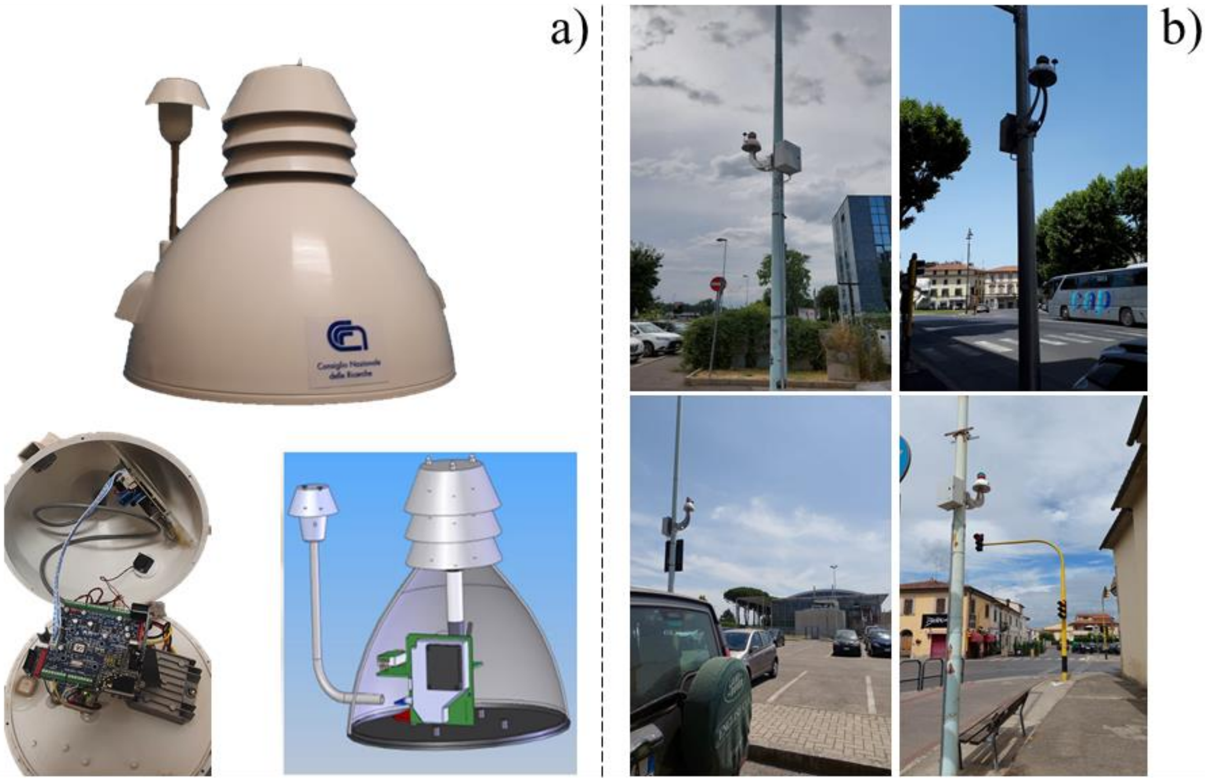

Figure C1

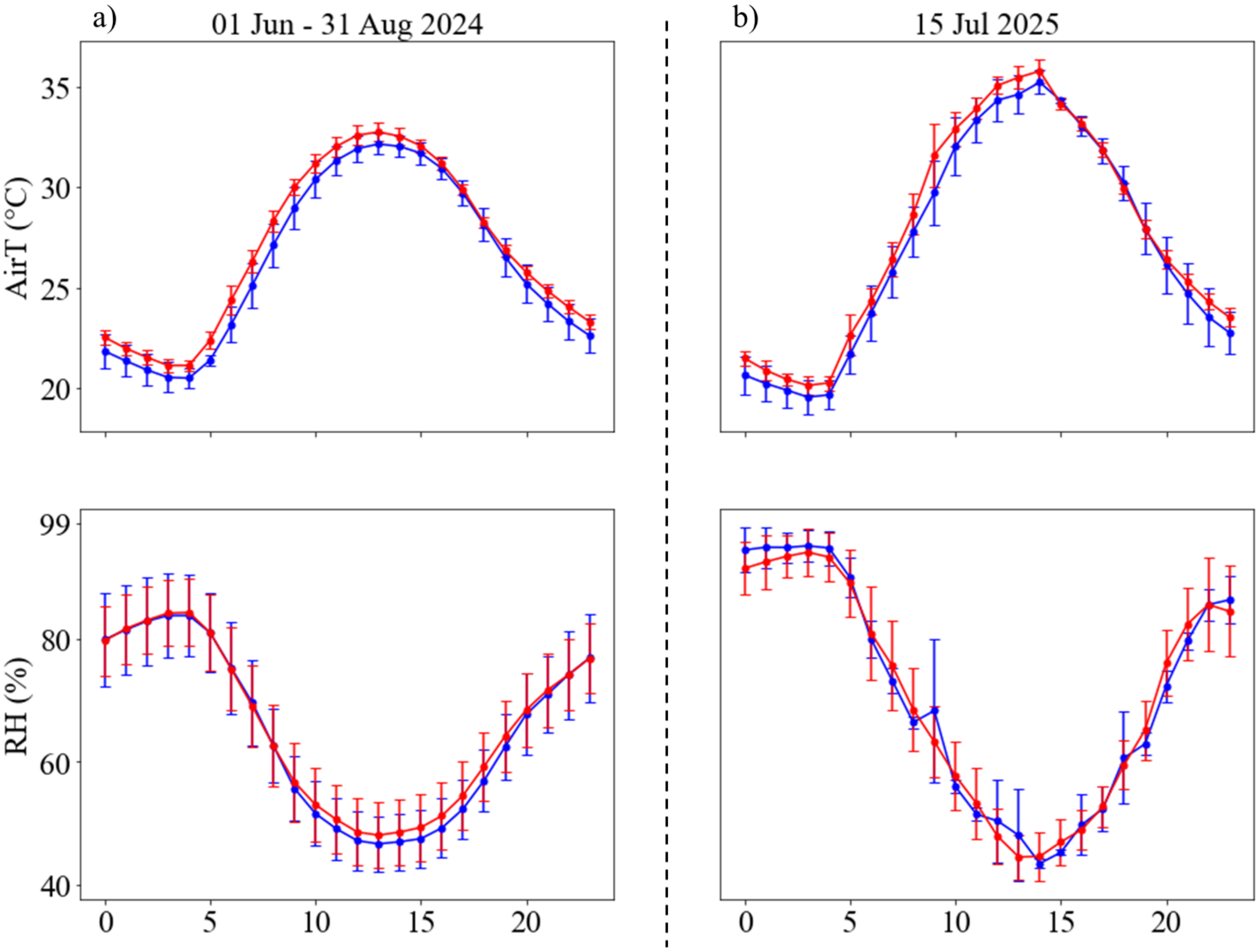

a)
01 Jun - 31 Aug 2024
b)
15 Jul 2025
AirT (°C)
RH (%)
35
30
25
20
99
80
60
40
0
5
10
15
20

Figure C2

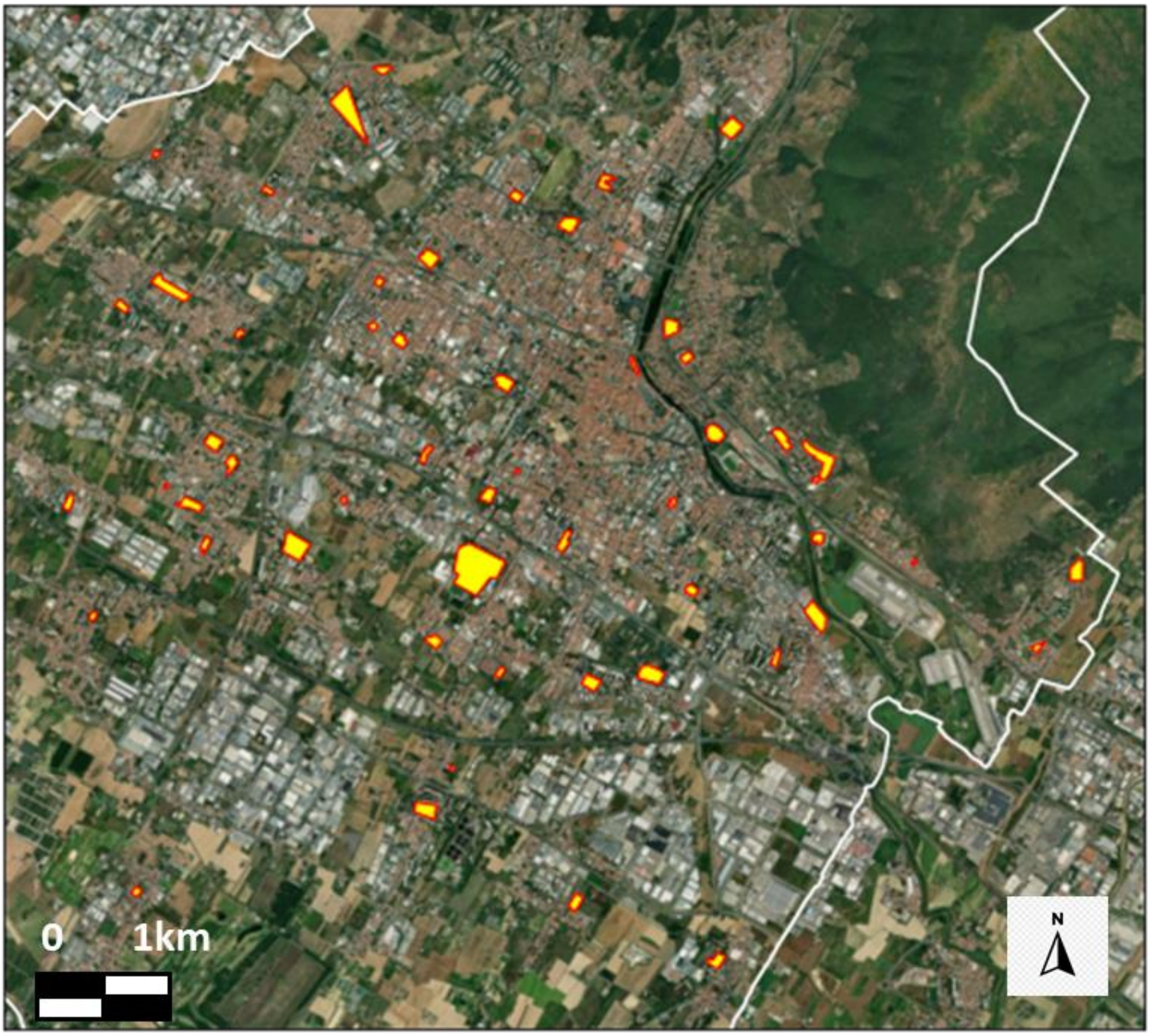

Figure C3

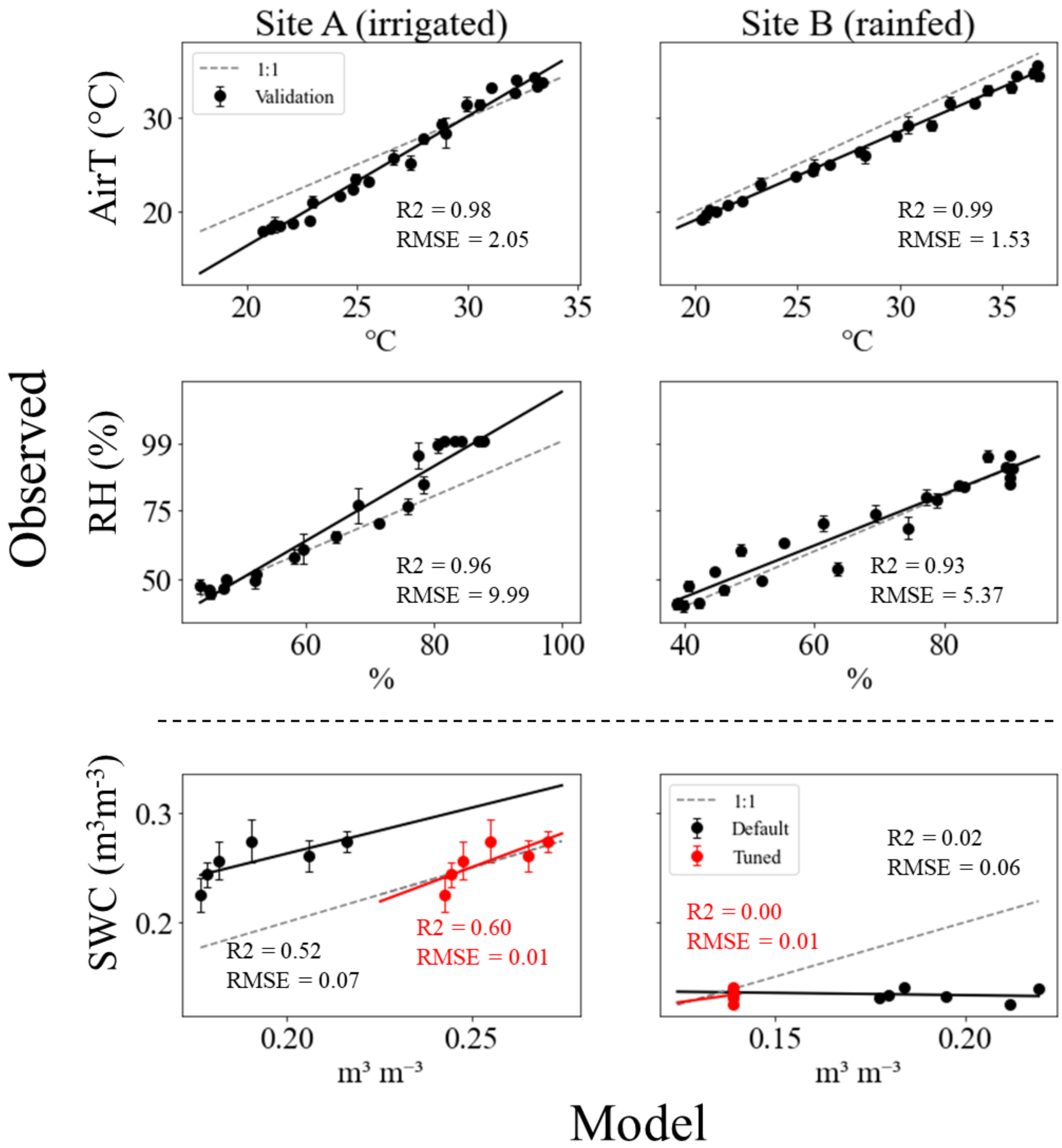
Site A (irrigated)
Site B (rainfed)
Observed
AirT (°C)
1:1
Validation
R2 = 0.98
RMSE = 2.05
R2 = 0.99
RMSE = 1.53
°C
RH (%)
R2 = 0.96
RMSE = 9.99
R2 = 0.93
RMSE = 5.37
%
SWC (m3m-3)
R2 = 0.52
RMSE = 0.07
R2 = 0.60
RMSE = 0.01
Default
Tuned
R2 = 0.02
RMSE = 0.06
R2 = 0.00
RMSE = 0.01
m3 m-3
Model

Figure C4

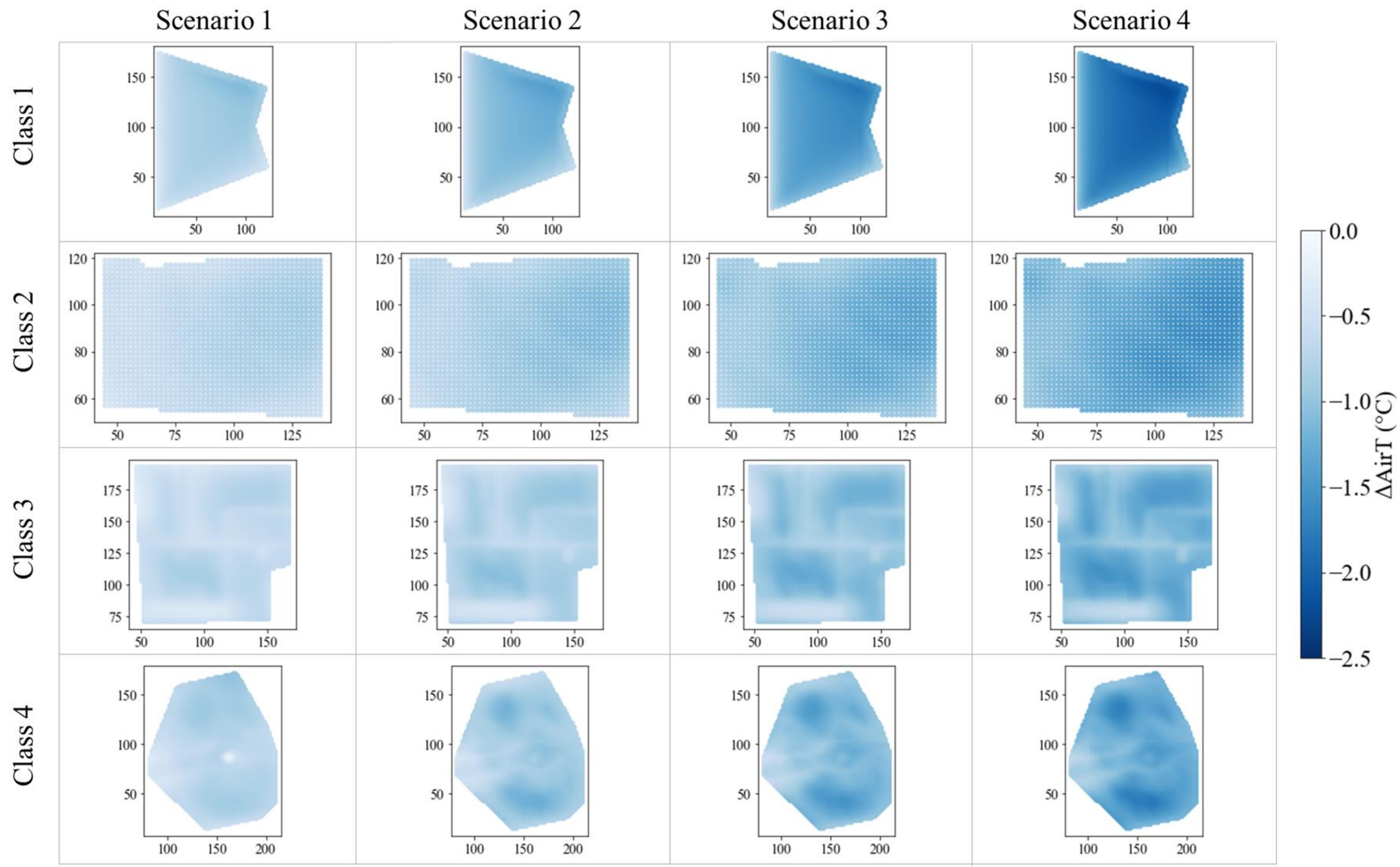

Scenario 1
Scenario 2
Scenario 3
Scenario 4
Class 1
Class 2
Class 3
Class 4
ΔAirT (°C)
0.0
−0.5
−1.0
−1.5
−2.0
−2.5

Figure C5

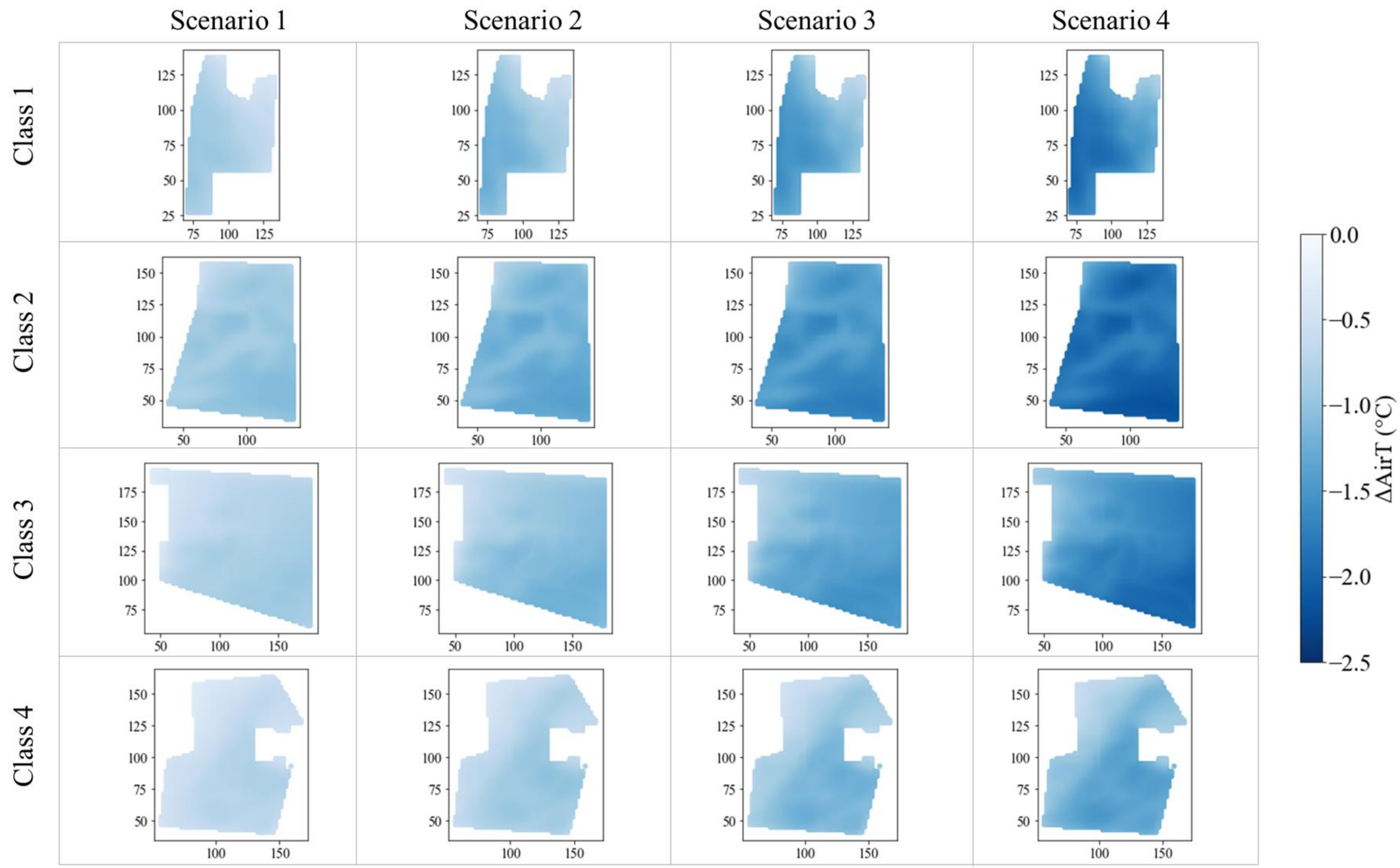

Scenario 1
Scenario 2
Scenario 3
Scenario 4
Class 1
Class 2
Class 3
Class 4
ΔAirT (°C)
0.0
−0.5
−1.0
−1.5
−2.0
−2.5

Figure C6

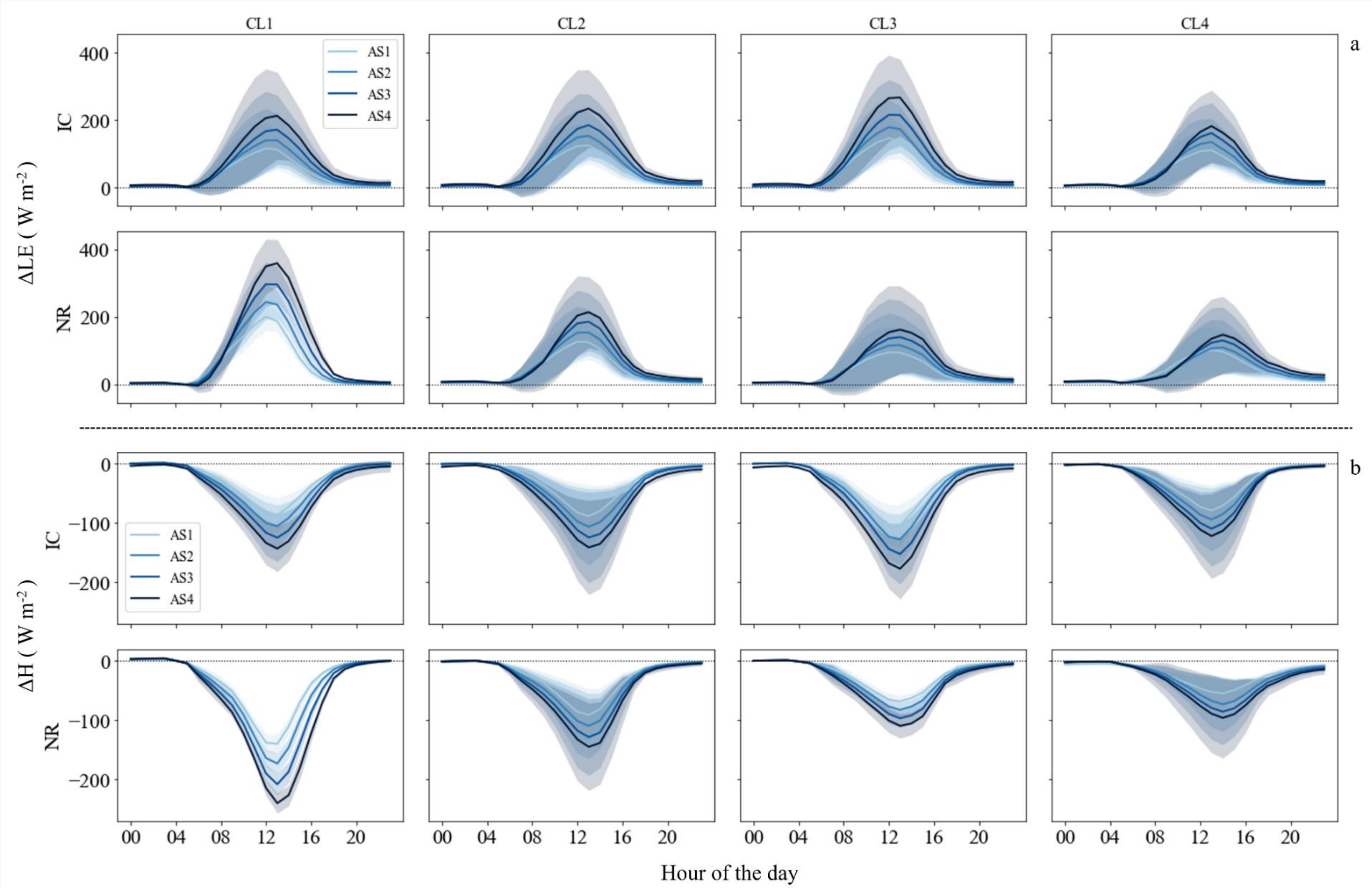
CL1
CL2
CL3
CL4
a
b
AS1
AS2
AS3
AS4
ΔLE (W m^{-2})
ΔH (W m^{-2})
IC
NR
400
200
0
−100
−200
00
04
08
12
16
20
Hour of the day

Figure C7